Experimental Demonstration of Advanced Palladium Membrane Separators for Central High Purity Hydrogen Production

Final Report

Project Period:	15 June 2007 to 30 June 2010
Date of Report:	30 September 2010
Award Number:	DE–FC26–07NT43055
Authors:	Sean C. Emerson, Neal Magdefrau, Susanne Opalka, Ying She, Catherine Thibaud-Erkey, Thomas H. Vanderspurt, & Rhonda Willigan
Submitting Organization:	United Technologies Research Center 411 Silver Lane East Hartford, CT 06108
Working Partners:	Power & Energy, Inc. Metal Hydride Technologies Incorporated Pall Corporation

Contents

List of Figures

List of Tables

Abstract

The overall objectives for this project were to: (1) confirm the high stability and resistance of a PdCu trimetallic alloy to carbon and carbide formation and, in addition, resistance to sulfur, halides, and ammonia; (2) develop a sulfur, halide, and ammonia resistant alloy membrane with a projected hydrogen permeance of 25 $m^3m^{-2}atm^{-0.5}h^{-1}$ at 400 °C and capable of operating at pressures of 12.1 MPa (≈120 atm, 1750 psia); and (3) construct and experimentally validate the performance of 0.1 kg/day H_2 PdCu trimetallic alloy membrane separators at feed pressures of 2 MPa (290 psia) in the presence of H_2S, NH_3, and HCl. This project successfully increased the technology readiness level of palladium-based metallic membranes for hydrogen separation from coal-biomass gasifier exhaust or similar hydrogen-containing gas streams. The reversible tolerance of palladium-copper (PdCu) alloys was demonstrated for H_2S concentrations varying from 20 ppmv up to 487 ppmv and NH_3 concentrations up to 9 ppmv. In addition, atomistic modeling validated the resistance of PdCu alloys to carbon formation, irreversible sulfur corrosion, and chlorine attack.

The experimental program highlighted two key issues which must be addressed as part of future experimental programs: (1) tube defects and (2) non-membrane materials of construction. Four out of five FCC PdCu separators developed leaks during the course of the experimental program because≈10% of the alloy tubes contained a single defect that resulted in a thin, weak point in the tube walls. These defects limited operation of the existing tubes to less than 220 psig. For commercial applications of a PdCu alloy hydrogen separator under high sulfur concentrations, it was determined that stainless steel 316 is not suitable for housing or supporting the device. Testing with sulfur concentrations of 487±4 ppmv resulted in severe corrosion of the stainless steel components of the separators.

The project identified an experimental methodology for quantifying the impact of gas contaminants on PdCu alloy membrane performance as well as an atomistic modeling approach to screen metal alloys for their resistance to irreversible sulfur corrosion. Initial mathematical descriptions of the effect of species such as CO and H_2S were developed, but require further experimental work to refine. At the end of the project, an improvement to the experimental approach for acquiring the necessary data for the permeability model was demonstrated in preliminary tests on an enhanced PdCu separator.

All of the key DOE 2010 technical targets were met or exceeded except for the hydrogen flux. The highest flux observed for the project, 125 $ft^3ft^{-2}h^{-1}$, was obtained on a single tube separator with the aforementioned enhanced PdCu separator with a hydrogen feed pressure of 185 psig at 500 °C.

1 Executive Summary

The overall objectives for this project were to: (1) confirm the high stability and resistance of a PdCu trimetallic alloy to carbon and carbide formation and, in addition, resistance to sulfur, halides, and ammonia; (2) develop a sulfur, halide, and ammonia resistant alloy membrane with a projected hydrogen permeance of 25 $m^3m^{-2}atm^{-0.5}h^{-1}$ at 400 °C and capable of operating at pressures of 12.1 MPa (≈120 atm, 1750 psia); and (3) construct and experimentally validate the performance of 0.1 kg/day H_2 PdCu trimetallic alloy membrane separators at feed pressures of 2 MPa (290 psia) in the presence of H_2S, NH_3, and HCl. In addition, the performance of the best separator candidate was to be tested for long-term operation. The project was also to provide a techno-economic evaluation of the use of PdCu alloy hydrogen separators for central hydrogen production from coal gasifier fuel gas, including an analysis of the best system configurations to use with the separators.

This project was focused on increasing the technology readiness level of palladium-based metallic membranes for hydrogen separation from coal-biomass gasifier exhaust or similar hydrogen-containing gas streams. Quantum mechanical atomistic modeling was performed in a previous contract (DE-FC26-05NT42453) to virtually develop a ternary PdCu alloy for a water gas shift membrane reactor (WGSMR) in a coal gasifier system. The alloy was based on the concept of making the BCC phase of a PdCu binary alloy stable at WGSMR temperatures in the presence of high concentrations of poisons such as sulfur. As the BCC phase of PdCu has a much higher hydrogen permeability than the FCC materials, and the FCC materials have been shown to have good sulfur resistance, a stabilized BCC alloy should be able to obtain the high permeability of alloys like PdAg with the sulfur tolerance of FCC PdCu. Thus one of the additional objectives of this work was to experimentally validate the UTRC PdCu ternary alloy performance. In addition, the best commercially available FCC PdCu alloy from UTRC's subcontractor, Power+Energy, was also to be experimentally validated for meeting the DOE technical targets.

In addition to the Pd-based, dense metallic membranes, the project was also focused on developing an advanced membrane concept which was a hybrid of ceramic and dense metallic membrane technology. The advanced concept involved using <100 nm colloidal Pd particles to plug the pores of a nanoporous oxide supported on a porous stainless steel tube. The Pd-alloy/nanoporous oxide concept should theoretically result in much higher fluxes, lower costs, and higher operating pressures than what is currently achievable by dense metallic membranes alone. The Pd-alloy/nanoporous oxide approach was added to the project statement of work in April 2009.

The project demonstrated the reversible sulfur tolerance of PdCu alloy separators. After the project began, the DOE developed a testing protocol for evaluating membrane performance (Driscoll, 2008). An FCC PdCu membrane produced for this project was tested for 527 hours under the DOE test protocol conditions. The testing was performed under pure H_2 as well as test conditions 1, 2a, and 2b. Under the specific test conditions, the pure H_2 flux of this separator was 45±2 $ft^3ft^{-2}h^{-1}$ with a H_2 recovery of >80% at 450 °C and 200 psia. Upon exposure to the DOE test 1 conditions, this flux decreased to 14±2 $ft^3ft^{-2}h^{-1}$ with a similar recovery. When 20 ppmv H_2S was introduced during test 2a conditions, the flux was further reduced to 11±1 $ft^3ft^{-2}h^{-1}$ with a corresponding decrease in recovery to (61±7)%, however, membrane performance remained stable during the 100+ hours at each condition. Finally, when the H_2 concentration was decreased and the sulfur level increased to 40 ppmv, the flux was reduced to 6±1 $ft^3ft^{-2}h^{-1}$ with a H_2 recovery of (50±6)%. The

decrease in H_2 flux due to composition effects was completely reversible based on measurements taken with pure H_2 between each of the gas compositions and also the fact that the membrane did not leak. This further supports the conclusion that FCC PdCu is sulfur resistant and not susceptible to sulfur corrosion.

Development of the UTRC ternary PdCuTM alloy resulted in a permeability performance in 2009 that was similar to that of the FCC PdCu alloy. Further characterization was performed to determine the root cause of the lower than expected performance. An unwanted TM-oxide surface scale formed during manufacturing of the separator tubes and required removal. The separator performance in 2009 was measured after chemical etching which resulted in selective dissolution of the Cu, leaving the surface Pd-rich. It is known from the literature (McKinley, 1967 & 1969) that a PdCu alloy with greater than ≈50at% Pd has a rather poor permeability compared to pure Pd. As a result, a mechanical polishing technique was developed to remove the surface oxide scale without affecting the surface PdCu composition. The data for the polished separator tubes, showed that the performance was improved by a factor of two.

A technical and economic modeling analysis was performed for the FCC PdCu dense metallic membranes. Similar assumptions to those used in the DOE test protocol (Driscoll, 2008) were used in the calculations. A mean flow rate of 6.425×10^5 $kg.h^{-1}$ was used for membrane sizing calculations based on different gasifier systems operating in the range of 520 MW to 640 MW (Klara, 2007). For the purposes of the analysis, the gas was assumed to be at the DOE protocol test 1 composition (50% H_2, 1% CO, 30.0% CO_2, & 19.0% H_2O). H_2 recovery curves as a function of membrane surface area and membrane feed pressure at 450 °C were developed. Higher feed pressures resulted in higher fluxes and thus a reduced area for the same H_2 recovery.

For a high H_2 recovery, a dense metallic PdCu membrane for this size system would require an area approaching 60,000 m^2 and the metal would cost on the order of $200,000,000. However, one advantage of the dense metallic membranes is that the raw materials can be recycled and the Pd cost can be significantly reduced by a lease and recycling strategy. In addition, the very high H_2 purity achievable by dense metallic membranes, along with their higher technology readiness level, makes the dense metallic approach a viable path forward for H_2 separation while other, longer-term, low-cost technology paths are further developed.

At the end of the project, a new type of separator, based on the FCC PdCu and "enhanced" through a proprietary P+E process was evaluated and appeared to have the same permeability as the BCC PdCu. However, the membrane did not go through a phase transformation at temperatures above 450 °C and appeared to retain the sulfur resistance of the FCC PdCu while achieving a higher hydrogen permeability. The highest flux observed for the project, 125 $ft^3ft^{-2}h^{-1}$, was obtained on a single tube enhanced PdCu separator with a hydrogen feed pressure of 185 psig at 500 °C.

Three separate methods were investigated for the Pd-alloy/nanoporous oxide membrane part of the project. A single membrane tube was prepared using a two-step infiltration approach to introduce the colloidal particles. Although the nitrogen permeance of the membrane was reduced to 12% of the baseline oxide coated support tube, the tube failed during a hydrogen reduction step, leading to micron-sized defects which prevented the membrane from undergoing a hydrogen permeance test. The most promising results were obtained using a proprietary approach to depositing Pd within the oxide coated tubes. Nitrogen permeance reductions of 96% were obtained relative to the baseline oxide coated

support tubes with that technique. However, time constraints prevented additional membrane processing for a hydrogen permeability measurement to be performed.

The final progress toward the DOE's technical targets for hydrogen separation is given in Table 1. The 2010 target for hydrogen flux was not attained, but all of the other metrics were met or exceeded.

Table 1: Technical progress for the project as measured against the DOE's technical targets for hydrogen separation.

Metric	2010 DOE Target	Current Project Status	Notes
Hydrogen Flux	200 $ft^3ft^{-2}h^{-1}$	**125 $ft^3ft^{-2}h^{-1}$ (P+E alloy)**	• Enhanced P+E alloy at 500 °C; 185 psig H_2
Temperature	300–600 °C	**350–600 °C**	• UTRC ternary alloy limited to 450 °C
Sulfur tolerance	20 ppmv	**78 ppmv H_2S (P+E alloy)** 9 ppmv NH_3 (P+E alloy)	• Demonstrated with P+E alloy at 450 °C • Demonstrated 487±4 ppmv for 4 hours • Demonstrated 9 ppmv NH_3 for 175 hours
ΔP operating capability	Up to 400 psi ΔP	**200 psig**	• Current tube thicknesses limited to ≈200 psia
CO tolerance	Yes	**Yes**	• Demonstrated up to 13.3% CO at 90 psia total pressure; >9% CO at 304.7 psia
Hydrogen purity	99.5%	**99.9999%**	• P+E manufacturing design and manufacturing ensures no leaks • CO < 1 ppm, S < 15 ppbv desired for fuel cell applications

2 Results

2.1 Dense Metallic Membrane Development

2.1.1 Technical and Economic Modeling

2.1.1.1 System Trade Studies for WGS and Pd Membrane Configurations

System trade studies were performed to examine the impact on efficiency of feed pressure, steam to carbon ratio, and the order in which the H_2 separation with palladium membranes and the water gas shift (WGS) reaction using the HYSYS process simulation software package. UTRC has a proprietary model for calculating the performance of WGS membrane reactors to account for different mass transfer mechanisms through Pd membranes. A modification of HYSYS's membrane extension unit operation module was made to incorporate UTRC's membrane reactor model into HYSYS system level calculations. Once the UTRC module was integrated with HYSYS, high fidelity system trade studies on the above variables as well as Pd membrane size and cost were performed. As the project progressed, the modeling work was shifted away from system level trade studies toward experimental data analysis and economic modeling of just the membrane separators.

The HYSYS membrane extension unit operation module was critical for trade studies because it significantly impacts the system efficiency and membrane cost calculations. The

HYSYS extension unit operation module was implemented to provide the specific membrane permeability and calculate the performance of a membrane with its temperature and pressure dependency. The modified module was integrated into two fuel processing systems with two configurations to produce hydrogen with a feed of "dry coal gas".

The two system HYSYS diagrams are shown in Figure 1 and Figure 2, respectively. The two systems are almost identical except for the fact that the system 2 configuration does not have a membrane unit in front of the high temperature water gas shift (HTWGS) reactor. The conditions of the "dry coal gas" labeled in the system diagrams as "cleaned gas" are listed in Table 2. System efficiency was improved by adding a burner in each system, where the combustible gases in the retentate were sent to and burned to recover the thermal energy. In a real plant, this step could be replaced by a gas turbine to generate power. The exhaust stream from the burner in each system was used to generate steam for the water gas shift (WGS) reactions. For the initial economic study, membrane cost was evaluated based on the material cost of the membrane alloy used. Membrane permeabilities were obtained through previous UTRC experimental data and used for the preliminary cost calculations. Table 3 lists the assumed material costs for the membranes as well as the hydrogen permeability coefficient and activation energy used in the simulations.

The major results of the two initial baseline systems are summarized in Table 4. The system efficiency and H_2 recovery listed in the table are defined by the following equations.

$$\text{System efficiency } \eta = \frac{\text{LHV of pure } H_2 \text{ produced}}{\text{LHV of cleaned gas} + \text{energy consumed}}$$

$$H_2 \text{ recovery } (\%) = \frac{\text{Pure } H_2 \text{ produced through membranes}}{H_2 \text{ in feed to membranes}}$$

The use of an additional membrane separator in the front of the HTWGS in system 1 can produce somewhat more hydrogen than system 2 by removing much of it from the initial gas stream. As a result, the system efficiency of the system 1 was about 80.7% while system 2 had an efficiency of 77%. However, the membrane cost for the system 1 was approximately \$5.5/SCFH H_2 versus an estimated \$4.96/SCFH H_2 in system 2.

Table 2: Conditions for the "dry coal gas" feed to the fuel processing system.

Feed, kg/h	Temperature, °C	Pressure, atm	Compositions, %			
			CO	CO_2	H_2	N_2
3.516×10^4	400	120	61.1	2.1	33.9	2.9

Table 3: Material costs and permeation properties of the membrane used in the initial trade studies.

Material cost, \$/g			Membrane permeation properties	
Pd	Ag	Cu	Permeability coefficient, mol/(m h $Pa^{0.5}$)	Activation energy, kJ/mole
8.0	0.225	3.97×10^{-3}	1.59×10^{-3}	20.5

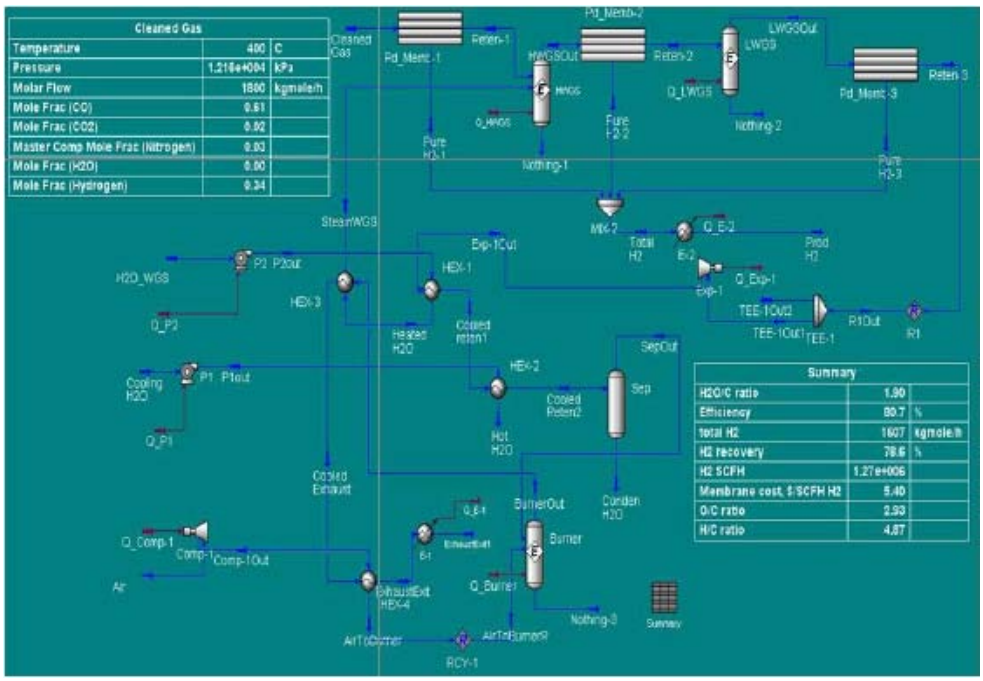

Figure 1: Fuel processing system 1 configuration HYSYS baseline process diagram.

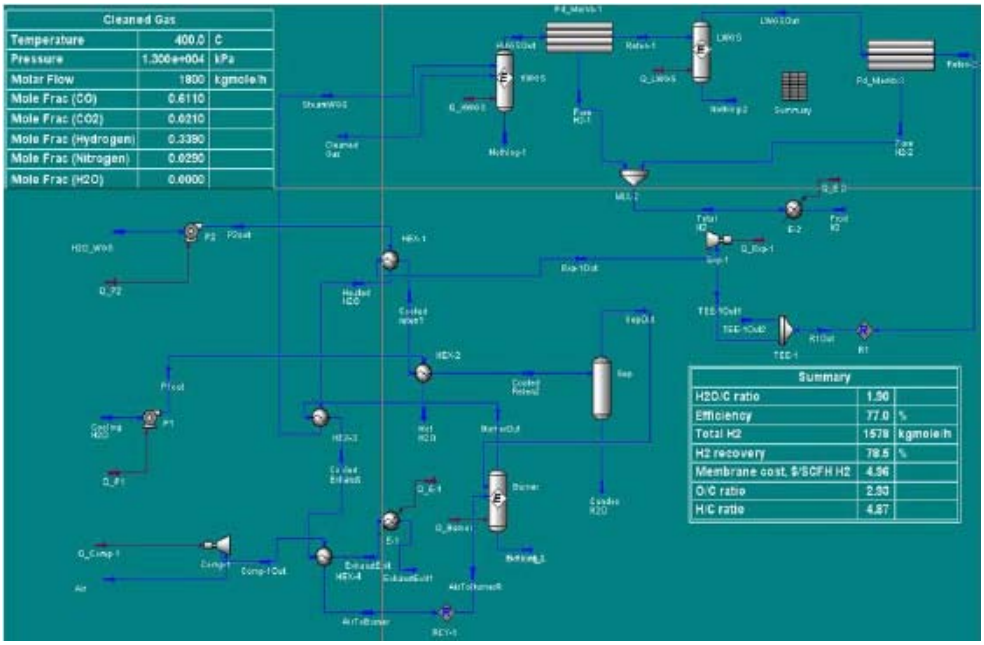

Figure 2: Fuel processing system 2 configuration HYSYS baseline process diagram.

Table 4: Summary of both initial system performances at baseline conditions.

	Efficiency %	H_2 recovery %	H_2 produced kg/h	H_2O/C -	O/C -	Cost $/SCFH H_2
System I	80.7	78.6	3214	1.9	2.93	5.4
System II	77	78.5	3156	1.9	2.93	4.96

2.1.1.2 External Collaboration on Technical and Economic Modeling

A collaboration was developed with Professor Robert Braun at the Colorado School of Mines (CSM). CSM had a DOE project (contract award DE-NT0005202) titled: *Coal/Biomass Gasification at the Colorado School of Mines*. Professor Braun's effort was Task I-C: Systems Modeling and Optimization. The following is a description of the task.

> The objectives of Task I-C are several fold: (1) Generate modeling tools to perform system analysis of integrated gasification fuel cell power plants (IGFC) that employ advanced technologies, such as high temperature ceramic heat exchangers and catalytic membrane reactors; (2) Perform a quantitative assessment of the potential system benefits and performance issues when such hardware is integrated within gasification plants where the analysis is inclusive of carbon capture concepts; and (3) Evaluate the importance of system operating parameters (such as degree of co-mingled biomass/coal feedstocks, and gasifier and SOFC-GT operating conditions) and quantify the sensitivity of system performance to a variation in these parameters.
>
> The approach employed involves the evaluation (and selection) of different software platforms. The modeling effort shall leverage existing models and where necessary, extend or develop new component models (e.g., SOFC, membrane reactors, etc.) that enable system performance prediction, analysis, and optimization of IGFC plants. Commercial or "near"-commercial hardware performance characteristics, such as GE H-class and/or Pratt & Whitney FT8 gas turbine product lines, shall be implemented. Additionally, a preliminary evaluation of gasification technology options that are most compatible with IGFC plant concepts shall be performed prior to the execution of extensive system architecture and parameter optimization studies. System models shall be built to study performance sensitivities due to variations in system configurations and operating parameters. Emphasis will be placed on tying system studies to other task efforts in this project and evaluation of carbon capture strategies in the SOFC periphery. Plant size and SOFC stack performance will be consistent with DOE SECA program goals (>100 MW and > 0.5 W/cm$_2$ power density).

As part of the collaboration, UTRC transferred the mathematical equations described in Section 2.1.4.2 to CSM, as well as the permeability data publicly presented at the DOE Peer

Reviews. The objective of this effort was to explore different ways to integrate Pd membranes and WGSMRs into integrated gasification fuel cell power plants.

2.1.1.3 Thermodynamic Modeling

Two important parameters in assessing the economics of coal-to-hydrogen plants are the gasification pressure and the steam to carbon ratio. Recent publications have considered pressures of 70 atm to 120 atm and steam to carbon ratios of 2.4 to 1.5 (Chiesa et al., 2005a & 2005b) and have concluded that using current available technologies (in particular pressure swing adsorption for separation), there might be an economical benefit to operating at higher pressures and lower steam to carbon ratios. Such modifications need to be evaluated as well with respect to the operation of a H_2 membrane.

Increasing the operating pressure and decreasing the steam to carbon ratio may have some important repercussions on the reactivity of the gas mixture and in particular, special attention should be directed to the possibility of carbide and coke formation. Carbide formation within the Pd alloy of a H_2 separator was addressed through atomic modeling, described below. To better understand the limitations of steam to carbon ratio reduction, it was necessary to calculate operating conditions where there is a thermodynamic driving force for carbon formation.

The HSC thermodynamic software package was used to study the coking issue thermodynamically with different oxygen to carbon (O/C) and hydrogen to carbon (H/C) ratios to map out coking regions. O/C and H/C ratios were varied by fixing the initial amount of carbon in a system but varying O_2 and H_2 amounts. The components that were allowed to be present during the equilibrium calculations were: C, CO, CO_2, H_2, O_2, H_2O, CH_4, C_2H_2, C_2H_4, and C_2H_6. The equilibrium calculations were conducted at 1 atm pressure and temperatures between 25 °C and 1000 °C. Calculation results about coking temperature regions with different O/C and H/C ratios are listed in Table 5. The coking temperature resolution in Table 5 is ±5 °C due to the temperature increments used for the calculations.

Table 5 indicates that with high O/C ratios above 2.5 and low H/C ratios below 1 there is no coke formation within the entire temperature range calculated (25–1000 °C). On the other hand, with O/C ratios below 0.75 and H/C ratios below 1 coking can occur within the entire temperature range. However, coking may not be an issue at these low temperatures due to slow carbon formation kinetics.

Pressure has a significant impact on coke formation. Table 6 gives the coking map under 20 atm pressure for temperatures between 25 °C and 1000 °C. Compared to Table 5, there are more “no coking” temperature regions at high H/C ratios above 10 and high O/C ratios larger than 1.25 because methanation is favored at elevated pressures. Calculated thermodynamic tables such as Table 6 were used to guide the membrane separator modeling and experimental studies to avoid carbon formation under “dry” oxygen coal gasifier syngas conditions.

Table 5: Coking temperature map based on thermodynamic calculations at 1 atm and 25 °C to 1000 °C with a ±5 °C temperature resolution. Temperature ranges in the table indicate the temperature region in which coke formation is possible.

		H/C 0.5	H/C 1	H/C 2	H/C 5	H/C 10	H/C 15	H/C 20
O/C	0.5	coking	coking	coking	160–840	230-785	255–741	265–735
O/C	0.75	coking	coking	25–885	25–60 & 110–800	225–750	250-720	265–700
O/C	1	25–865	25–830	25–785	25–735	220–690	250–665	265–650
O/C	1.25	25–725	25–715	25–695	25–665	215–635	245–615	260–600
O/C	1.5	25–655	25–650	25–635	25–610	205–585	240–570	260–555
O/C	1.75	25–585	25–580	25–570	25–550	200–525	235–510	260–500
O/C	2	25–405	25–415	25–425	25–425	190–420	235–410	255–405
O/C	2.25	No coking	25–275	20–305	25–330	175–345	230–345	255–345
O/C	2.5	No coking	No coking	20–270	25–305	165–315	225–320	250–320
O/C	2.75	No coking	No coking	20–240	25–285	145–300	220–305	250–305
O/C	3	No coking	No coking	No coking	25–270	125–290	215–290	245–290

Table 6: Coking temperature map based on thermodynamic calculations at 20 atm and 25 °C to 1000 °C with a ±5 °C temperature resolution. Temperature ranges in the table indicate the temperature region in which coke formation is possible.

		H/C 0.5	H/C 1	H/C 2	H/C 5	H/C 10	H/C 15	H/C 20
O/C	0.5	coking	coking	coking	345–725	440–625	515–545	No coking
O/C	0.75	coking	coking	25–855	355–695	460–600	No coking	No coking
O/C	1	25–970	25–885	25–785	25–270 & 375–665	485–560	No coking	No coking
O/C	1.25	25–885	25–805	25–735	25–280 & 400–630	No coking	No coking	No coking
O/C	1.5	25–780	25–740	25–685	25–280 & 435–580	No coking	No coking	No coking
O/C	1.75	25–695	25–665	25–610	25–275	No coking	No coking	No coking
O/C	2	25–465	25–440	25–350	25–275	No coking	No coking	No coking
O/C	2.25	No coking	25–305	25–310	25–270	No coking	No coking	No coking
O/C	2.5	No coking	No coking	25–285	25–270	No coking	No coking	No coking
O/C	2.75	No coking	No coking	25–260	25–265	No coking	No coking	No coking
O/C	3	No coking	No coking	No coking	25–260	No coking	No coking	No coking

2.1.1.4 Techno-economic Analysis of Membrane Cost

A technical and economic modeling analysis was performed for PdCu dense metallic membranes. Similar assumptions to those used in the DOE test protocol (Driscoll, 2008) were used in the calculations. A mean flow rate of 6.425×10^5 kg.h^{-1} was used for membrane sizing calculations based on different gasifier systems operating in the range of 520 MW to 640 MW (Klara, 2007). For the purposes of the analysis, the gas was assumed to be at the DOE protocol test 1 composition (50% H_2, 1% CO, 30.0% CO_2, & 19.0% H_2O). Figure 3 shows the H_2 recovery as a function of membrane surface area at 450 °C. The recovery curves are presented as a function of the membrane feed pressure. Higher feed pressures result in higher fluxes and thus a reduced area for the same H_2 recovery.

For the economic analysis, a 7-year mean Pd price of $9.38/g was used. Figure 4 shows the cost of the PdCu metal as a function of tube thickness for the data shown in Figure 3. Also shown is the minimum tube thickness required for the operating feed pressure. As the

operating pressure goes up, the tube thickness will increase, resulting in more expensive tubes.

For a high H_2 recovery, a dense metallic PdCu membrane for a 520 MW to 640 MW system would require an area approaching 60,000 m^2 and the metal would cost on the order of $200,000,000 (approximately $(300–500)/ft^2$). However, one advantage of the dense metallic membranes is that the raw materials can be recycled and the Pd cost can be significantly reduced by a lease and recycling strategy. In addition, the very high H_2 purity achievable by dense metallic membranes, along with their higher technology readiness level, makes the dense metallic approach a viable path forward for H_2 separation while other, longer-term, lower-cost technology paths are further developed.

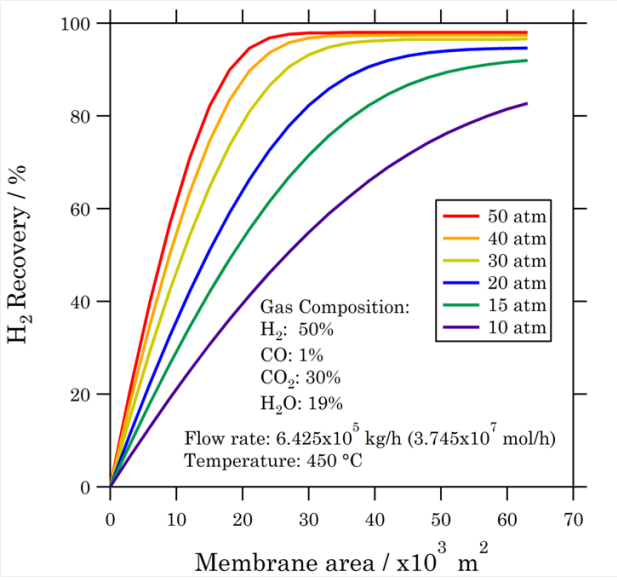

Figure 3: Impact of H_2 recovery on PdCu membrane surface area for a 520–640 MW gasifier system operated at 450 °C.

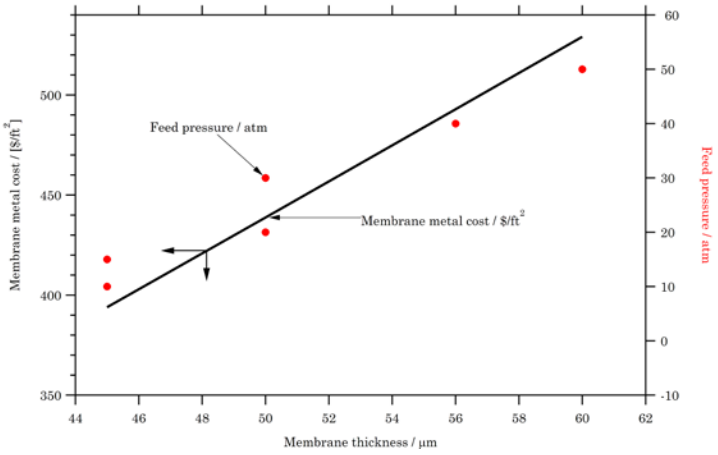

Figure 4: PdCu dense metallic membrane cost and operating feed pressure as a function of tube wall thickness.

2.1.2 Membrane Separator Development and Fabrication

2.1.2.1 Initial FCC PdCu and BCC Ternary Alloy Separators

An initial ten (10) separators were fabricated and delivered to UTRC for testing in late 2007. Five of the separators were constructed with an FCC PdCu alloy provided by Power+Energy. The remaining five separators were built using the UTRC PdCuTM alloy composition developed under a previous DOE contract. At the beginning of the project, a total of twelve separators were to be constructed, with the choice of alloy for the remaining two to be made based on testing results. It was expected that the final two separators would be used for endurance testing. However, by early 2008, it was apparent that the ternary alloy was not performing as expected.

Sample tubes of both the FCC PdCu and UTRC ternary alloys were provided by Power+Energy for characterization. Initially, X-ray diffraction patterns were taken of both tubes before testing was conducted on the first UTRC ternary alloy separator. The patterns, shown in Figure 5, show that the P+E alloy is in the FCC phase, while the UTRC alloy is primarily in the BCC phase with a trace amount of FCC. The lattice parameters for the UTRC ternary alloy diffraction pattern agreed to within 1.7% of the atomistic modeling predictions, giving preliminary evidence that the ternary alloy phase had been successfully created.

Further characterization of separator tubes indicated that the surface of the membrane alloy tubes for the UTRC ternary BCC PdCu composition consisted primarily of a binary alloy. The binary alloy between Pd and the ternary element TM existed in a layer approximately 600±100 Å deep and acted as a dissociation and diffusion barrier for hydrogen. Thermal treatments in the presence of hydrogen were unable to significantly improve the performance of the separator units with the UTRC composition (see Section 2.1.4.1).

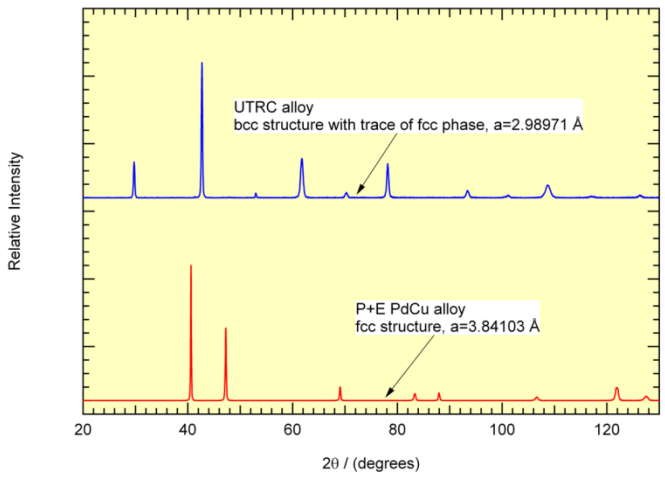

Figure 5: X-ray diffraction patterns on alloy tubes prepared in parallel with hydrogen separators. Bulk diffraction indicated the P+E PdCu alloy was FCC, as expected, and that the UTRC ternary alloy was BCC with a trace of FCC.

Further characterization was performed using electron backscatter diffraction (EBSD) in a scanning electron microscope (SEM). The sample tube section used previously for

surface characterization was cut open and polished to expose the tube cross-section. Figure 6 shows the EBSD phase map for the UTRC ternary alloy. All of the areas colored in green indicate the presence of the BCC PdCuTM phase. Areas that are dark could not be characterized by the technique. These dark areas corresponded primarily to the grain boundaries and may have been due to the positioning of the sample or the degree of polishing. The algorithm did not detect the PdTM binary or oxides of the TM element within the tube cross-section. Figure 7 shows the various elemental maps for the three elements showing that they were uniformly dispersed within the alloy tube sample.

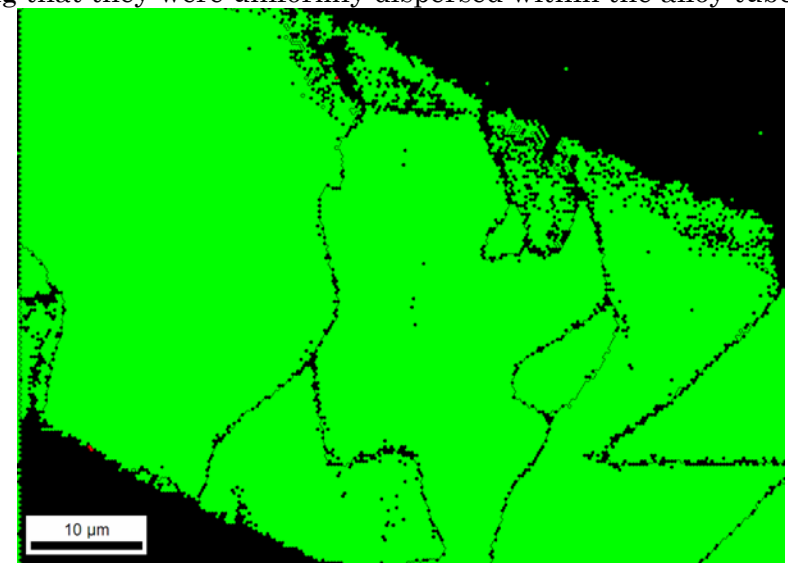

Figure 6: EBSD phase map of PdCuTM alloy tube cross-section. The green colored areas indicate the presence of the ternary alloy phase while the dark areas were not identified by the algorithm. The dark areas reside primarily at the grain boundaries. Neither an oxide of TM ternary element nor the PdTM binary compound was detected in the cross-section.

2.1.2.2 In situ Chemical Etching to Remove Surface Barrier on UTRC Ternary Alloy

Since thermal treatments were unable to remove the PdTM surface layer and the thickness of this layer was relatively thin, the effort moved to using chemical etching to improve separator performance. An etching system composed of hydrofluoric acid (HF), nitric acid (HNO_3), and phosphoric acid (H_3PO_4) was identified as appropriate for removing the TM element in particular. The nitric acid oxidizes the surface species which are subsequently removed with HF by converting the surface oxides into water soluble fluorides. The phosphoric acid serves as a buffering agent to moderate the etching rate.

Of particular concern was the co-etching of stainless steel 316 parts of the separator assemblies when the units were etched in situ. As a result, some initial tests were performed on 0.5-mm long membrane tube samples in the presence of stainless steel 316 tubing to evaluate the etching performance. The initial results, as measured by chemical analysis of the etching solutions after treatment, indicated that the solution could be used to remove the TM element from the surface layer. Experiments were performed with small alloy tube sections in environments where stainless steel was either present or absent. When the tube sections were etched in the presence of stainless steel, a new etching

procedure at elevated temperatures was required to etch both the stainless steel and the membrane tubes at comparable rates.

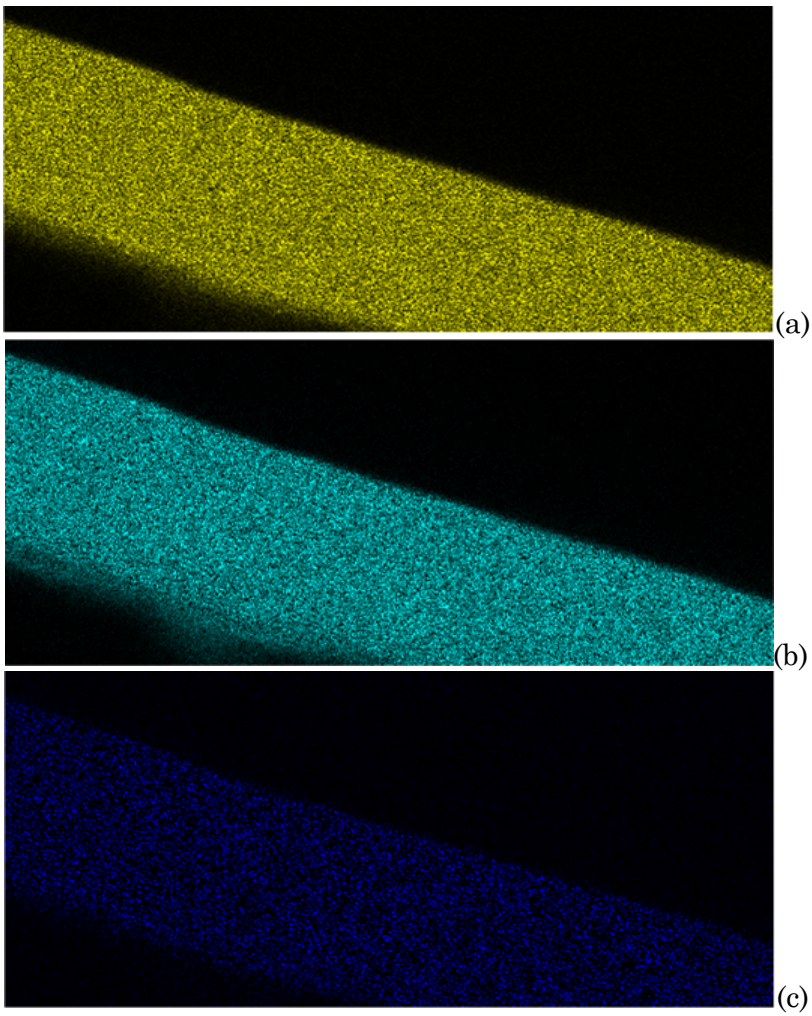

Figure 7: Elemental maps of the PdCuTM alloy tube cross-section for (a) Pd, (b) Cu, and (c) the ternary TM element. All three elements are uniformly distributed throughout the cross-section of the tube.

Figure 8 shows a scanning electron microscope (SEM) image of a ternary alloy tube after testing in hydrogen, but before etching had been performed. Note that there is a well defined grain boundary visible at a magnification of 500×. Figure 9 shows a ternary alloy tube after one hour of etching at elevated temperature. Although there appeared to be a minor change in the surface texture of the sample, there was no significant weight loss, indicating that this period of time was too short to have an effect on the surface layer.

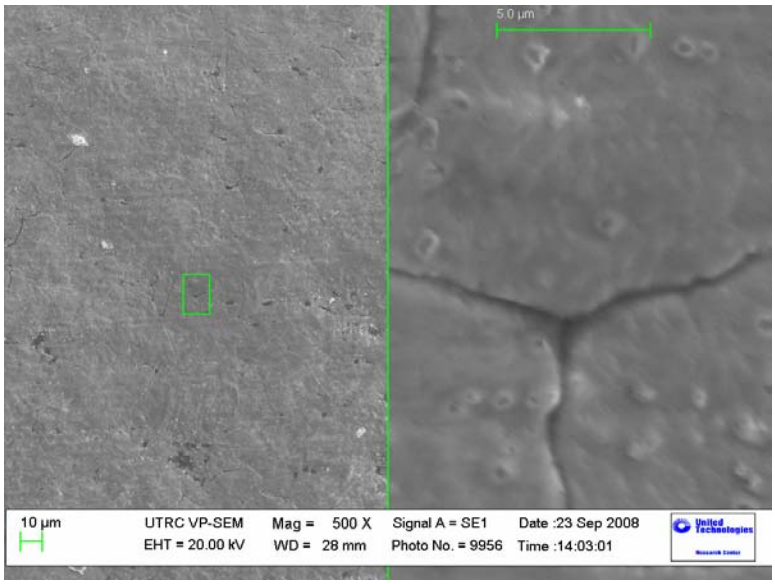

Figure 8: Tube from separator UTRC-5130 after thermal treatments and before etching.

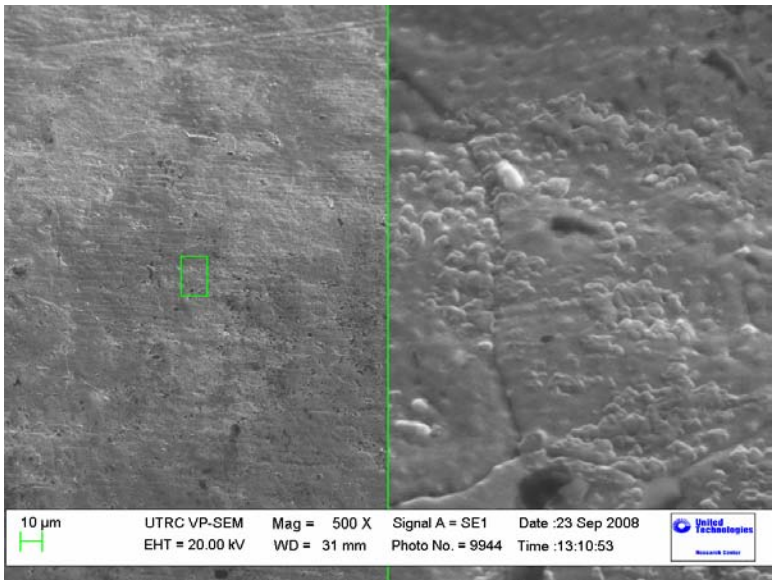

Figure 9: Tube from separator UTRC-5130 after one (1) hour with new etching procedure.

Figure 10 is an image of another tube sample that was etched for three hours with the new etching procedure in a stainless steel vessel. The SEM image at 500× shows a marked change in surface texture which corresponded to a weight loss of 5%. This weight loss was equivalent to removal of approximately 1 µm from both sides of the tube sample, which was more than enough to remove the surface binary layer. Additional evidence of the efficacy of the etching procedure is shown in Figure 11, where a tube sample was etched overnight for approximately 12 hours. This extended etching time resulted in what appeared to be a crystallographic preference in the surface texture, as well as a loss of 50% of the sample weight.

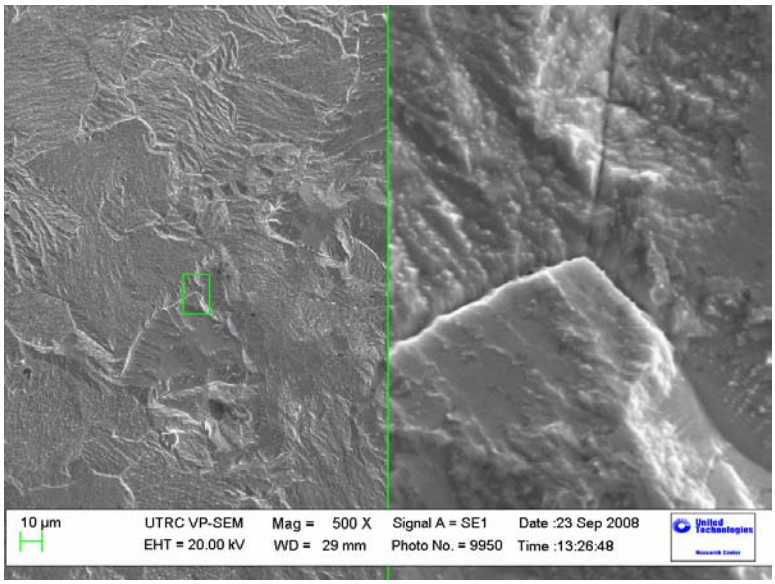

Figure 10: Tube from separator UTRC-5130 after three (3) hours with new etching procedure.

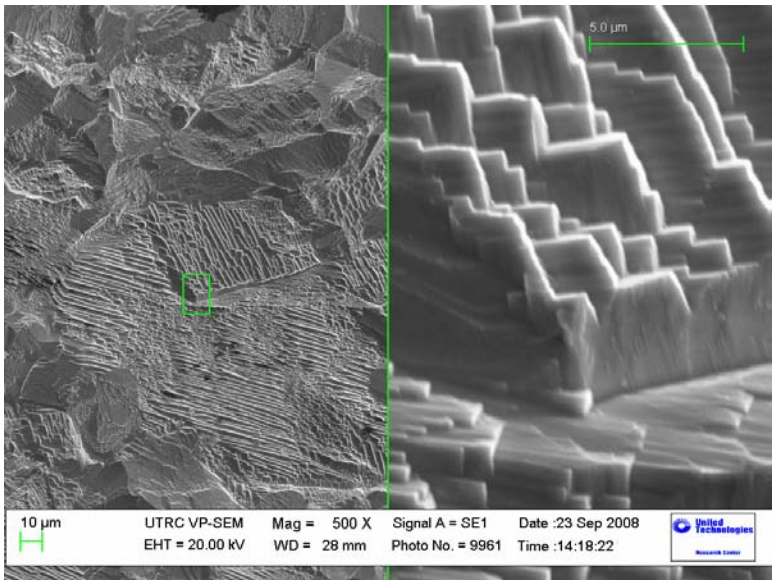

Figure 11: Tube from separator UTRC-5130 after overnight (approximately 12 hours) etching with new procedure.

Based on the weight loss data, solution elemental analysis, and SEM images, it appeared that an etching time between one (1) hour and three (3) hours would be sufficient to remove the binary surface layer on the separators. Two UTRC alloy separators were etched in situ. One of these was etched initially for one hour, which resulted in no significant improvement in hydrogen permeability. After an additional one-hour etch, the separator appeared to develop a leak when heated up to 350 °C. The other separator was etched in situ for three hours and also developed a leak when tested at 350 °C.

The separator that was etched in situ for three hours was cut open to do a root cause analysis on the source of the leak. It was expected that a stainless steel weld or other key

steel section had been over-etched. However, the leak testing showed that there were only a few leaks on two of the tubes within the separator. Figure 12 shows an SEM image of one of the tubes that had developed leaks with clear evidence of a crack in the sample. It was suspected that the leak points were due to preferential etching of places in the membrane where there was internal stress, and once this stress was relieved, cracks developed.

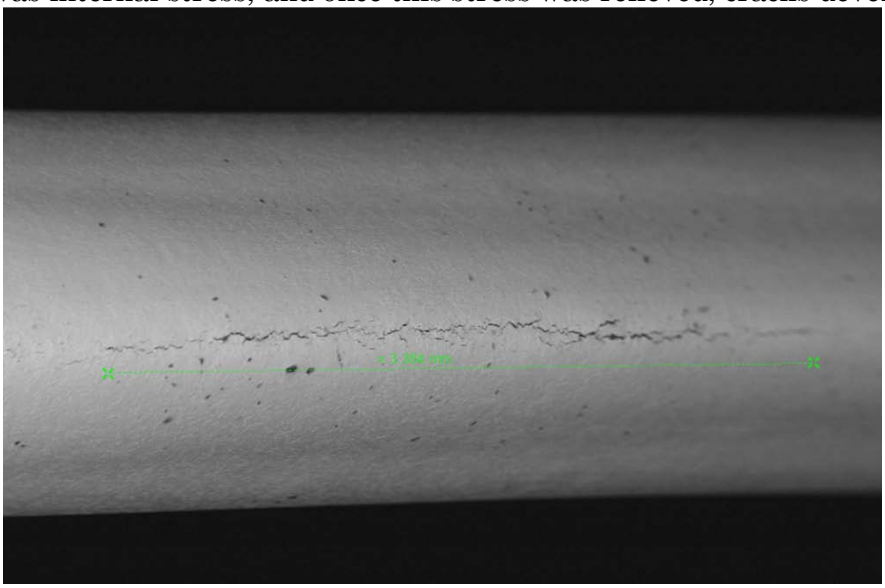

Figure 12: SEM image of tube from ternary separator after in situ etching, showing crack from stress relief.

2.1.2.3 Fabrication of Modified BCC Ternary Alloy Tubes

Based on the in situ etching results, UTRC began working with Power+Energy to produce new ternary alloy tubes without the surface binary layer and then make additional separators with those tubes. In the event that theoretically modeled solubility of the ternary element TM in the PdCu was inaccurate, the processing of the tubes could have been responsible for TM segregation at the surface which would lead to the binary surface layer. As a result, the composition of these new tubes was adjusted to reduce the TM concentration.

The new batch of ternary alloy tubes arrived at UTRC from Power+Energy in April 2009. The initial plan was to characterize the tubes and etch them to remove any barrier compounds on the surface. However, the initial characterization results, including XRD and EBSD, showed that the new tubes did not have a surface barrier layer and were also in the FCC phase, not the BCC phase.

The presence of the FCC phase suggested that Power+Energy's proprietary heat treatment and brazing procedures might be the source of the previous material's BCC phase as well as the binary surface barrier layer. As a result, an experiment was performed to try and convert a tube from the FCC phase to the BCC phase. A small piece of tube was placed in a quartz tube furnace and heated in hydrogen from 400 °C to 835 °C followed by a one hour hold at the high temperature. At this point, the tube should clearly have been in the FCC phase. The tube was then rapidly cooled to 410 °C, still in hydrogen, and held at that temperature for 36 hours before cooling down to room temperature. The temperature profile and gas flow rates for the experiment are given in Figure 13.

This heat treatment resulted in the conversion of the tube from the FCC phase to the desired BCC phase. The X-ray diffraction patterns for the tube before and after heat treatment are given in Figure 14. XPS and EBSD characterization of the tube sample after processing indicated that the tube had picked up some carbon contamination from the furnace, but that the barrier layer was not present. This meant that by reducing the concentration of the ternary element slightly for this second tube batch, the formation of the binary barrier compound was avoided.

Based on the initial success of this heat treatment experiment, additional experiments were performed using UTRC's INEL X-ray diffractometer equipped with an environmental chamber. The INEL system is capable of collecting X-ray diffraction patterns while flowing gases through the chamber at temperatures up to 1000 °C. Power+Energy provided UTRC information on their proprietary heat treatment protocol. Using that information, experiments were performed using the INEL system to match the temperatures and times as closely as possible while flowing nitrogen through the environmental chamber.

Two sets of INEL experiments were performed. One involved putting a tube sample through the Power+Energy temperature cycle three times; the second involved only doing it twice. The experiments showed that after the first, and possibly the second, heating cycle, the alloy could be converted from the FCC phase to the BCC phase and back again. However, at the end of one of the second cycles and at the end of a third cycle, the tube did not convert completely to the bcc phase. In addition, EBSD and XPS analysis detected the presence of an oxide at the surface, most likely due to oxidation of the ternary element. It was possible that in the INEL system, parts per million level concentrations of oxygen or water could have been present in the environmental chamber that caused this oxidation.

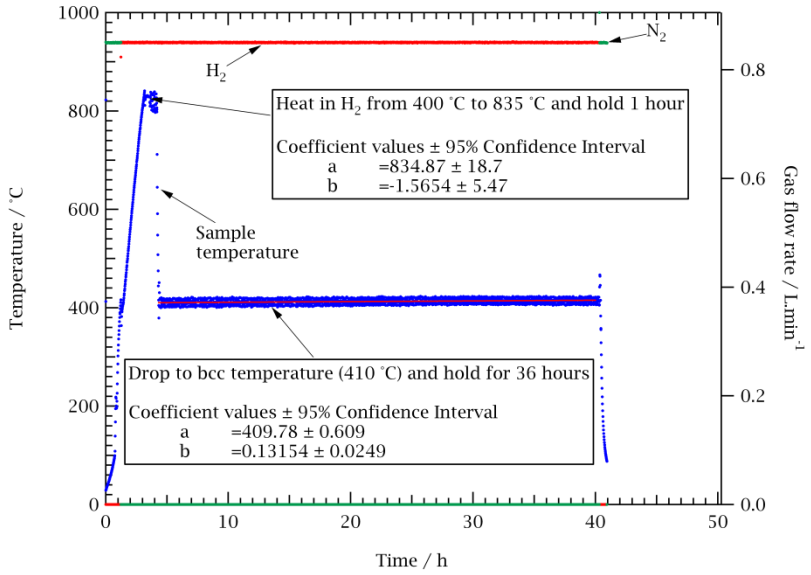

Figure 13: Initial heat treatment in hydrogen of a new PdCuTM alloy tube at UTRC. Heating for 36 hours at 410 °C after 1 hour at 835 °C in a hydrogen atmosphere resulted in a transformation from the FCC phase to the bcc phase.

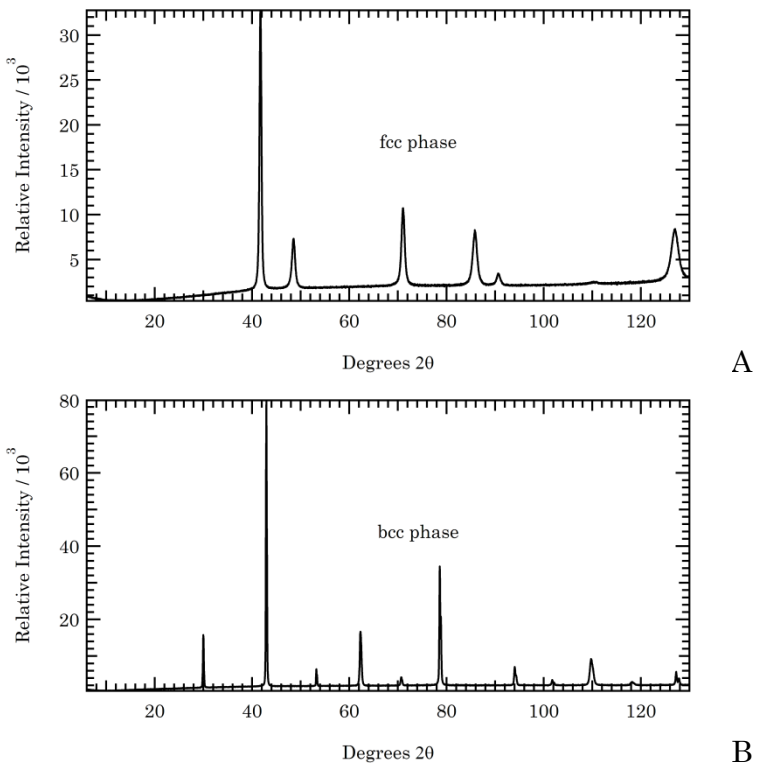

Figure 14: X-ray diffraction patterns before (A) and after (B) heat treatment in hydrogen for more than 36 hours.

Based on the above information, UTRC worked with Power+Energy to modify their heat treatment protocols to allow a background of hydrogen to be present during processing of the tubes to prevent oxidation. In addition, a hold at 450 °C in hydrogen was added to the cycle in an attempt to improve the nucleation and growth of the BCC phase. Tubes were sent back to Power+Energy for heat treatment. At the end of the processing, one tube was kept for single tube permeability testing at Power+Energy to check the hydrogen separation properties, while another was sent back to UTRC for detailed characterization.

Section 2.1.4.1 gives the detailed results for the single tube separator tests. The performance of the new membranes was not what was expected from a BCC PdCu alloy but closer to that expected for an FCC $Pd_{60wt\%}Cu_{40wt\%}$ alloy.

Detailed high temperature X-ray diffraction (XRD) experiments were carried out on an as-received tube in an attempt to understand the unexpected low permeability of the bcc ternary alloy. The experiments were run in an INEL diffractometer equipped with a heating chamber and a CPS-120 position sensitive detector. To prevent oxidation of the alloy, hydrogen gas was used at a flow rate of 315 cm^3/min. The sample was heated from 450 °C to 784 °C in increments of 50 °C and held at each temperature for 2 hours. A room temperature XRD scan prior to the high temperature test revealed a fully bcc microstructure. Upon heating, the bcc structure was observed to be stable up to 600 °C at which time the crystal structure was found to be a mixture of BCC and FCC. At 650 °C the structure was fully FCC and was stable up to 784 °C which was the temperature limit for this test. The sample was then cooled to 450 °C and held for 2 hours upon which the crystal

structure immediately transformed back to the bcc structure. Figure 15 below shows a 3-D plot of the high temperature X-ray diffraction data as a function of temperature.

In addition to the high temperature XRD studies performed on an as-received tube, a detailed characterization study was performed on the single brazed tube which had previously undergone permeability testing at Power and Energy and at UTRC. Room temperature XRD showed a fully bcc structure as can be seen in Figure 16. Electron backscattered diffraction (EBSD) was used to examine the crystal structure on the inner and outer diameter of the same post-permeability tested tube. Figure 17 below shows an inverse pole figure (A), and a phase map (B) indicating that the grains at the surface of the ID were BCC.

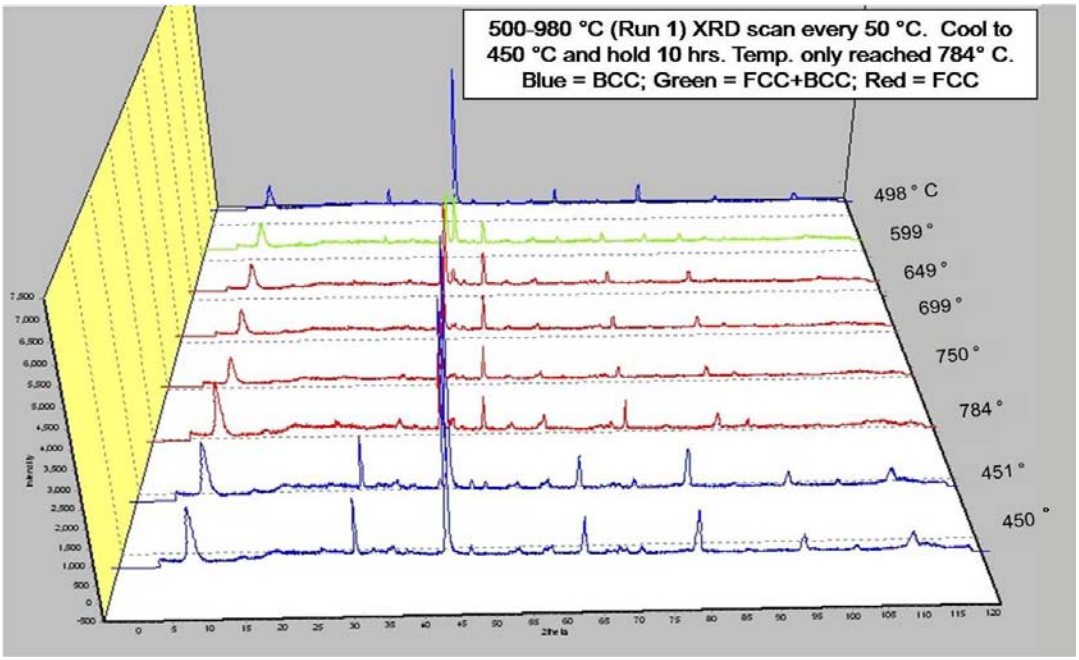

Figure 15: High temperature XRD scans of the ternary alloy show that the alloy was stable BCC up to 500 °C and was FCC above 650 °C. Cooling back down to 450 °C resulted in rapid transformation back to the BCC phase.

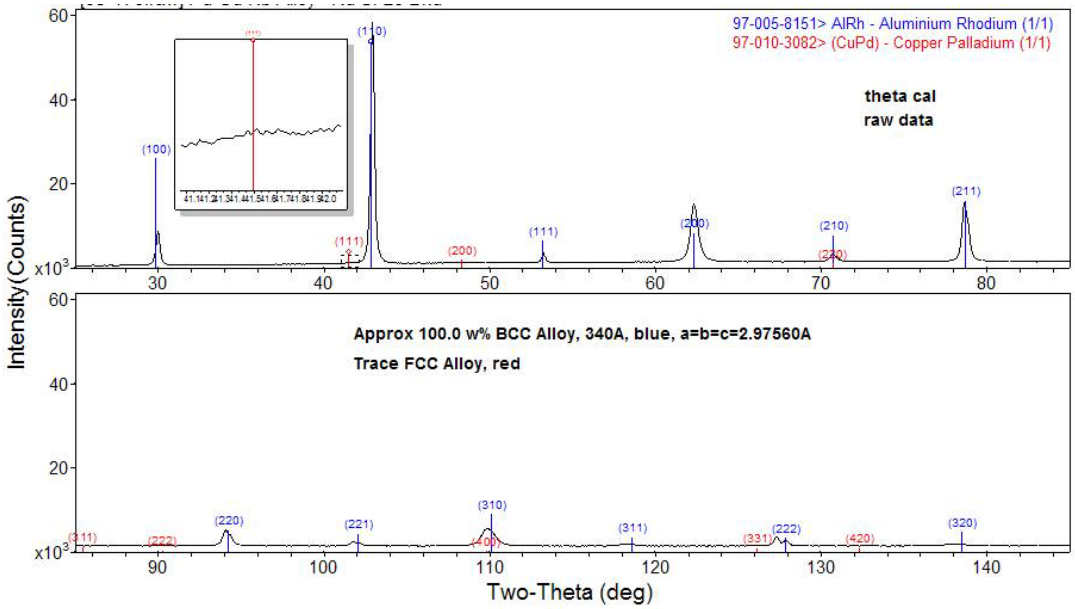

Figure 16: XRD scan of a single brazed tube after hydrogen permeability testing shows a fully bcc structure.

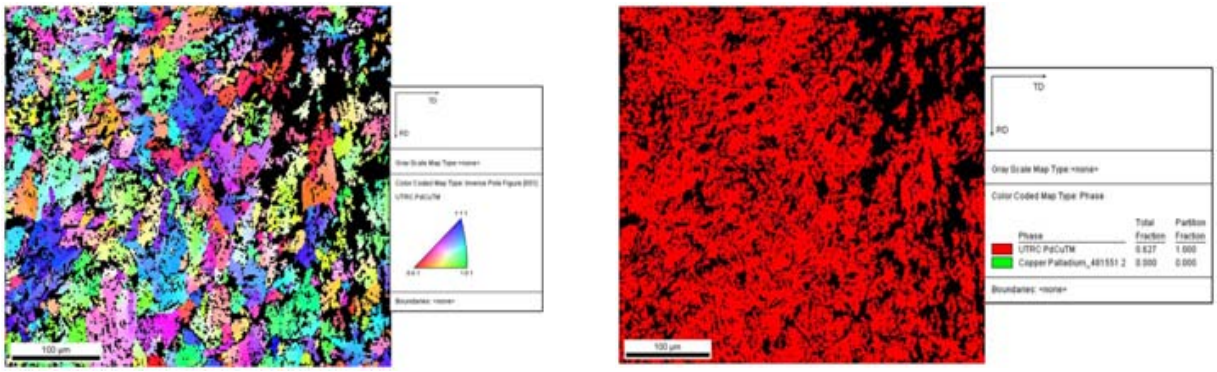

A B

Figure 17: (A) EBSD inverse pole figure showing grain size and orientation and (B) EBSD phase map showing the surface of the ID of the tube is bcc.

2.1.2.4 XPS Characterization & Chemical Etching of Ternary Alloy Tubes

X-ray photoelectron spectroscopy (XPS) was used to check the surface of the tube for any type of contamination (oxidation or formation of second phase). A depth profile was performed on the top 90 nm of the ID of the tube by using an argon ion beam to sputter the surface. The results are shown below in Figure 18, and indicate that only a small amount of adsorbed carbon existed on the surface. Since the permeability of this alloy composition should theoretically be much higher than that of the Power+Energy FCC PdCu alloy, and that the permeability in PdCu alloys is driven primarily by hydrogen diffusivity rather than solubility, more detailed, angle-resolved, small angle XPS analysis was performed on the tubes to determine the root cause for the lower permeability.

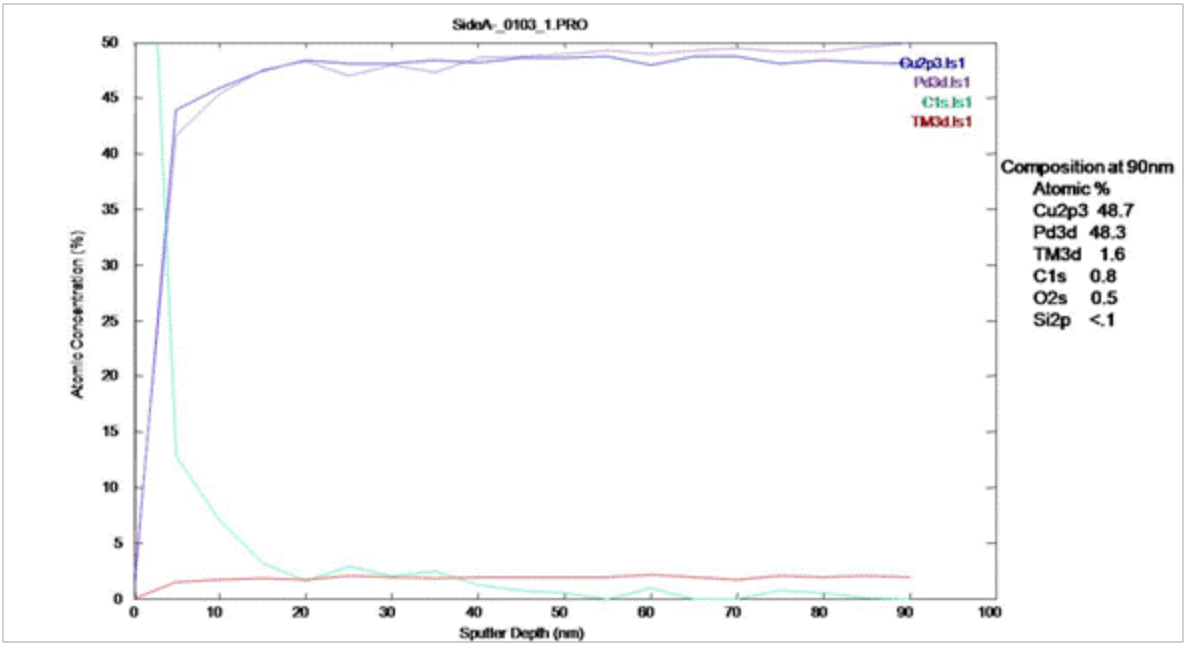

Figure 18: An XPS depth profile shows adsorbed carbon on the top 5-10 nm. Further angle-resolved work is in progress to check for the presence of surface oxidation.

Table 7 shows the surface concentrations of copper, palladium, and the ternary element obtained from low angle XPS measurements on different tube samples. Also listed in the table is the desired composition of the ternary alloy and the copper to palladium ratio. From Table 7, it can be seen that in the upper few nanometers of the single tube separator, which was tested at both Power+Energy and UTRC, the composition was different from the desired values. The surface of the tested tube appeared to have a higher concentration of the ternary element in an oxide form with a layer just below it that was depleted in the ternary element. The ternary oxide was not in a high enough concentration to cover the whole surface. However, the segregation of the ternary into an oxide phase leaves behind a PdCu phase with the wrong copper to palladium ratio (Cu/Pd = 1.20 versus a target of 1.11). It is known from the literature (McKinley, 1967 & 1969) that a PdCu alloy with less than 45at% Pd has a rather poor permeability compared to pure Pd.

Table 7: Low angle XPS surface concentration measurements of tested ternary alloy single tube and various etched, as-received tubes.

	Cu / at%	Pd / at%	TM / at%	Cu/Pd ratio
Targeted PdCuTM composition	52.25	47.00	0.75	1.11
P+E/UTRC tested ternary tube	53.57	44.64	1.79	1.20
As received tube (3-component etching solution; 3-h etch)	44.26	53.93	1.81	0.82
As received tube (3-component etching solution; 2-h etch)	38.48	60.59	0.93	0.64
As received tube (2-component etching solution)	59.48	39.64	0.88	1.50

Preliminary etching work was done on as-received tubes of the ternary alloy in an attempt to etch away the surface layer similar to the approach described in Section 2.1.2.1 for the original ternary alloy. Unlike the original alloy, the surface of the new as-received tubes was much more resistant to etching. This is shown in Table 7 for etching times of 2 to 3 hours with different etching solutions. Although it was more difficult to remove the ternary alloy from the surface, it was possible to adjust the copper to palladium ratio.

Since the copper to palladium ratio on the surfaces can effectively change the diffusion of hydrogen through the membrane, additional etching experiments were performed for longer times. The goal of those experiments was to focus only on adjusting the copper to palladium ratio rather than remove the ternary oxide. Figure 19 shows the progress on etching with UTRC's standard 3-component etching solution developed for the first ternary alloy. There was a trend toward increasing the copper to palladium ratio as etching times were increased, although times in excess of 100 hours would be necessary to adjust the ratio to the target value of 1.11, and the samples would be at risk of dissolving or thinning over that period.

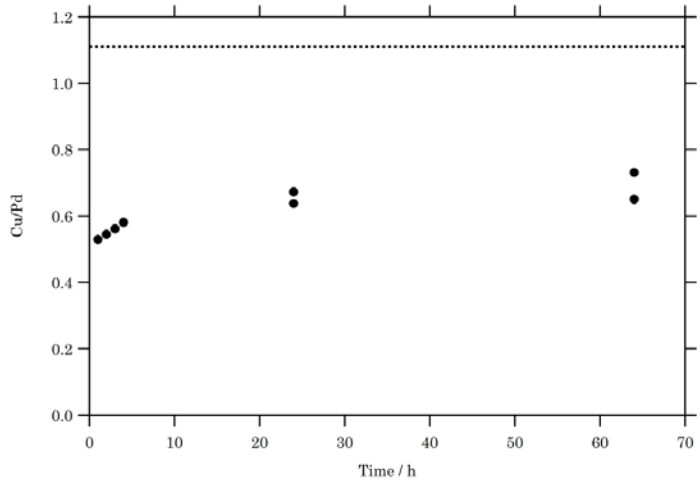

Figure 19: Surface Cu/Pd as a function of etching time for a 3-component etching mixture on as-received ternary PdCuTM tubes.

2.1.2.5 Mechanical Polishing of Ternary Alloy to Improve Performance

The dense metallic membrane effort became focused on alternative means to removing the unwanted TM-oxide scale from the ternary alloy tubes. Grazing angle XPS data showed a TM-oxide phase at the surface which was removed upon sputtering. Etching was used to try to remove this layer, but subsequent XPS analysis shows that etching actually leads to selective dissolution of the copper, leaving the surface Pd-rich (see Section 2.1.2.4). It is known from the literature (McKinley, 1967 & 1969) that a PdCu alloy with greater than ≈50at% Pd has a rather poor permeability compared to pure Pd.

In an attempt to remove the surface oxide layer without preferentially changing the surface chemistry, a mechanical polishing method was used. Fine pipe cleaners loaded with diamond paste and varsol lubricant were used to polish the ID of the tubes as shown in Figure 20. Similarly, a fine cotton cloth was used with the same diamond paste to remove material from the OD.

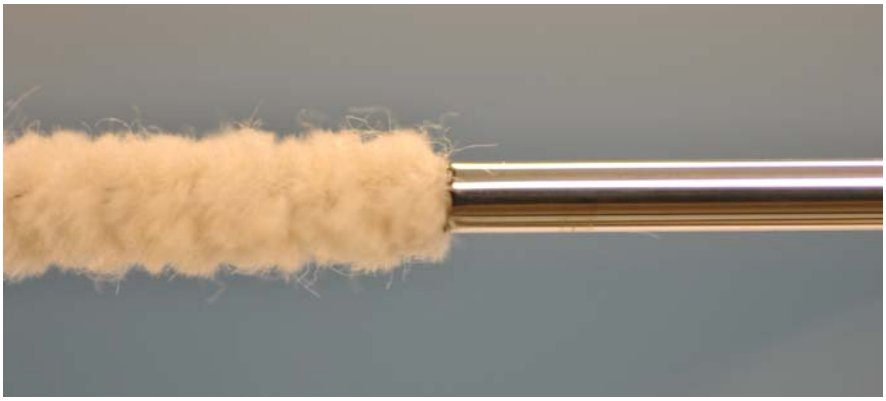

Figure 20: The setup used to polish the ID of the ternary alloy tubes.

A target weight loss of 2% was chosen in order to remove the TM-oxide, but limit the removal to less than 1 µm of material. The mechanically polished membranes were cleaned internally and externally with a delicate wipe soaked with varsol. They were then ultrasonically cleaned in 30 minute intervals in varsol, heptane, acetone, and ethanol. Finally, the membrane was dried in an oven at 130 °C for 2 hours. Table 8 below shows the initial and final weights of the first four tubes that were mechanically polished.

Table 8: Weight measurements of ternary alloy tubes before and after mechanical polishing.

Sample	Prior to removal (g)	Post removal (g)	% Wt. Loss
Tube 1	0.771	0.752	2.44
Tube 2	0.78	0.763	2.17
Tube 3	0.786	0.765	2.68
Tube 4	0.788	0.774	1.76

After mechanical polishing the tube surfaces were examined with Auger and XPS. Both techniques showed an artificial 25–50 Å surface layer that was Cu-rich and Pd-poor. This layer was caused by a thin 25–50 Å layer of adsorbed carbon and oxygen. The kinetic energy of the Cu Auger electrons is much greater than that of the Pd Auger electrons, thus Cu Auger electrons can escape more easily. This is what leads to the "false" enrichment of Cu at the surface. To verify this, a mechanically polished sample was analyzed and sputtered to a depth of 500 Å as shown in Figure 21. The sample was then left in air for 3 days and the same region was re-analyzed. Figure 22 shows that the surface was once again artificially Cu-rich due to the carbon and oxygen adsorbed on the surface. Thus, it was concluded that the actual surface chemistry was essentially the same as that observed in the bulk.

Mechanically polished tubes were sent to Power+Energy for fabrication into single tube separators for testing. The mechanically polished ternary alloy was tested in a single tube separator configuration (see Section 2.1.4.1). The data suggested that at 400 °C the ternary alloy has approximately twice the hydrogen permeability as the conventional FCC PdCu alloy. However, the polished membranes appeared to go through a phase transformation

from BCC to FCC at 450 °C, which is very similar to the original bcc PdCu alloy reported in the literature, and were not able to achieve the anticipated high hydrogen fluxes.

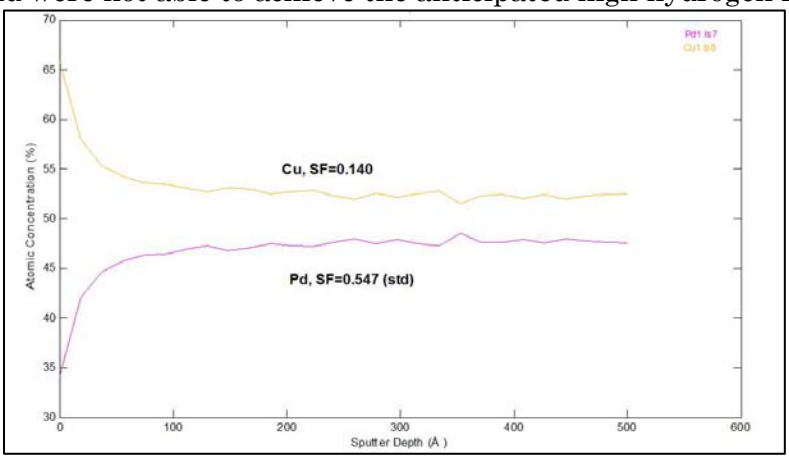

Figure 21: Auger depth profile after mechanical polishing shows no TM-oxide and a bulk composition very close to the 52.25 at%Cu-47 at% Pd target.

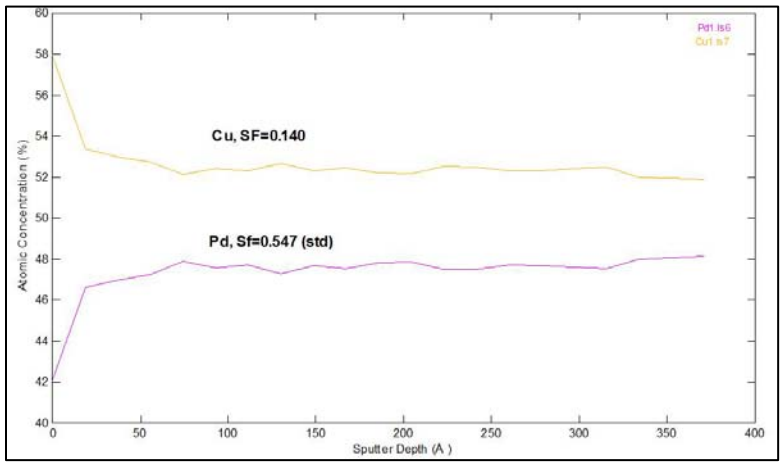

Figure 22: Auger depth profile of the same region as shown in Figure 21, after leaving the sample in air for 3 days.

2.1.3 Membrane Hydrogen Solubility Testing

Samples of both the initial ternary alloy and the FCC PdCu alloy tubes in the project were sent to Professor Ted Flanagan at Metal Hydride Technologies in 2008. Thermodynamic data were obtained for both alloys to determine, among other things, the hydrogen solubility of the materials. One of the key observations was that the Power+Energy FCC PdCu alloy had a hydrogen solubility similar to literature values for its composition. For the initial UTRC BCC PdCu alloy, the solubility was similar to that of the BCC PdCu metal Metal Hydride Technologies had evaluated as part of the modeling and experimental work under DOE contract DE-FC26-05NT42453.

Using the data from Metal Hydride Technologies, the solubility coefficient for the initial UTRC ternary alloy samples as a function of temperature was calculated. Figure 23 shows

the experimentally derived solubility coefficient versus the atomistic and thermodynamic modeling prediction for the alloy. On average, the experimentally derived solubility coefficient was a factor of two (2) lower than the modeling projection, which is a fairly good agreement between theory and experiment. As the permeability, and ultimately the flux, of hydrogen through Pd membranes is proportional to the product of the hydrogen diffusivity and the solubility, this suggests that the ternary membrane separator alloy tubes should have fluxes approximately half of that originally predicted by UTRC's atomistic models. However, this still meant that the hydrogen flux should be theoretically greater than what was initially observed without the interference of surface phases described in Section 2.1.4. Thus, hydrogen solubility was not the limiting factor in the performance of the ternary alloys evaluated during this project.

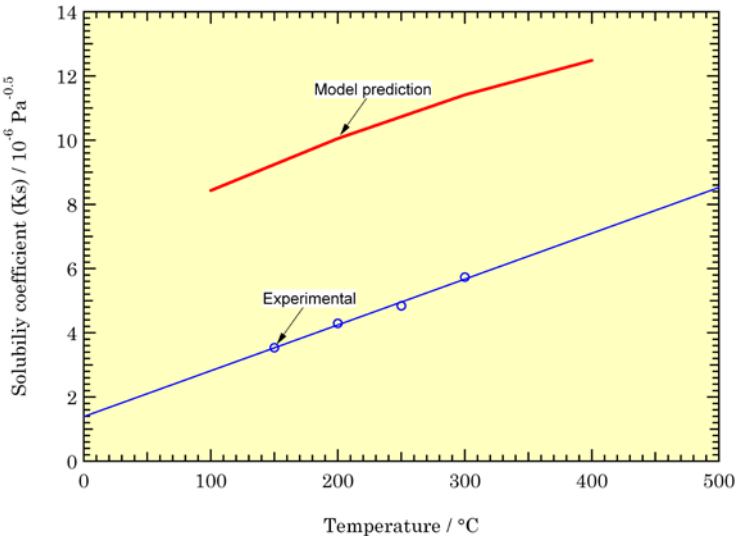

Figure 23: Experimentally derived solubility coefficient versus the model prediction as a function of temperature for the initial UTRC ternary alloy tubes.

2.1.4 Membrane Separator Testing

2.1.4.1 UTRC Alloy Separators

Initial testing of the first as-received UTRC ternary alloy separators indicated that the membranes were not performing well according to model predictions. The performance was below that of the FCC PdCu separators. Attempts were made to activate the UTRC alloy by leaving it under 6 atm of hydrogen pressure at constant temperatures on the assumption that the phase transformation from FCC to BCC was not 100% complete, but there were only small improvements to the hydrogen flux from the separator.

As described in Section 2.1.2.3, UTRC worked with Power+Energy to modify their heat treatment protocols to allow a background of hydrogen to be present during processing of a second batch of ternary alloy tubes to prevent oxidation. In addition, a hold at 450 °C in hydrogen was added to the cycle in an attempt to improve the nucleation and growth of the bcc phase. Tubes were sent back to Power+Energy for heat treatment. At the end of the processing, one tube was kept for single tube permeability testing at Power+Energy to

check the hydrogen separation properties, while another was sent back to UTRC for detailed characterization.

Figure 24 shows the hydrogen permeability data from Power+Energy on the single ternary alloy tube compared to other FCC PdCu separator data as well as data from the original Union Carbide patent on the BCC PdCu alloy (McKinley, 1969). The performance of the membrane was not what was expected from a BCC PdCu alloy but closer to that expected for an FCC $Pd_{60wt\%}Cu_{40wt\%}$ alloy (e.g., the 825 K data point from the McKinley data). The tube was sent back to UTRC for testing with similar results.

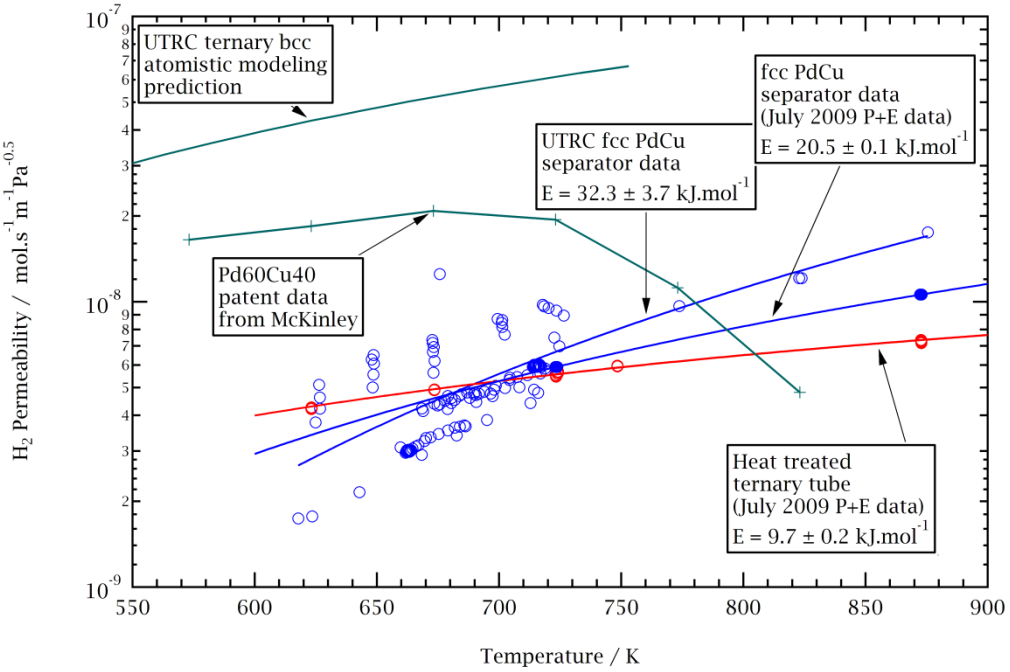

Figure 24: Permeability of FCC PdCu and single-tube ternary alloy separators compared to original UTRC atomistic modeling predictions and data from McKinley, 1969.

The mechanically polished ternary tubes described in Section 2.1.2.5 were sent to Power+Energy (P+E) for fabrication into single tube separators. The H_2 permeability testing results for a single tube ternary alloy separator compared to FCC and BCC PdCu data are shown in Figure 25. The data suggest that at 400 °C the ternary alloy has approximately twice the hydrogen permeability as the conventional FCC PdCu alloy from P+E. However, the polished membranes appear to go through a phase transformation from BCC to FCC at 450 °C which is very similar to the original bcc PdCu alloy reported by McKinley (McKinley, 1969). It may be that the addition of the ternary element to the bcc PdCu alloy widened the phase envelope enough to stabilize the composition, but it also shifted the composition at which the hydrogen permeability is maximized.

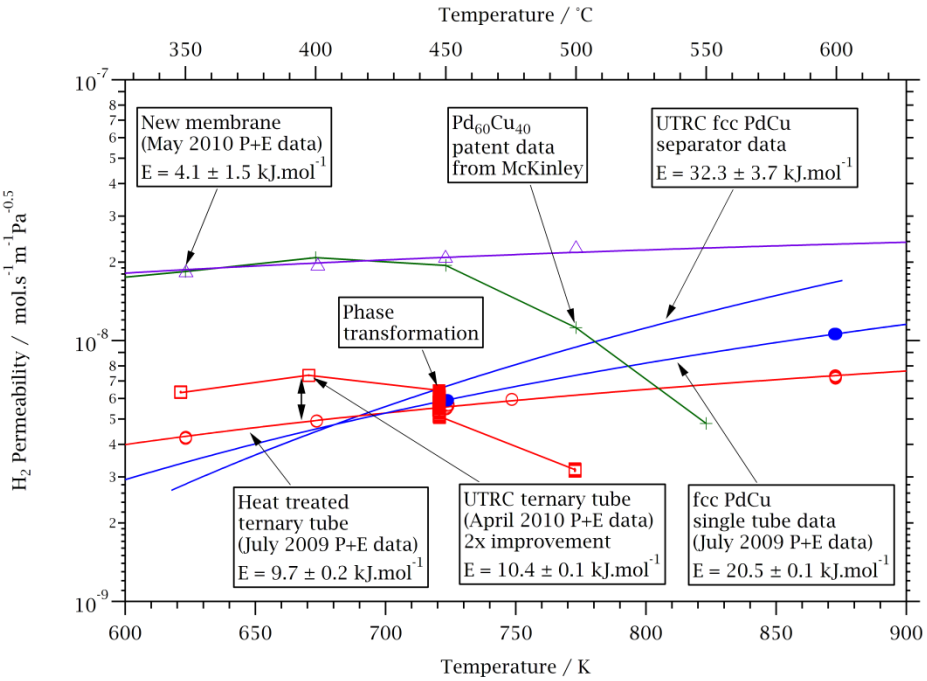

Figure 25: Permeability of FCC PdCu and single-tube ternary alloy separators compared to data from McKinley, 1969 for bcc PdCu. Also shown is the new membrane data from a P+E proprietary enhanced FCC PdCu tube.

2.1.4.2 Effect of Gas Species on FCC PdCu Alloy

One of the goals of the experimental program was to quantify the effect of different gas species on the PdCu alloy hydrogen permeabilities. Experience at UTRC has shown that the presence of non-pure hydrogen streams results in lower hydrogen permeabilities. By quantifying these effects in a permeability model, membrane performance can be better predicted over a wide range of gas compositions and pressures.

An FCC PdCu separator was tested at 123 distinct experimental conditions for nonlinear regression analysis of a permeability model. During these tests, the pressure was varied from 203 kPa to 620 kPa (29.4 psia to 89.9 psia) and the temperature was changed from 353 °C to 455 °C. The tests consisted of pure hydrogen feeds as well as different binary and ternary mixtures. It was not possible to determine the heats of adsorption for the various gases on the surface as all of those parameters were statistically insignificant. This may have been due to the narrow temperature range of the experimental program (≈100 °C) as well as the wide variation in hydrogen recoveries measured during the experiments. Thus, simple linear temperature terms were included in the model, which were found to be very significant in the regression adequacy checks.

The preliminary model results for the P+E FCC alloy permeability are given below. All of the gases had some effect on reducing the pure hydrogen permeability, but carbon monoxide had the strongest effect as evidenced by the larger adsorption coefficient. Figure 26 shows a comparison between the model prediction and an additional set of experiments where a combined five-gas mixture was fed to the separator. On average, the model predicted within 5% of the experimental result, with better agreement as the temperature

increased. Also shown in the Figure is the pure hydrogen permeability, which illustrates why the quantification of gas effect on permeability is so important.

$$Q_{\text{eff}} = \frac{Q_{H_2}}{1 + K_{CO}p_{CO} + K_{CO_2}p_{CO_2} + K_{H_2O}p_{H_2O} + K_{N_2}p_{N_2}}$$

$$Q_{H_2} = \exp\left(-18.795 + 4.8187\left(1 - \frac{673.15\ \text{K}}{T}\right)\right) = 8.5 \times 10^{-7} \exp\left(\frac{-26968}{RT}\right)$$

$$K_{CO} = \exp\left((-11.831 \pm 0.115) + \ln\frac{T}{673.15\ \text{K}}\right) = 1.08 \times 10^{-8} T$$

$$K_{CO_2} = \exp\left((-13.134 \pm 0.223) + \ln\frac{T}{673.15\ \text{K}}\right) = 2.94 \times 10^{-9} T$$

$$K_{N_2} = \exp\left((-13.551 \pm 0.111) + \ln\frac{T}{673.15\ \text{K}}\right) = 1.94 \times 10^{-9} T$$

$$K_{H_2O} = \exp\left((-13.6 \pm 0.156) + \ln\frac{T}{673.15\ \text{K}}\right) = 1.84 \times 10^{-9} T$$

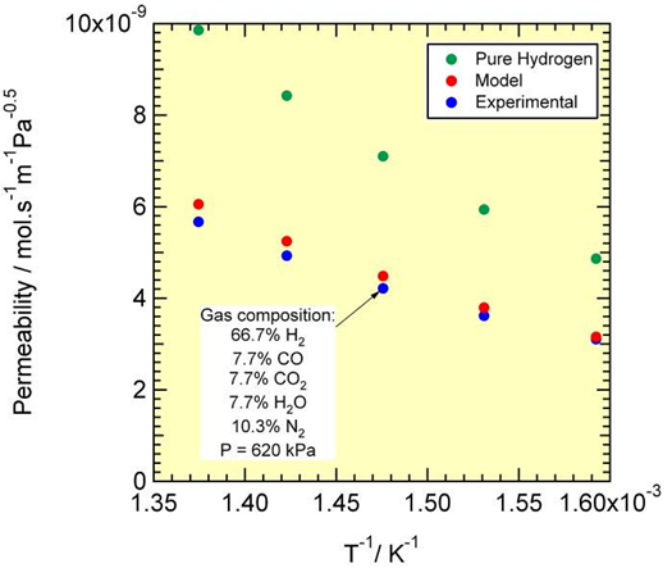

Figure 26: Comparison of permeability model prediction versus experimental data for a 66.7% H_2, 7.7% CO, 7.7% CO_2, 7.7% H_2O, 10.3% N_2 mixture as a function of temperature. The permeability of pure hydrogen is given for reference to show the effect due to the presence of other gas species. The preliminary model for P+E's PdCu alloy shows a mean average agreement of 5.2% between the model and the experimental data. At 450 °C the agreement was approximately 1% and at 350 °C it was approximately 6%.

After the preliminary permeability model was established, additional high pressure data was obtained using the high pressure reformer rig (Section 2.1.4.3) on both pure hydrogen and gas mixtures. Using the additional data, the model was updated and is shown in the following equations, where Q_i is the H_2 permeability in units of $mol.s^{-1}m^{-1}Pa^{-0.5}$ and the species partial pressures are in Pa. As with the previous modeling effort, the gas species adsorption terms had to be fitted to simple linear functions to get a statistically

significant result as it was not possible as yet to determine the effective heats of adsorption terms and fit an Arrhenius type function.

$$Q_{\text{eff}} = \frac{Q_{H_2}}{1 + K_{CO}p_{CO} + K_{CO_2}p_{CO_2} + K_{H_2O}p_{H_2O} + K_{N_2}p_{N_2} + K_{H_2S}p_{H_2S}}$$

$$Q_{H_2} = \exp\left(-19.085 + 5.6365\left(1 - \frac{689.9\ \text{K}}{T}\right)\right) = 1.4434 \times 10^{-6} \exp\left(\frac{-32330}{RT}\right)$$

$$K_{CO} = \exp\left((-12.748 \pm 1.008) + \ln\frac{T}{689.9\ \text{K}}\right) = 4.22 \times 10^{-9}T$$

$$K_{CO_2} = \exp\left((-15.107 \pm 2.340) + \ln\frac{T}{689.9\ \text{K}}\right) = 3.98 \times 10^{-10}T$$

$$K_{N_2} = \exp\left((-14.859 \pm 1.046) + \ln\frac{T}{689.9\ \text{K}}\right) = 5.11 \times 10^{-10}T$$

$$K_{H_2O} = \exp\left((-15.386 \pm 1.531) + \ln\frac{T}{689.9\ \text{K}}\right) = 3.01 \times 10^{-10}T$$

$$K_{H_2S} = \exp\left((-4.569 \pm 1.345) + \ln\frac{T}{689.9\ \text{K}}\right) = 1.50 \times 10^{-5}T$$

The need to use linear functions was partly due to the limited temperature range of the data collected. Although as temperature increases, this model eventually predicted that the gas species will have a stronger adsorption effect, the magnitude of the coefficients can be used for temperatures near the mean of the experiments (416.8 °C) to examine the impact of the different gas species. Inspection of the adsorption coefficients in the above equations showed that the effect of H_2S was much greater than that of CO, which in turn was an order of magnitude greater than the other gas species. These results have a practical implication for the DOE's membrane targets. At 400 °C, the presence of H_2S and other gases in the concentrations specified in the DOE membrane test protocol can result in up to a 50% decrease in membrane permeability. As a result, for a membrane to perform at a flux of 200 $ft^3ft^{-2}h^{-1}$, that membrane may need a pure hydrogen flux capability of 400 $ft^3ft^{-2}h^{-1}$.

At the end of the project, the same permeability model approach was used to characterize the performance of the enhanced FCC PdCu alloy (Section 2.1.4.6). The measurements were made on non-sulfur containing gases mixtures. However, the experiments were conducted such that the measured hydrogen recoveries were low (<10%). This in turn improved the quality of the parameter estimation and resulted in qualitatively similar results to the above models, in that CO was the only significant gas that had impact on the hydrogen permeability. In addition, it was possible to fit the CO adsorption term to a typical exponential temperature relationship and properly account for the impact of temperature.

2.1.4.3 Dedicated High Pressure Testing Rig

There were two test stands dedicated for this project. The first test stand was a low pressure (<6 atm) laboratory testing rig that used house gases, such as hydrogen, combined with gas cylinders, to evaluate membrane performance. The second was a high pressure (>10 atm) testing rig that used compressed reformate from a diesel reformer and mixed it with steam and additional poisons from gas cylinders to evaluate membrane separator durability and performance.

The high pressure rig construction was completed in 2008. Figure 27 shows a photograph of most of the testing rig as it neared completion in mid-2008. In June 2008, the new DOE standard testing protocol was made available to UTRC for evaluating hydrogen separators (Driscoll, 2008). As construction on the high pressure rig came to an end, the low pressure testing rig was thus modified to accommodate the new DOE testing protocol.

The low pressure test rig was used for the majority of the data obtained in the project and was subsequently modified for higher pressure testing (up to 200 psig). One of the limitations of the low pressure rig was that it used house hydrogen generated by an electrolyzer system, which was limited to 75 psig. The new DOE protocol presented conditions that were not achievable with the reformer system in the high pressure rig and thus it was used for limited testing (such as the 120 hour durability test shown in Section 2.1.4.4) until the low pressure rig was upgraded.

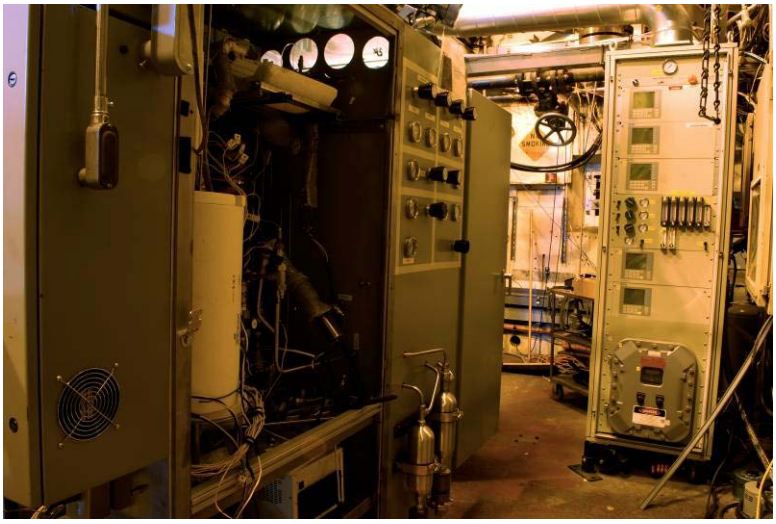

Figure 27: High pressure (>10 atm) Pd membrane test rig under construction. The left portion of the picture contained the testing section which included heaters for the hydrogen separators, the logistic fuel reformer, and steam generator. At the far right of the image is the continuous gas analyzer system.

2.1.4.4 Performance of FCC PdCu Alloy

2.1.4.4.1 FCC PdCu Hydrogen Flux

Much of the hydrogen flux data obtained on the FCC PdCu alloy separators was primarily at 100 psig H_2 feed pressure using either hydrogen or a mixture of hydrogen with nitrogen and hydrogen sulfide (H_2S). A summary of the performance data on three of the Power+Energy FCC PdCu alloy separators is given in Table 9. The highest hydrogen flux obtained with the FCC PdCu alloy separators was 61.03±0.01 $ft^3h^{-1}ft^{-2}$ at an operating temperature of approximately 600 °C. Figure 28 shows the data from Table 9 in graphical form.

Table 9: Performance data at high H_2 partial pressure (100 psig) obtained on three Power+Energy FCC PdCu alloy separators. Permeate pressure was at atmospheric pressure for all experiments. All data are reported with 95% confidence limits.

Separator: P+E-5123	**50% H_2/50% N_2**	
Temperature / °C	H_2 Feed Pressure / psig	Flux / $ft^3h^{-1}ft^{-2}$
342.5 ± 0.1	92.66 ± 0.02	16.27 ± 0.06
382.4 ± 0.5	92.68 ± 0.04	20.20 ± 0.26
397.7 ± 0.3	92.63 ± 0.05	21.58 ± 0.22
443.0 ± 0.8	92.64 ± 0.03	28.41 ± 0.49
511.2 ± 0.4	92.69 ± 0.06	32.83 ± 0.55

Separator: P+E-5123	**100% H_2**	
Temperature / °C	H_2 Feed Pressure / psig	Flux / $ft^3h^{-1}ft^{-2}$
402.6 ± 0.2	111.72 ± 0.04	46.78 ± 0.02

Separator: P+E-5124	**50% H_2/50% N_2**	
Temperature / °C	H_2 Feed Pressure / psig	Flux / $ft^3h^{-1}ft^{-2}$
549.8 ± 0.2	99.98 ± 0.03	32.89 ± 0.07
553.1 ± 0.8	100.08 ± 0.08	32.42 ± 0.10

Separator: P+E-5124	**100% H_2**	
Temperature / °C	H_2 Feed Pressure / psig	Flux / $ft^3h^{-1}ft^{-2}$
351.7 ± 0.3	100.00 ± 0.29	13.14 ± 0.11
400.0 ± 0.4	100.00 ± 0.16	19.60 ± 0.04
449.4 ± 0.4	100.06 ± 0.13	26.09 ± 0.07
500.6 ± 0.4	99.88 ± 0.14	33.58 ± 0.06
549.7 ± 0.4	99.96 ± 0.13	42.01 ± 0.03
550.6 ± 0.3	100.03 ± 0.12	42.14 ± 0.05
602.3 ± 0.2	100.06 ± 0.11	**61.03 ± 0.01**

Separator: P+E-5124	**50% H_2/50% N_2**	**487±4 ppm H_2S**
Temperature / °C	H_2 Feed Pressure / psig	Flux / $ft^3h^{-1}ft^{-2}$
558.6 ± 0.1	100.00 ± 0.02	**31.16 ± 0.05**

Separator: P+E-5125	**50% H_2/50% N_2**	
Temperature / °C	H_2 Feed Pressure / psig	Flux / $ft^3h^{-1}ft^{-2}$
450.7 ± 0.4	99.97 ± 0.03	19.27 ± 0.13

Separator: P+E-5125	**100% H_2**	
Temperature / °C	H_2 Feed Pressure / psig	Flux / $ft^3h^{-1}ft^{-2}$
451.5 ± 0.1	99.98 ± 0.02	26.11 ± 0.06

Separator: P+E-5125	**50% H_2/50% N_2**	**20±1 ppm H_2S**
Temperature / °C	H_2 Feed Pressure / psig	Flux / $ft^3h^{-1}ft^{-2}$
450.2 ± 0.1	100.00 ± 0.02	**25.69 ± 0.02**

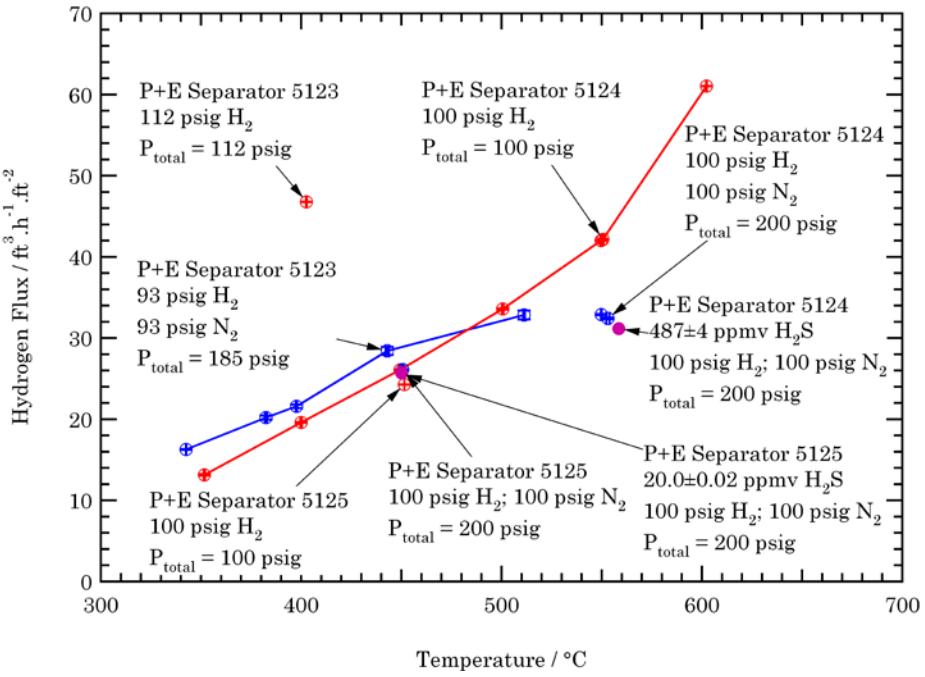

Figure 28: Hydrogen fluxes of different Power+Energy PdCu alloy separators obtained at 100 psig H_2.

2.1.4.4.2 Temperature and Pressure Limits of FCC PdCu Separator Units

The initial tests in the high pressure rig were done with the P+E alloy separator 5123. This separator had been used previously to generate data at lower pressures and with different gas compositions. Unfortunately, the thermal management system on the new test rig was not fully optimized during these higher pressure, higher flow tests. In attempts to generate high pressure hydrogen data at elevated temperatures (e.g., 550–600 °C), the furnace around the separator eventually reached a temperature of 770 °C. This temperature exceeded the recommendation for maximum operation temperature given by Power+Energy and the separator developed a leak. As a result only the reliable data for separator 5123 are reported in Table 9 and Figure 28.

2.1.4.4.3 Sulfur Tolerance of FCC PdCu Separator Units

A key objective of this project was to evaluate the resistance of the P+E "best in class" and UTRC ternary alloys to different poisons, especially sulfur. Due to the leak in separator 5123, a new FCC PdCu alloy unit, separator 5124, was selected for testing. The separator's performance was measured at 100 psig pure H_2 to obtain the ideal flux data. The separator was then evaluated twice with a 50% H_2/50% N_2 mixture at a total pressure of 200 psig at 550 °C. This temperature was chosen for a high concentration sulfur experiment to maximize the hydrogen flux.

After the second 550 °C measurement, the H_2 was replaced with a 974±8 ppmv H_2S in H_2 supply. The resulting feed mixture thus contained 487±4 ppmv H_2S. The separator operated for approximately 4 hours without incident at a hydrogen flux that was within 5% of the data measured without sulfur. However, at the end of the 4-hour period, the measured flow on the hydrogen permeate side of the membrane began to increase slightly,

potentially indicating a nitrogen leak. After an additional 30 minutes of operation, the membrane failed completely and was unable to hold a back pressure of more than 40 psig. Nitrogen flow checks verified that the membrane had been compromised. The data for this experiment are shown graphically in Figure 29.

Based on the previous performance of this alloy in the presence of sulfur and the relative thickness of the membrane itself, alloy failure was not suspected to be the cause of this leak. Sulfur is known to affect stainless steel ("hot corrosion") as well as some palladium alloys. It was anticipated that operation at 550 °C would be hot enough to maximize the hydrogen flux, yet avoid sulfidation of the other materials of construction in the separator.

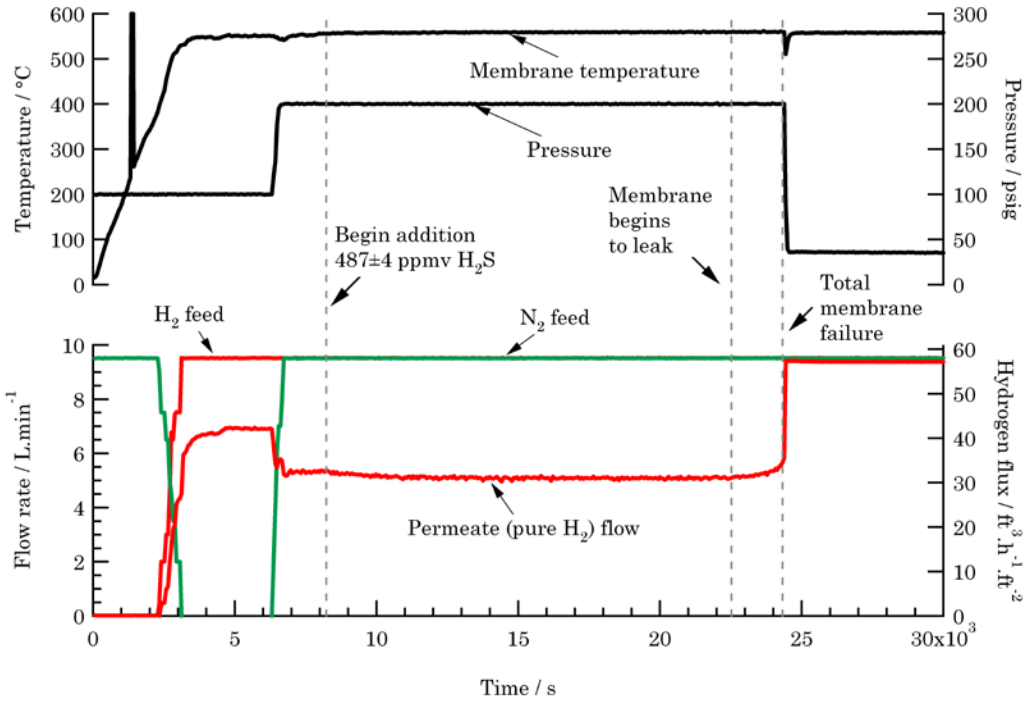

Figure 29: Experimental details of a 487±4 ppmv sulfur experiment on Power+Energy separator 5124. The separator operated for four (4) hours at 559 °C with a hydrogen flux of 31.2 $ft^3h^{-1}ft^{-2}$ before a leak developed. After 4.5 hours of operation, the separator failed completely and was unable to hold a pressure greater than 40 psig.

Based on the testing results for separator 5124, it was decided that the next sulfur test should be started with less aggressive conditions. To avoid sulfidation of stainless steel, a lower feed concentration of 20 ppmv H_2S and an operating temperature of 450 °C were chosen for the next test. The next membrane unit, separator 5125, was tested at 450 °C with a H_2 partial pressure of 100 psig. Both pure H_2 and 50% H_2/50% N_2 were used to evaluate the performance of the separator, which had a hydrogen flux comparable to separator 5124. The separator was then fed a 50% H_2/50% N_2 mixture containing 20 ppmv H_2S for 24 hours. The separator did not fail, although the hydrogen flux increased slightly during the run. However, the final measured hydrogen flux was within the range of

that measured for separator 5124 and a nitrogen flow check confirmed that the separator was leak-free after the sulfur testing. The data for this experiment are shown graphically in Figure 30. Although the 20 ppmv H_2S test was for a limited duration, it demonstrated that the FCC PdCu alloy can meet the DOE's 2012 sulfur metric. There was also evidence that the alloy can withstand much higher sulfur concentrations based on the 487 ppmv H_2S test.

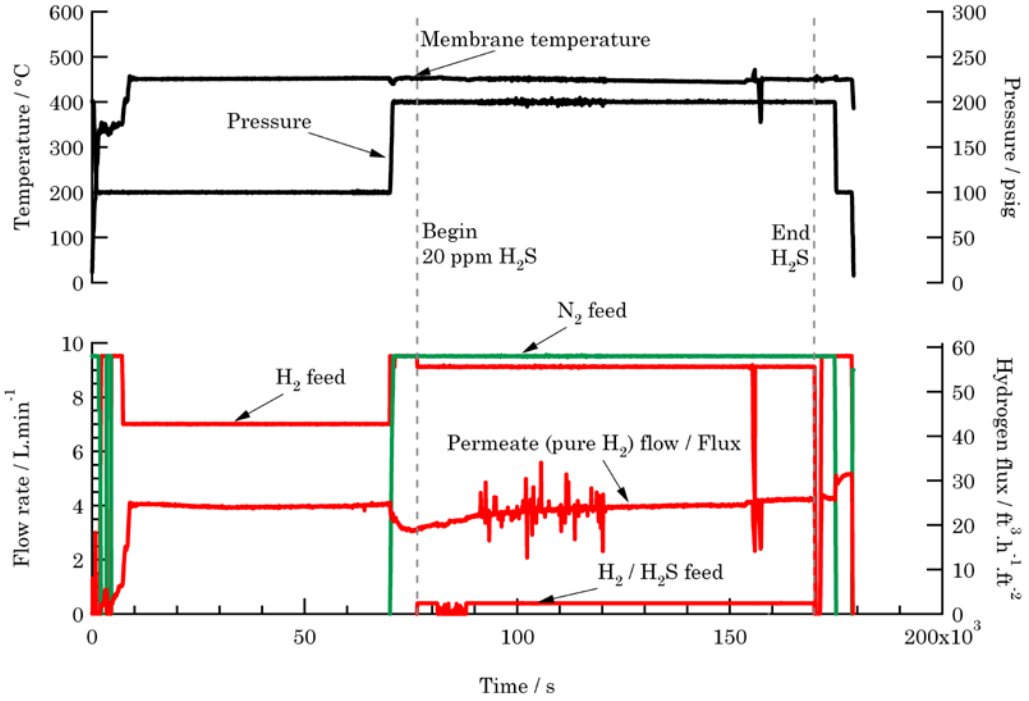

Figure 30: Experimental details of a 20 ppmv sulfur experiment on Power+Energy separator 5125. The separator was operated for 24 hours at 450 °C without failure.

2.1.4.4.4 Ammonia and Sulfur Tolerance of FCC PdCu Separator Units

Separator 5125 was operated for a total of 120 hours during another experiment, with the last 100 hours operated in the presence of 78 ppmv H_2S. The separator did not appear to degrade in performance due to the presence of such high levels of sulfur. At the end of the test, all gases were stopped and only nitrogen and water were fed to the separator. Approximately 20 hours later, the membrane developed a leak. In total, separator 5125 had been operated for more than 200 hours at temperatures above 400 °C and feed pressures of 290 psig.

Based on the characterization results from the preliminary root cause analysis (Section 2.1.4.4.5), showing that the tube failures occurred due to a tube defect and not the presence of high sulfur levels, as well as this failure; it was suspected that some tubes could not withstand such a high pressure at the operating temperature. As a result, when the next separator, 5126, was operated with the reformer in the high pressure testing rig, it was decided that the operating pressure should be reduced to 250 psig. The data for the testing of separator 5126 are shown in Figure 31.

Separator 5126 was tested for more than 300 hours with varying levels of sulfur and ammonia. The sulfur level was maintained at an average concentration of 33 ppmv H_2S, although this concentration was varied from 20 ppmv to 90 ppmv. At several points during

the run (e.g., 220 hours), the sulfur poisons were removed, resulting in a temporary increase in hydrogen flux which then lowered once the poison feed was restored. During the last 175 hours of the experiment, ammonia was fed to the membrane system via the steam at an average concentration of 9 ppmv.

Although the hydrogen fluxes were only in the range of 2.5–4 $ft^3ft^{-2}h^{-1}$ due to the gas composition, the effect of the sulfur and ammonia was otherwise negligible in terms of membrane durability. However, at approximately 310 hours, the sulfur was removed from the feed gases and the membrane was operated with only ammonia present. Shortly thereafter, the membrane developed a leak and eventually failed. This failure in the absence of sulfur, combined with the results for separator 5125, suggested that even 250 psig was too high a pressure for these particular separators to operate at for long periods of time.

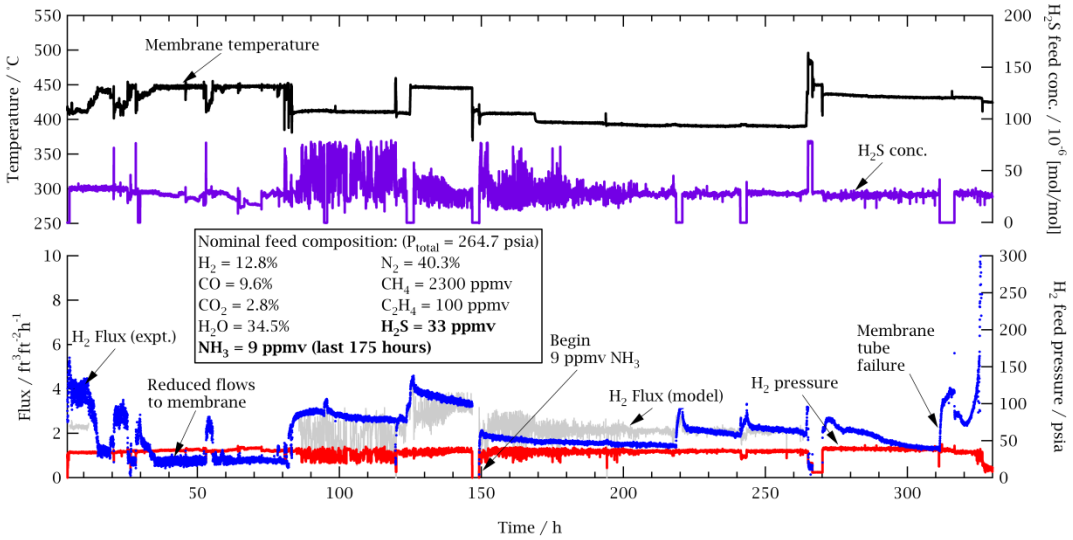

Figure 31: H_2 & H_2S feed concentrations, temperature, and H_2 flux for P+E membrane 5126 tested to failure. This membrane was operated for approximately 330 hours during the test in the presence of 20—90 ppmv H_2S with a typical feed concentration of 33 ppmv H_2S. In addition, the membrane was operated in the presence of 9 ppmv NH_3 for the last 175 hours of the run. Although the operating pressure for this experiment was reduced to 250 psig, around 320 hours into the run the separator developed a leak.

2.1.4.4.5 Root Cause Analysis for Separator Tube Leaks

The root cause for the failure of the P+E membrane separators is best described by the analysis performed on separator 5124, as all of the separator failures in this project followed the same mode. That separator developed a leak after 4 hours of operation at 550 °C with a H_2S feed concentration of 487±4 ppmv. The hypothesis at the time, in the absence of detailed characterization, was that sulfur aggressively attacked the stainless steel and welds within the separator resulting in leaks. Some of the stainless steel internals of the separator were indeed attacked by the sulfur, but the welds and stainless steel were still intact. It appeared that the PdCu alloy resisted attack by the sulfur as expected, but that a defect in one of the tubes at a grain boundary resulted in that single tube failing under the high pressure and temperature.

During the bubble test and leak checks on the failed separator, it was discovered that only one tube in the separator had failed. Figure 32 shows an image of the damaged portion of the failed tube. Note that all other parts of the separator appeared to be leak tight.

Figure 32: Image of failed membrane tube inside P+E FCC PdCu separator 5124 during a bubble leak test.

The failed tube and another undamaged tube were cut from the separator and submitted for characterization. Figure 33 shows a scanning electron micrograph of a magnified portion of the mounted cross-section of the failed portion of the tube. As shown in the Figure, there is an ≈30 μm section missing from the membrane at the failure point. This corresponds to the typical size of the grains in this membrane, which vary from 20–40 μm. Based on all of the microscopy work, it appears that there was a defect at a grain boundary, resulting in a very thin (≈10 μm) portion of the membrane tube. This thin a wall thickness was unable to hold back the 290 psig gas pressure at 550 °C, and eventually failed, causing the separator to leak.

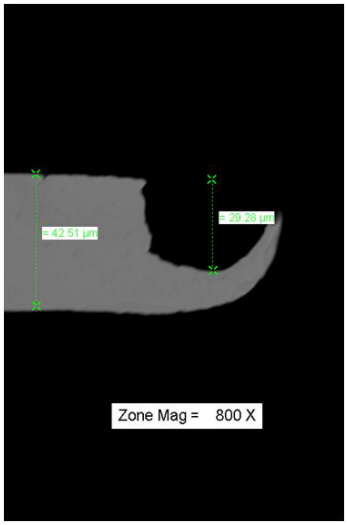

Figure 33: Scanning electron micrograph cross-section of the single tube of P+E membrane 5124 that failed showing a defect at the failure point.

Figure 34 is a micrograph of the failed cross-section, but with zone magnification on the inner diameter of the stainless steel tube. This portion of the tube was on the return side of the retentate in the separator, and sees the highest sulfur concentration. There was a scale ≈30 μm thick on the surface of the stainless steel tube. A similar, much thinner layer, was also present on the outer diameter. EDS maps and line scans of the stainless steel tube show that the scale contained on the order of 25 wt% sulfur in the form of iron and chrome compounds. This was consistent with sulfur causing *hot corrosion* of the stainless steel. However, EDS analysis of the membrane tube, particularly at the defect failure point, showed that there was no detectable sulfur inside the PdCu membrane. On the interior surface of the tube there are a few regions where there was 3–5 wt% sulfur, but that was consistent with sulfur adsorption on the surface during testing. At the defect site, there were also two particles that were primarily iron and chrome with a sulfur concentration on the order of 25 wt% sulfur, which may have been due to pieces of the scale from the stainless steel tube.

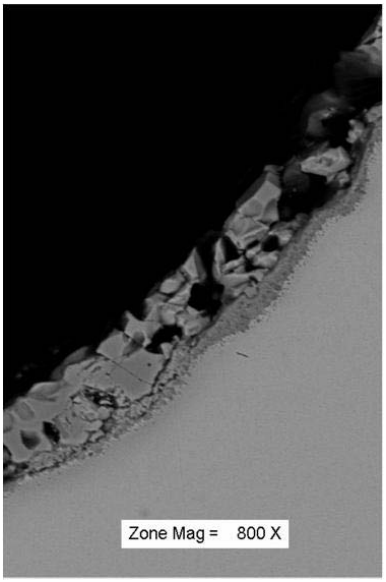

Figure 34: Scanning electron micrograph cross-section of the single tube of P+E membrane 5124 that failed showing the high sulfur content scale on the stainless steel tube that was inside the PdCu membrane tube.

Based on the evidence collected on all of the failed separators, it appeared that the PdCu alloy was not affected by sulfur, but that the stainless steel portions of the separator were being corroded. This sulfur-induced corrosion did not result in the leaks and separator failures. A defect in a single tube at a grain boundary failed, due to the high pressure and temperature of the test conditions.

Figure 35 shows a calculated membrane tube wall hoop stress as a function of the wall thickness. In the case of a defect such as that described above, the effective wall thickness was approximately 10 μm. At that pressure, the membrane wall can only withstand a pressure of 220.6 psig. This was consistent with the observation that the three separators tested at 290 psig and the one separator tested at 250 psig failed, yet the final separator operated for more than 500 hours without failure at 200 psia (see Section 2.1.4.5).

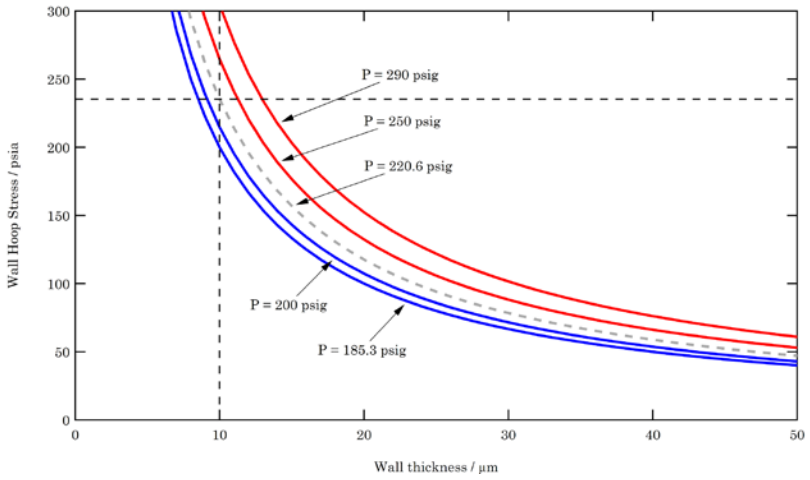

Figure 35: Membrane tube wall hoop stress calculated as a function of wall thickness.

2.1.4.5 DOE Testing Protocol of FCC PdCu Alloy

As described in Section 2.1.4.3, UTRC's low pressure testing rig was modified to perform testing at 200 psia according to the DOE membrane testing protocols (Driscoll et al., 2008). The rig did not have a sweep flow on the permeate side of the membrane nor a vacuum pump, so it was be possible to evaluate performance under the Test 2c conditions. The Test 2c feed gas contains only 9.6 psia of hydrogen in the feed, and as this is lower than atmospheric pressure on the permeate side, it would have resulted in no driving force through the membrane and thus no flux.

The last FCC PdCu separator (P+E 5127) using Power+Energy's alloy began testing under the DOE protocol toward the end of the project. The separator was tested for a total of 527 hours under DOE protocol test conditions 1, 2a, and 2b, including some pure hydrogen flux checks and brief nitrogen leak checks. The data for the entire protocol testing is shown in Figure 36 and a summary of the hydrogen flux results is given in Table 10.

After an initial pure hydrogen flux measurement, the separator was tested for 120 hours at DOE test 1 conditions followed by an additional 120 hours in the presence of H_2S (test condition 2a). Between conditions, rapid, pure hydrogen flux measurements were taken to ensure the membrane was not undergoing degradation and some nitrogen leak checks were also performed to verify leak tight performance as indicated on Figure 36. After testing at test 2a conditions, the separator was briefly returned to test 1 conditions to further establish that the membrane maintained performance after exposure to sulfur. Subsequently, the membrane was retested under test condition 2a for an additional 120 hours followed by a final durability test under test 2b conditions.

During the first half of the testing under DOE test conditions 1 and 2a, the separator was not run isothermally, which is reflected in the differences shown in Figure 36 between the membrane control temperature and the mean of the separator skin temperatures. After the test 2a condition was finished, the separator testing was shut down to adjust the heater configuration and make the remainder of the testing isothermal. Since the performance in the presence of sulfur is sensitive to temperature, the first test under condition 2a was not representative of the isothermal membrane performance as part of the separator was cooler than the desired 450 °C operating condition. The measured hydrogen flux of 7.4±0.6 $ft^3ft^{-2}h^{-1}$

for the non-isothermal DOE test 2a result improved to 10.7±1.1 $ft^3ft^{-2}h^{-1}$ after the heating profile of the separator was corrected.

As shown in the data summary in Table 10, the membrane experienced a decrease in hydrogen flux with a corresponding reduction in hydrogen recovery as sulfur and other non-hydrogen species were increased and the feed hydrogen concentration was decreased. During sulfur testing, there was an observed period of flux decay toward steady state that lasted as long as 30 hours for the first exposure to sulfur. This flux decay was attributed to sulfur adsorption and then saturation of the stainless steel components within the separator. Later exposure to sulfur after a pure hydrogen exposure showed reduced times to reach the steady-state flux which indicated that the stainless steel surfaces were more fully sulfided.

The data in Figure 36 show that the FCC PdCu alloy can operate in the presence of sulfur and that the reduction in hydrogen flux is reversible when the membrane is re-exposed to pure hydrogen. In addition, the membrane appears to be stable over the duration period of the test and no leaks were detected, confirming that the current tubes can withstand an operating pressure of 200 psia.

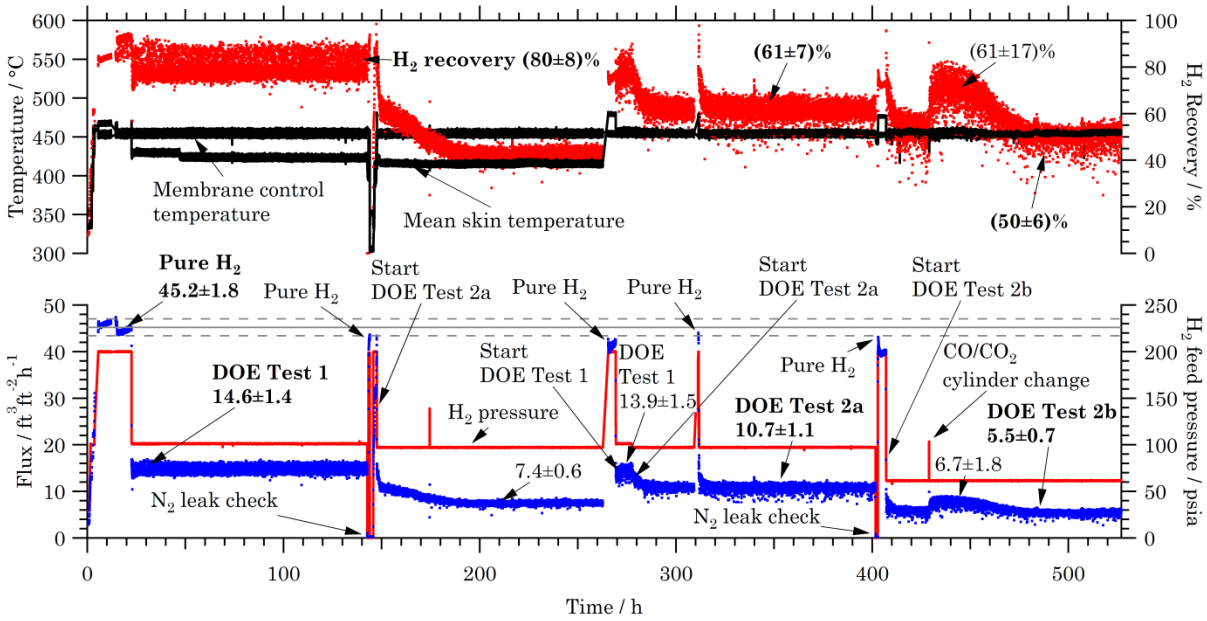

Figure 36: DOE protocol test data for FCC PdCu separator 5127. The membrane was tested for 527 hours at DOE protocol test conditions 1, 2a, & 2b at 450 °C.

Table 10: Summary of DOE testing protocol durability testing data for P+E separator 5127 at 450 °C. Errors for measured hydrogen flux and recovery are given in terms of 95% confidence levels.

Test condition	Hydrogen flux / $ft^3ft^{-2}h^{-1}$	Hydrogen recovery / %
Pure H_2	45.2±1.8	>80
Test 1	14.6±1.4	80±8
Test 1 repeat	13.9±1.5	
Test 2a	10.7±1.1	61±7
Test 2b	5.5±0.7	50±6

2.1.4.6 Enhanced FCC PdCu Alloy

The data in Figure 25 for the mechanically polished ternary alloy separator did not achieve the hydrogen permeability and flux desired by the DOE. As a result, for the remaining separators to be fabricated for the project, it was decided to evaluate the performance of a new PdCu membrane from P+E. The data for the new membrane, which is based on the FCC PdCu and "enhanced" through a proprietary P+E process are also shown in Figure 25 and appeared to have the same permeability of the McKinley BCC PdCu data. One critical difference was that the membrane did not go through a phase transformation at temperatures above 450 °C.

Figure 37 shows a hydrogen flux comparison between the enhanced PdCu alloy and a previously tested standard PdCu. For any given temperature, there was an approximately five to six fold improvement in hydrogen flux for the enhanced PdCu relative to the standard FCC PdCu membranes. The highest flux observed for the project, 125 $ft^3ft^{-2}h^{-1}$, was obtained on a single tube separator with a hydrogen feed pressure of 185 psig at 500 °C.

Several single-tube separators were tested at both P+E and UTRC toward the end of the project. Figure 38 shows the hydrogen permeability of several single tube membrane tests with the enhanced PdCu measured with pure hydrogen at different feed pressures up to 185 psig. In general, the permeability of this membrane was $(1–2)\times10^{-8}$ $mol.s^{-1}.m^{-1}.Pa^{-0.5}$.

One single tube separator was tested with a variety of different gas mixtures to elucidate the impact of different gas species on the PdCu as was reported for previous separators. Unlike previous tests, these experiments were performed under flow conditions such that the hydrogen recovery of the separator was 10% or less to better simulate "differential" conditions and simplify direct calculation of the permeability. Due to time constraints associated with the end of the contract, it was not possible to complete the entire set of experiments, although there was a ten hour period at the end of the tests where the separator was tested under DOE protocol test conditions 1 and 2A (Driscoll et al., 2008) for five hours each without any change in performance. This suggests that the enhanced PdCu membranes retain the sulfur resistance of the standard FCC PdCu, but with increased permeability.

Parameter estimation was performed to determine the coefficients that would describe the effect of different gas species on the hydrogen permeability. Figure 39 shows the parity plot of the predicted permeabilities versus observed permeabilities for the multi-gas testing. For the data that was available, there was a statistically significant impact due to the presence of different partial pressures of carbon monoxide, whereas other gas species; such as nitrogen, carbon dioxide, and water; appeared to have a negligible effect on hydrogen permeability. The resulting fitted permeability model is shown below, where the permeability (Q) is given in units of $mol.s^{-1}.m^{-1}.Pa^{-0.5}$, the temperature is in Kelvin, and the partial pressure of carbon monoxide is in Pascals. The model prediction for pure hydrogen is also shown graphically in Figure 38, showing further good agreement with the data.

$$Q = \frac{Q_{H_2}}{1 + K_{CO}P_{CO}} = \frac{e^{(-18.275+2.1014(1-673.15/T(K))}}{(1 + e^{(-14.216-5.5942(673.15/T(K)-1))}P_{CO}(Pa))}$$

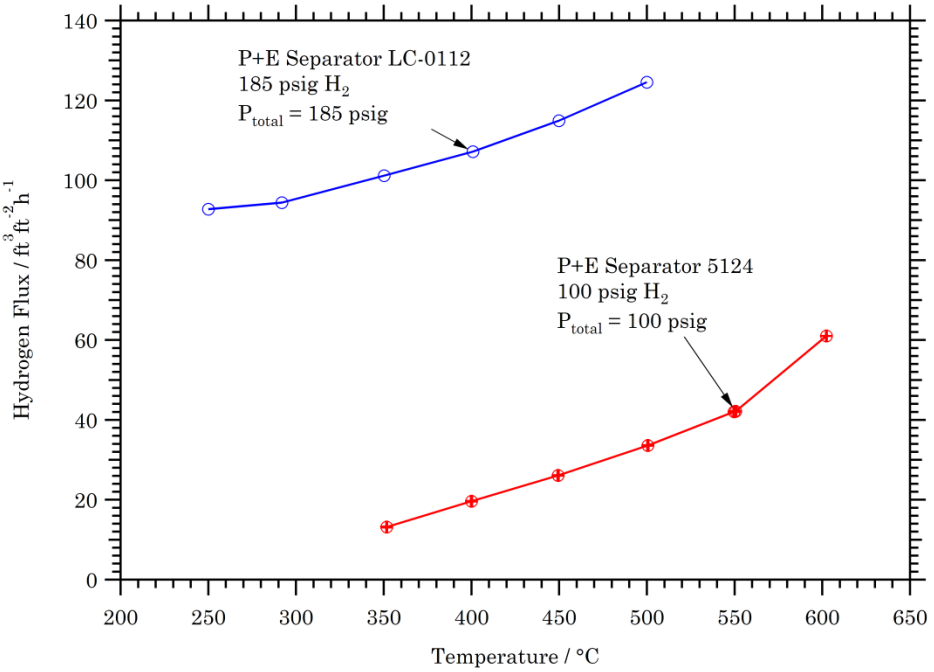

Figure 37: Hydrogen flux comparison of the enhanced PdCu membrane (LC-0112) to the standard FCC PdCu alloy (P+E 5124) previously reported. There is a factor of 5–6 improvement in hydrogen flux for the enhanced PdCu membrane.

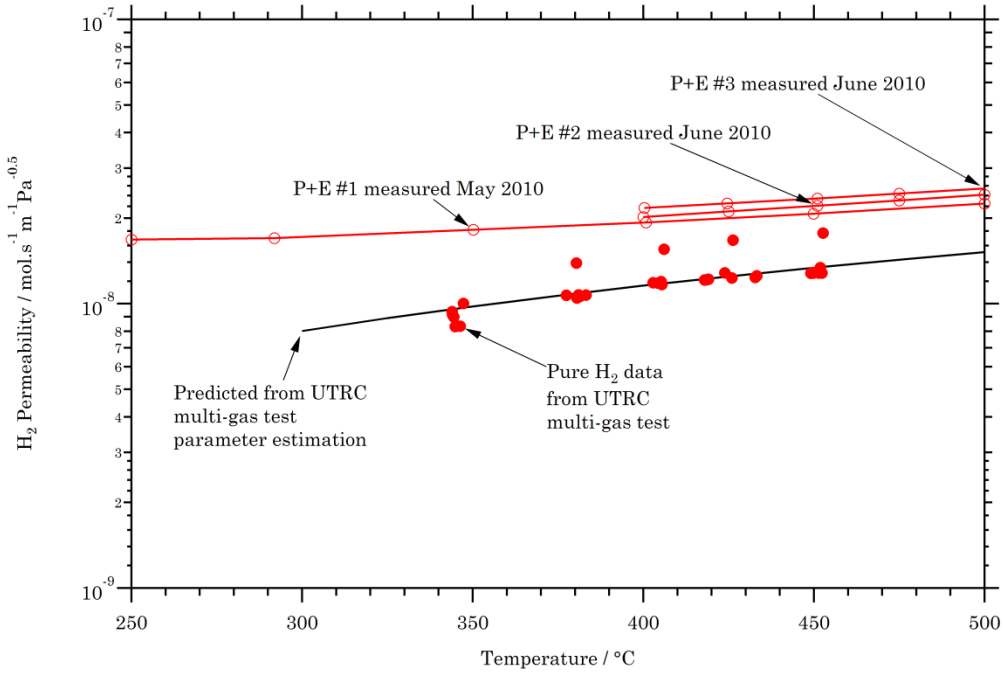

Figure 38: Pure hydrogen permeability measurements as a function of temperature for three enhanced PdCu single tube separators and one separator evaluated at UTRC. Also shown is the predicted hydrogen permeability obtained from parameter estimation using different gas mixtures.

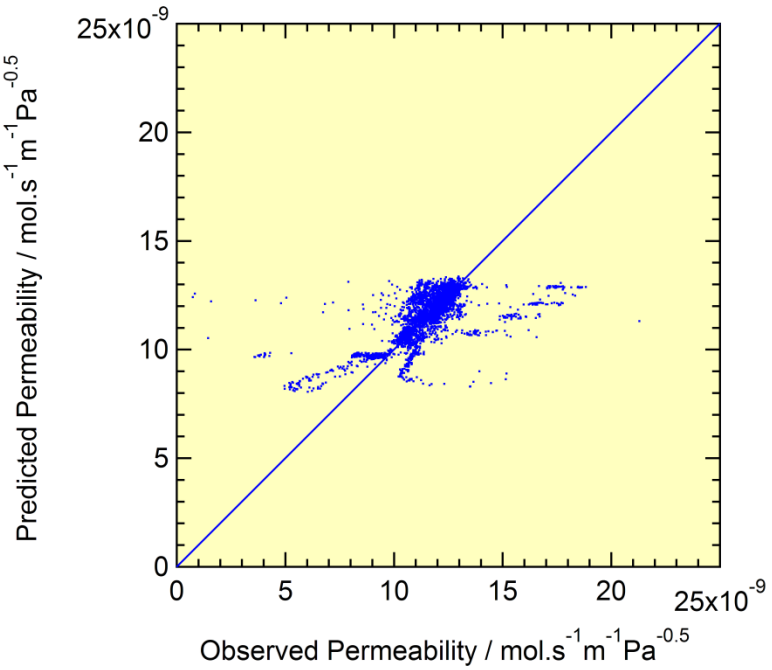

Figure 39: Parity plot for the predicted hydrogen permeability obtained from parameter estimation using different gas mixtures versus the observed data for a single tube separator.

2.2 Pd-alloy/Nanoporous Oxide Membrane Development

The Pd-alloy nanoporous oxide membrane concept was an alternate path to the dense metallic concept. It was based on the deposition of Pd alloy within the pores of a nanoporous oxide matrix supported on a porous metal tube (see Figure 40). The porous metal tube provides the membrane strength and the ability to operate at elevated pressures. The sulfur-resistant Pd alloy plugs block the pores of the ceramic layer providing H_2 separation with high flux. Ideally, the Pd alloy plugs should be very thin (<200 nm) to ensure that the membrane flux is no longer dominated by Sievert's Law. In addition, lower costs are possible with this concept due to the small amounts of noble metals used.

The work focused on the formation of pure Pd and Pd/Au alloy plugs inside the pores of nanoporous YSZ coated metal porous tubes provided by Pall Corporation. Various methods were evaluated to achieve incorporation of the metal into the pores including:

- Infiltration of correctly-sized colloidal metal particles into the pores,
- Precipitating of metal within the pores using counter diffusion of metal salt solutions and reductant,
- Infiltration of metal salt into the pores followed by calcination/reduction.

The project also included the development of synthesis techniques for the preparation of Pd and Pd/Au colloidal solutions.

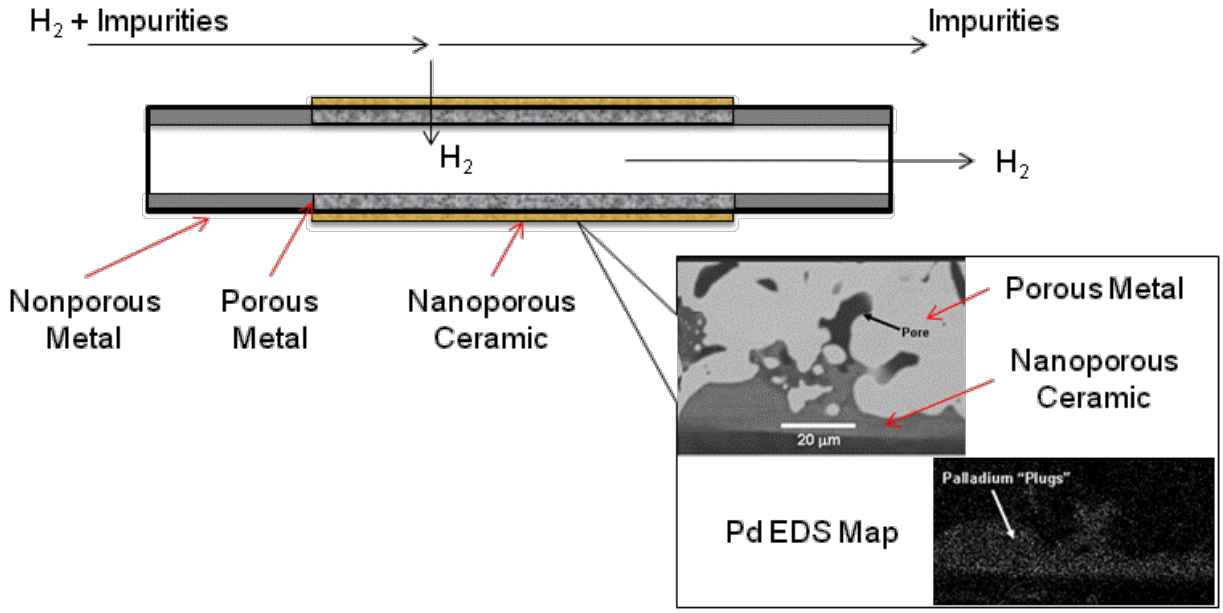

Figure 40: Nanocomposite membrane conceptual schematic.

2.2.1 Colloid Synthesis

The first step in colloid synthesis was to investigate the best route toward forming PdAu colloids since PdAu colloids are known to be resistant to sulfur (McKinley, 1967), an important property for hydrogen separation membranes for coal gas applications. In addition, PdAu was chosen over PdCu because the preparation method was more straightforward.

The main approach investigated for the PdAu colloid was based on the use of a stable, gold colloid as precursor seeds followed by addition of Pd to the gold particles. A proprietary internal method was used to produce the gold colloids, but commercially available gold colloids were also investigated. The gold colloids produced at UTRC had a smaller particle size distribution than the commercially available products, as shown on the TEM and particle size distribution plots presented in Figure 41. The particle size distribution for the gold colloids synthesized at UTRC was ≈14 nm, about half that of the commercial gold colloid.

Based on the previous Union Carbide work (McKinley, 1967), PdAu alloys with a composition between 5% by weight gold and 40% by weight gold should produce sulfur tolerant hydrogen permeable membranes. The initial target for the PdAu colloid was 5% by weight. Figure 42 shows the TEM images and particle size distribution for a 95wt%Pd/5%wtAu colloid produced by adding the Pd to the gold colloid shown in Figure 41. The resulting colloid had a mean particle size of 55 nm, with only a small fraction of the particles greater than 75 nm. Since the mean pore size of the oxide membrane was approximately 70 nm, it was desirable to have a colloid with only a few very small particles, which may pass through the oxide during preparation, and only a few very large particles which may not be able to penetrate the oxide.

A range of PdAu colloids were produced using the UTRC synthesized Au seeds to determine the effect of Au composition on the final particle size of the PdAu colloid suspension. The results of the particle size measurements from TEM (summarized in

Figure 43) indicated that the colloid size decreased as the wt% of Au was increased. This was not a surprising result, since adding the same amount of Pd to a larger number of Au seeds should result in smaller particles. However, the decreasing trend in particle size was shown to level off once the Au composition was greater than about 30 wt%.

Au colloids and PdAu colloids were examined via electron diffraction in TEM and shown to have d-spacings consistent with Au and Pd. Figure 44 shows a typical bright field image, diffraction pattern and measured d-spacings from a pure Au colloid which was consistent with Au and Figure 45 shows a typical bright field image, diffraction pattern and measured d-spacings from a 20 wt% Au/80 wt% Pd colloid. The TEM picture also shows that the PdAu colloid particles were faceted, which was not observed in the Au seeds.

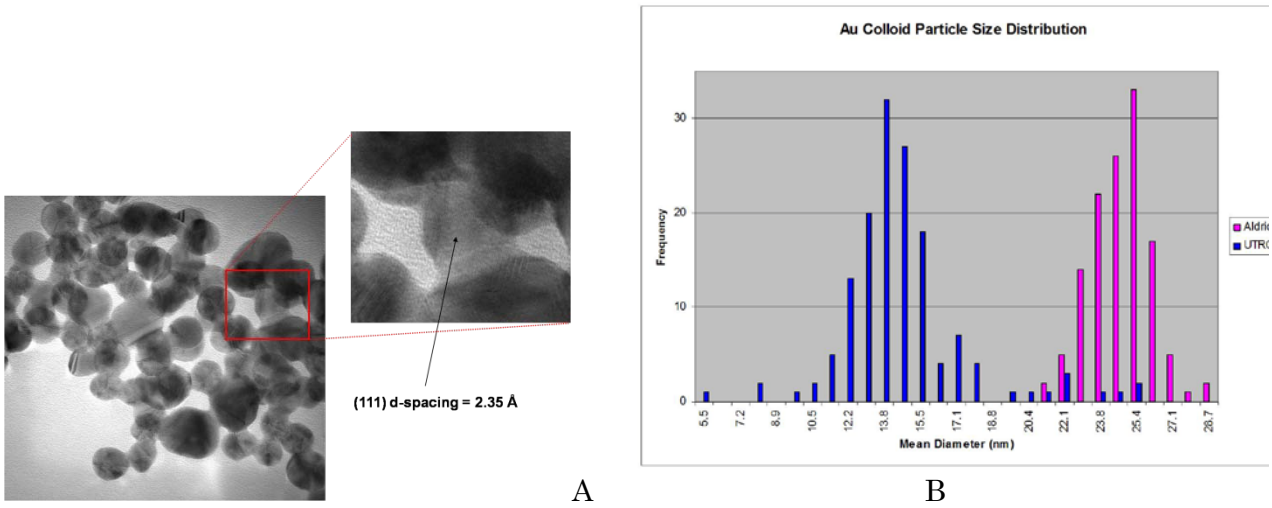

A B

Figure 41: Initial gold colloid synthesized at UTRC. Image A on left was taken in a TEM, with the high resolution image at a magnification of 580,000×. Plot B on the right shows the gold particle size distribution, for the commercial (Aldrich) and UTRC synthesized gold colloids, based on TEM measurements.

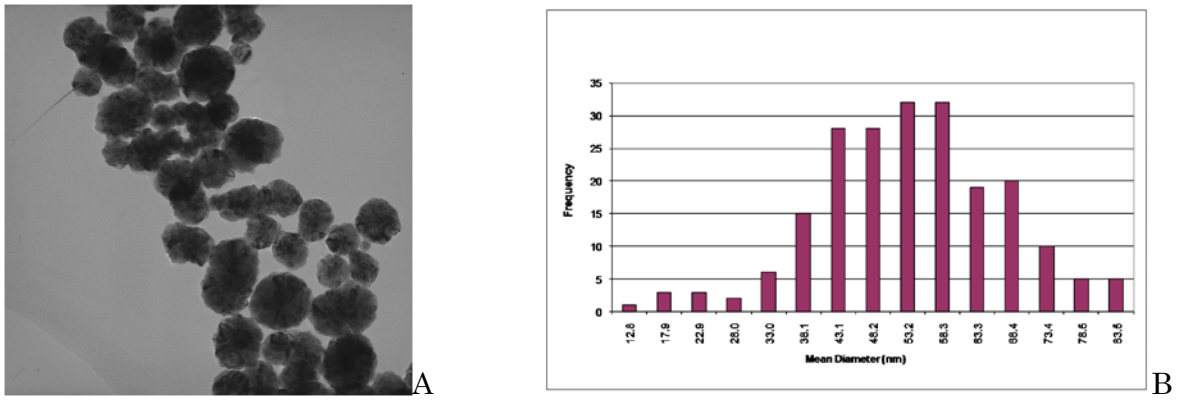

A B

Figure 42: 95wt%Pd/5wt%Au colloid produced by addition of palladium to UTRC gold colloid seeds. Image A on the left was taken in a TEM at a magnification of 135,000×. Plot B on the right shows the particle size distribution, centered at approximately 55 nm.

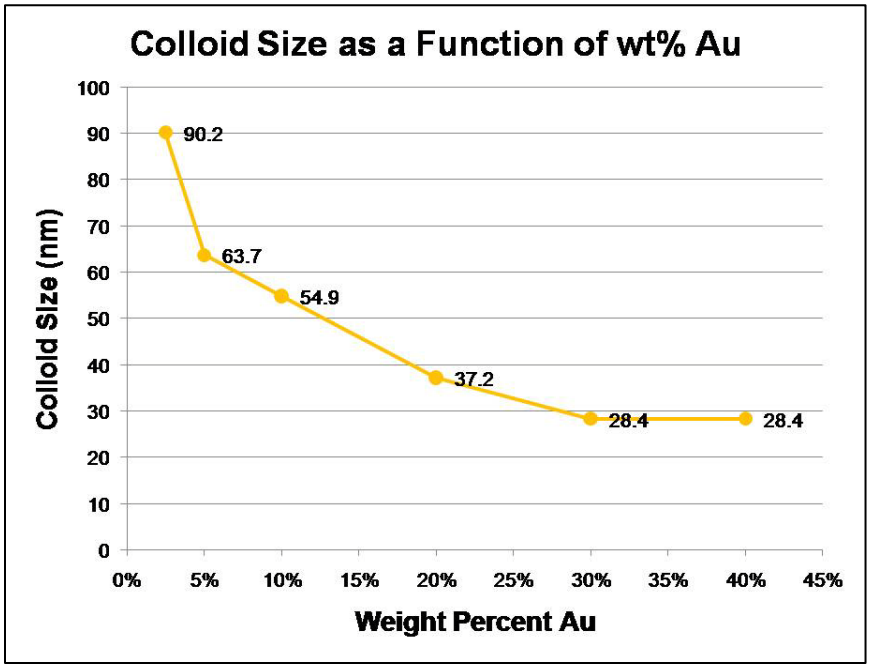

Figure 43: Average colloid particle size as a function of wt% Au. Measurements were taken using TEM.

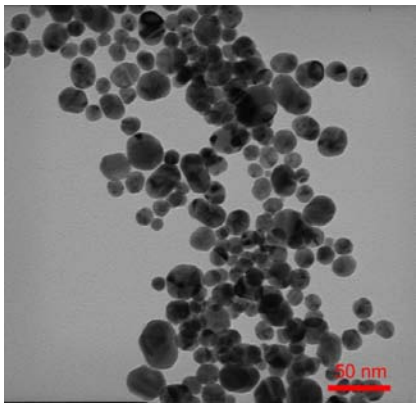

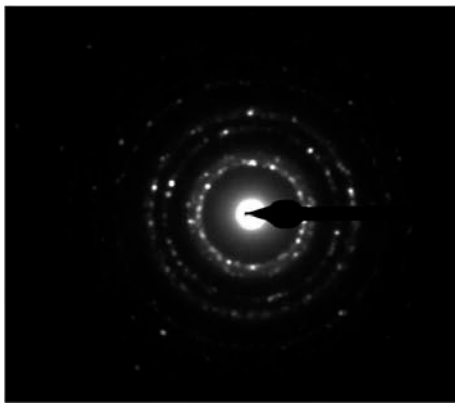

Plane	d (known)	d (avg. measured)
(111)	2.3546 Å	2.365 Å
(200)	2.0391 Å	2.049 Å
(220)	1.4419 Å	1.465 Å
(311)	1.2296 Å	1.226 Å

Figure 44: A bright field TEM image and corresponding diffraction pattern of Au seeds. The diffraction pattern was consistent with the d-spacings for pure Au as shown in the table.

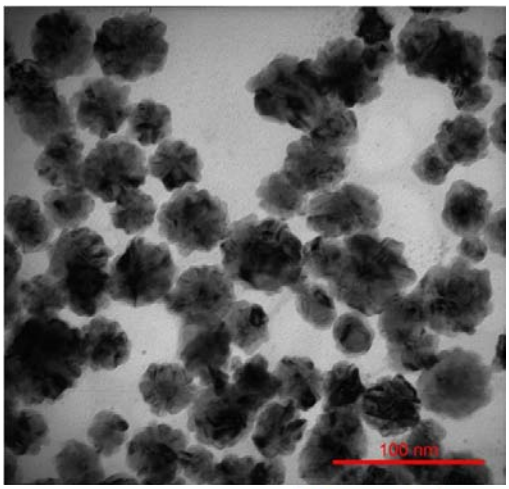

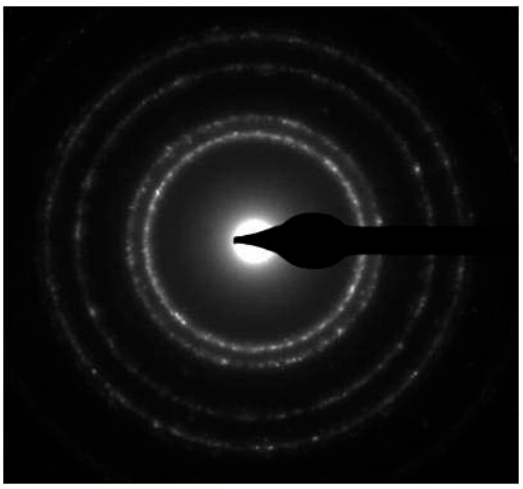

Measured d-spacing (Å)	Au (Å)	Pd (Å)	Plane
2.27	2.35	2.25	111
1.96	2.04	1.95	200
1.38	1.44	1.38	220
1.18	1.23	1.17	311

Figure 45: A bright field TEM image and corresponding diffraction pattern of an 80 wt% Pd/20 wt% Au colloid. Note from the table that the d-spacings measured from the diffraction pattern were consistent with Pd.

2.2.2 Porous Tube Characterization

The YSZ coated porous stainless steel tubes used in the study were a standard product manufactured by Pall Corporation (Figure 46). Upon receipt, each tube was visually inspected and pictures were taken. Each tube was cleaned by immersion in hot water (80 °C) overnight.

The nitrogen permeance and bubble point of each tube were measured using the set ups shown in Figure 47. The initial N_2 permeation was measured to provide a baseline and to assess the gas transport resistance through the porous substrate against the DOE's H_2 permeation target. The average tube permeance was 22.1±2.5 $ft^3ft^{-2}h^{-1}.psi^{-1}$ which translates into a N_2 flux of about 2200 $ft^3ft^{-2}h^{-1}$ at a 100 psia feed pressure. Since the H_2 permeation flux should be larger than that of nitrogen through a porous substrate with meso and micro pores, one can expect that, at the DOE's H_2 flux target of 200 $ft^3ft^{-2}h^{-1}$, the resistance through the porous part of the membrane will be negligible compared to that of a Pd or Pd alloy layer.

Figure 46: YSZ coated porous stainless steel tube manufactured by Pall Corporation.

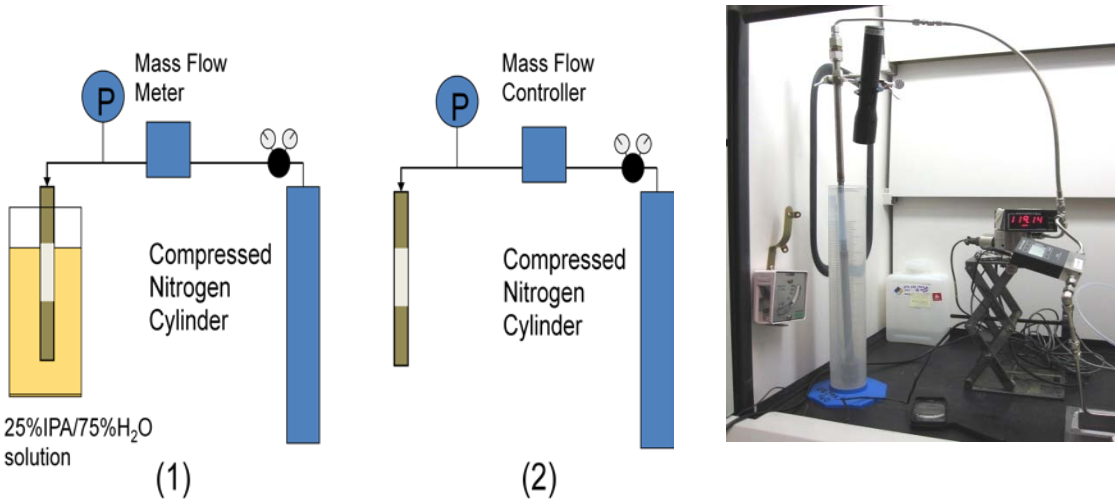

Figure 47: Flow schematic for bubble point measurement (1) and nitrogen permeance measurement (2). Picture of bubble point measurement set up.

2.2.3 Pd-alloy/Nanoporous Oxide Membrane Synthesis

2.2.3.1 Direct Colloidal Solution Infiltration Method

2.2.3.1.1 First Attempt using PdAu Colloid–Full Tube

The first attempt at immobilizing colloids inside the oxide YSZ layer pores was carried out using PdAu colloids of 30-40 nm size. The objective of the process was to plug the pores of the substrate with PdAu colloids to obtain a gas-tight PdAu colloid membrane. The colloidal solution was pushed through the membrane walls from the stainless steel side to the oxide side using pressure (>100 psig). The permeate was a clear solution indicating retention of the metal within the membrane. Four loading steps were implemented. After each loading step, the membrane tube was dried and its N_2 permeance was measured at room temperature to evaluate whether a gas tight membrane was achieved.

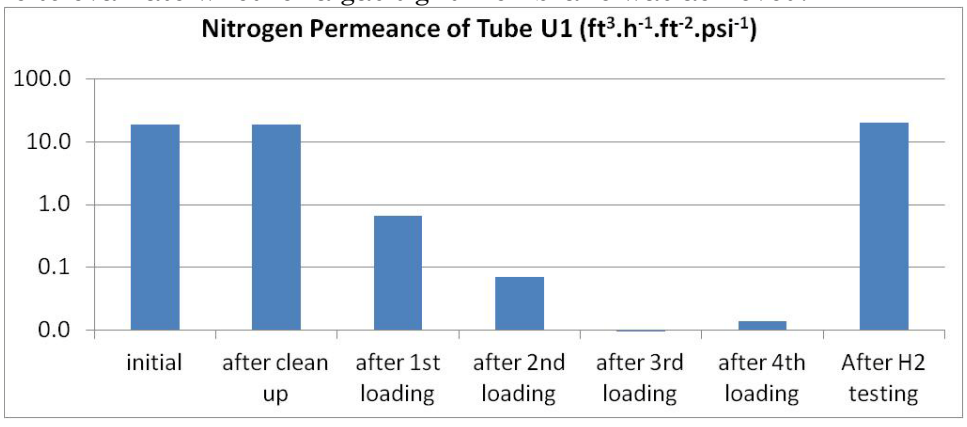

Figure 48: N_2 permeance data for first colloidal membrane synthesis. The permeability was measured after each loading of PdAu colloid, showing a decrease in flux as the pores in the oxide layer were blocked. Also shown is the data taken after testing the membrane

As shown in Figure 48, the N_2 permeance decreased significantly after each colloid loading, indicating that the pores were plugged with the PdAu colloids. After the fourth loading, the N_2 flux had decreased by 99.9% compared to the initial N_2 flux and the membrane was heated up under H_2 pressure to measure the H_2 permeance (Figure 49). The N_2 permeation flux was initially not measureable at a pressure of about 30 psia and a temperature of about 350 °C. The H_2 flux jumped to a promising 200 $ft^3ft^{-2}h^{-1}$ at 365 °C and 30 psia in a short time (around 3 hours) from 12 $ft^3ft^{-2}h^{-1}$ at about 300 °C and the same pressure. However, when the H_2 feed was switched to N_2 gas, the N_2 permeation flux was about 120 $ft^3ft^{-2}h^{-1}$ at 350 °C and 20 psia. This high N_2 flux combined with elemental characterization indicated that the PdAu colloids which plugged the pores were blown away during the H_2 permeation testing.

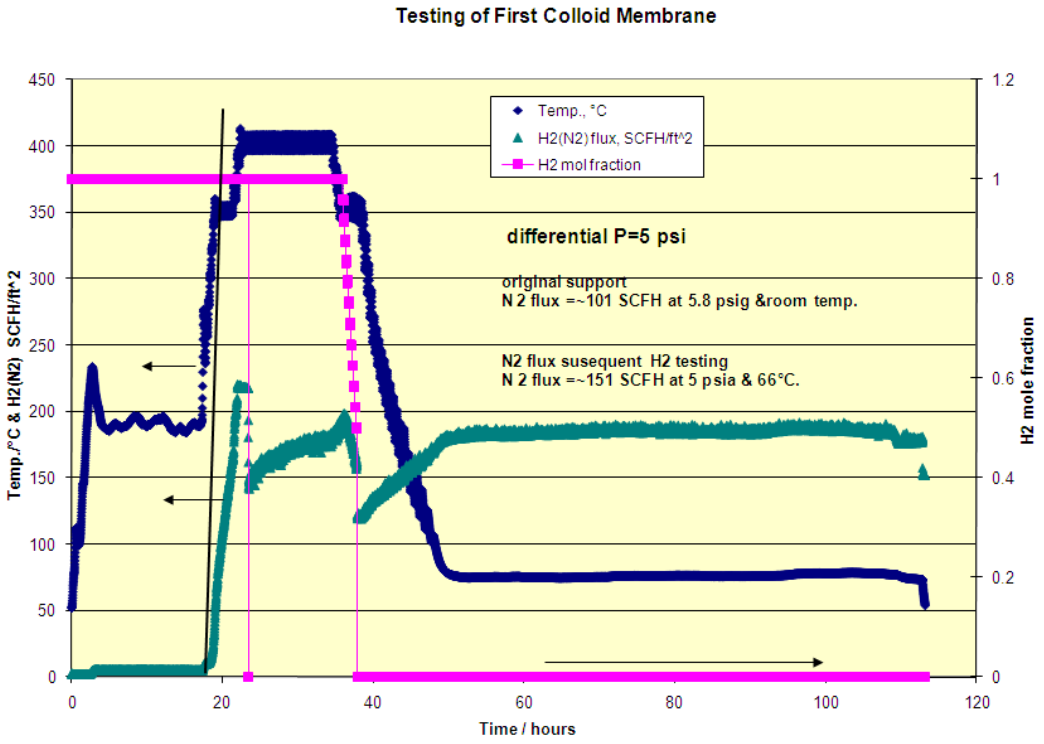

Figure 49: Hydrogen testing of first attempt at making a PdAu colloidal membrane.

2.2.3.1.2 Colloid Infiltration: Coupon Testing–Vacuum Method–YSZ to Stainless Steel Side

After the failure of the first attempt and due to a temporary limited availability of supports, various trials were carried out on membrane coupons using vacuum as a driving force for colloid infiltration (Figure 50). Various variables were investigated such as:

- Size and composition of colloidal solution
- pH of colloidal solution
- Pre-treatment of the surface
- Infiltration method (vacuum, pressure)
- Addition of polyvinylalcohol to increase stability of the colloidal solution

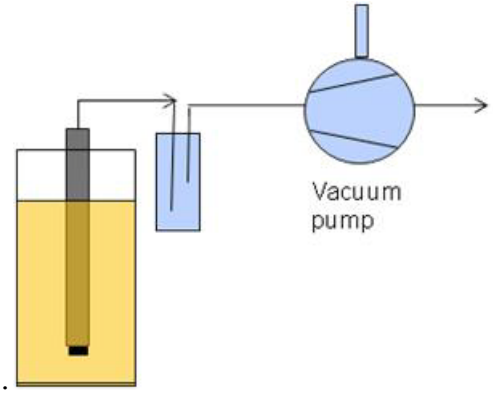

Figure 50: Experimental schematic for coupon testing using vacuum.

Figure 51 shows a YSZ-coated stainless steel tube obtained by vacuuming the smallest available colloid solution (20 ppm Au, 3 nm) from the zirconia to the stainless steel side. As apparent in the Figure, the gold colloid was deposited on the outside of the YSZ layer rather than infiltrating it. When the pH of the gold colloid solution was modified either by adding ammonium hydroxide or nitric acid (in an attempt to change the interaction between the YSZ and the colloid solution), the appearance of the coated coupons did change but no significant internal deposition was observed by SEM (Figure 52). Since all the attempts made were unsuccessful at demonstrating the presence of metal within the YSZ layer, it was decided to modify the process to vacuum the colloidal solution from the stainless steel side to the YSZ side.

2.2.3.1.3 Colloid Infiltration: Vacuum Method – Stainless Steel to YSZ Side

Various colloidal solutions were passed through the stainless steel portion of the YSZ tube (i.e., before the coating process) and it was noted that only solutions made of very small colloids (10 nm and less) were able to pass through the porous stainless steel. Therefore, a Pd colloidal solution synthesized by PurestColloid (concentration 10 ppm Pd, colloid size 10 nm) was used to infiltrate a YSZ-coated porous tube using vacuum. The solution was introduced into the inside of the tube (stainless steel side) and vacuum was applied on the outside. The liquid permeating the membrane and recovered on the outside of the YSZ layer was clear, indicating that the colloid was retained within the YSZ layer.

The N_2 permeance of the tube was measured several times after given volumes of colloidal solution were passed through the membrane. A preliminary calculation indicated that given the YSZ layer morphology (i.e., porosity and pore size), and assuming that all the colloidal particles were retained in the YSZ layer, about 10 L of Pd colloidal solution would be required to create the desired Pd plugs.

Figure 53 shows that after 16 L of colloid solution were passed through the membrane, the N_2 permeance had only decreased by about half. Given that the N_2 permeance decrease showed an asymptotic trend and the length of the process, it was decided that this immobilization technique was not a viable technique and the testing was terminated.

Figure 51: YSZ-coated porous stainless steel tube after vacuuming of a 3 nm gold colloidal solution. Metal appears to have coated rather than infiltrated the YSZ layer.

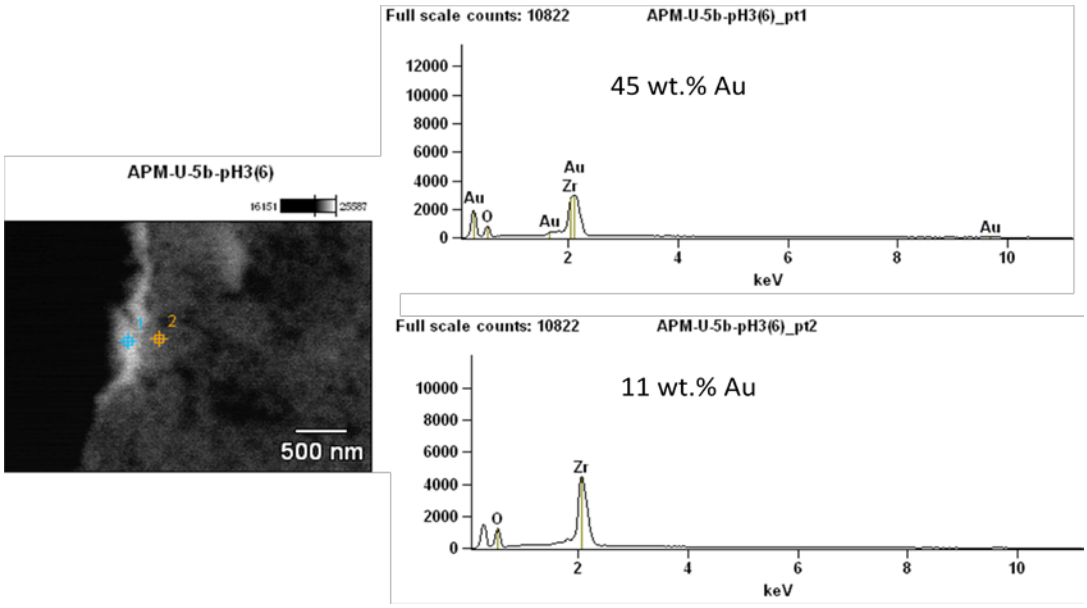

Figure 52: SEM picture and EDS line scan of a YSZ-coated stainless steel tube after vacuuming a 3 nm colloid solution of pH = 3.

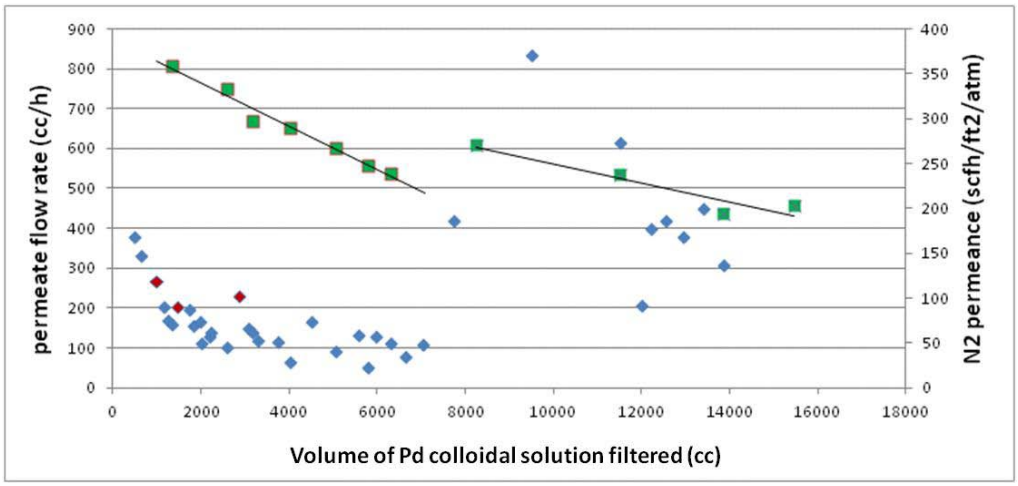

Figure 53: Infiltration of 10 nm Pd colloidal solution through a YSZ coated porous tube using vacuum (stainless steel to YSZ side). The square markers indicate the N_2 permeance, whereas the diamond markers indicate permeate flow.

2.2.3.1.4 Colloidal Infiltration: Infiltration with Seeding

Since previous attempts to infiltrate a Pd or Pd/Au colloidal into the ceramic YSZ layer of the membrane based on size exclusion principles alone had been unsuccessful and mostly led to the metal depositing on the external surface of the YSZ coating, or internally at the interface between the YSZ coating and the stainless steel, the next attempt was to try and increase the affinity of the Pd or Pd/Au colloid to deposit selectively within the YSZ coating layer. To do so, a process step was applied ahead of the colloid infiltration step in which alternating solutions of palladium and tin chloride solutions were flowed through the YSZ layer to effectively "seed" the ceramic. It is well established that palladium has a high affinity to deposit onto a previous, reduced palladium surface. This method has been successfully applied for the electroless deposition of palladium onto stainless steel membranes. Palladium chloride is instantly reduced to palladium metal when placed in contact with tin chloride (see equation below).

$$PdCl_2\ (aq) + SnCl_2\ (aq) \rightarrow Pd + SnCl_4\ (aq)$$

In addition to including a "seeding" step to the process, the overall procedure for infiltrating the Pd or Pd/Au colloid solution through the membrane, and therefore through the YSZ layer, was also modified. In all previous experiments, the colloid solution was either "pushed' through the membrane using pressure or vacuumed through. Since these methods may caused destabilization of the colloidal solution, it was decided to only use diffusion for colloid infiltration.

In total, five $PdCl_2/SnCl_2$ "seeding" cycles were applied to a membrane (tube 164), before contact with the colloid solution. Figure 54 shows the nitrogen permeance values after cycles #2 and #5. ICP analysis on the $PdCl_2/SnCl_2$ solutions after they were passed through the membrane (from outside to inside using vacuum suction) suggested that ≈90% of the palladium was retained inside the membrane. Originally, this membrane tube was characterized as having a nitrogen permeance of 20 $ft^3ft^{-2}h^{-1}.psi^{-1}$. After two $PdCl_2/SnCl_2$ "seeding" cycles, the nitrogen permeance dropped to 4.7 $ft^3ft^{-2}h^{-1}.psi^{-1}$and after 5 cycles was 2.4 $ft^3ft^{-2}h^{-1}.psi^{-1}$. After washing and calcination, the nitrogen permeance increased to 4.2 $ft^3ft^{-2}h^{-1}.psi^{-1}$. suggesting that the membrane was only ≈57% leak tight.

Since the goal was not to make the membrane leak tight using just the seeding cycles, it was decided to place the membrane in contact with the colloidal solution. The colloidal solution selected for this study had the composition 95% Pd / 5% Au and a measured hydrodynamic body, or agglomerate/cluster size, of 75 nm, which is within the range of the pore size distribution measured for the YSZ layer. The full size membrane was placed in contact with the Pd/Au colloid solution for several hours, after which the solution was replaced with fresh colloid solution. This step was repeated 9 times. The membrane was then dried and finally reduced under hydrogen. After drying, the nitrogen permeance was 2.8 $ft^3ft^{-2}h^{-1}.psi^{-1}$. After hydrogen reduction, it was 8.6 $ft^3ft^{-2}h^{-1}.psi^{-1}$. At this point, the membrane was considered to have potential defects and a bubble point test was performed.

The membrane was found to be leaking profusely from the seal area, as shown in Figure 55. Bubbles were visible as low as 7 psig, suggesting micron size defects. These large defects were most likely due to the hydrogen reduction step which was performed at 500 °C. It was also possible that prolonged exposure to the acidic Pd/Au colloid solutions could have weakened the seal.

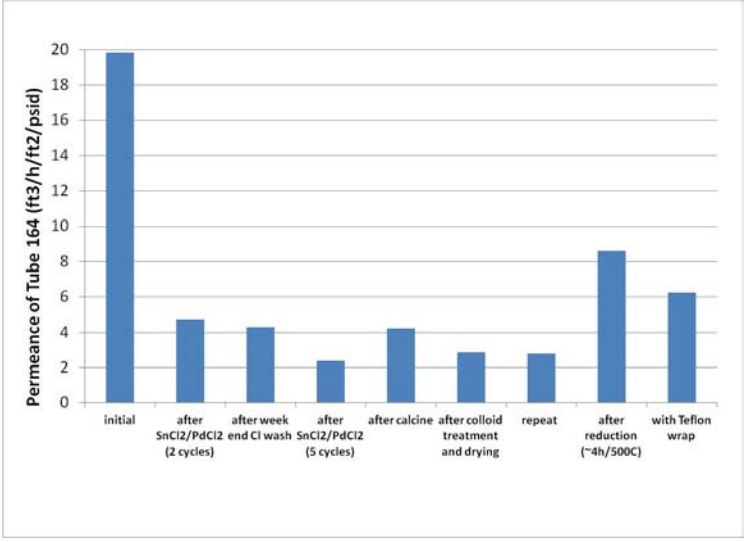

Figure 54: Nitrogen permeance of tube 164 at various treatment steps. A 68% reduction in N2 permeance was obtained.

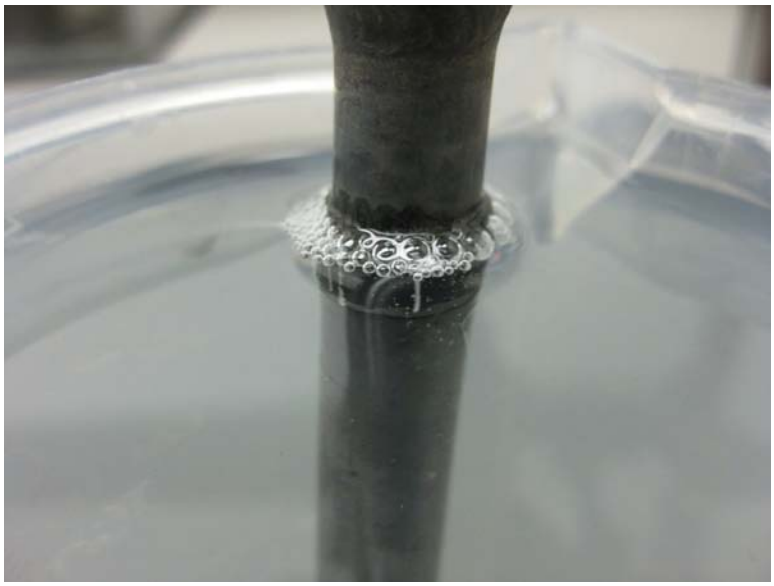

Figure 55: Photo taken from the bubble point test performed on tube 164 after the final hydrogen reduction step.

The membrane tube was cross-sectioned and mounted for SEM analysis to determine the location of the Pd seeds and also the Pd/Au colloid metal. The SEM cross-section images are shown in Figure 56. Very little gold was detected, suggesting that most of the metal entrapment occurred during the seeding cycles. Also, the majority of the metal entrapped (Pd) was located at the YSZ/stainless steel interface and not throughout the YSZ layer.

Since the colloid infiltration method did not give satisfactory results despite numerous attempts, another method based on in situ deposition/precipitation of the metal inside the pores was considered.

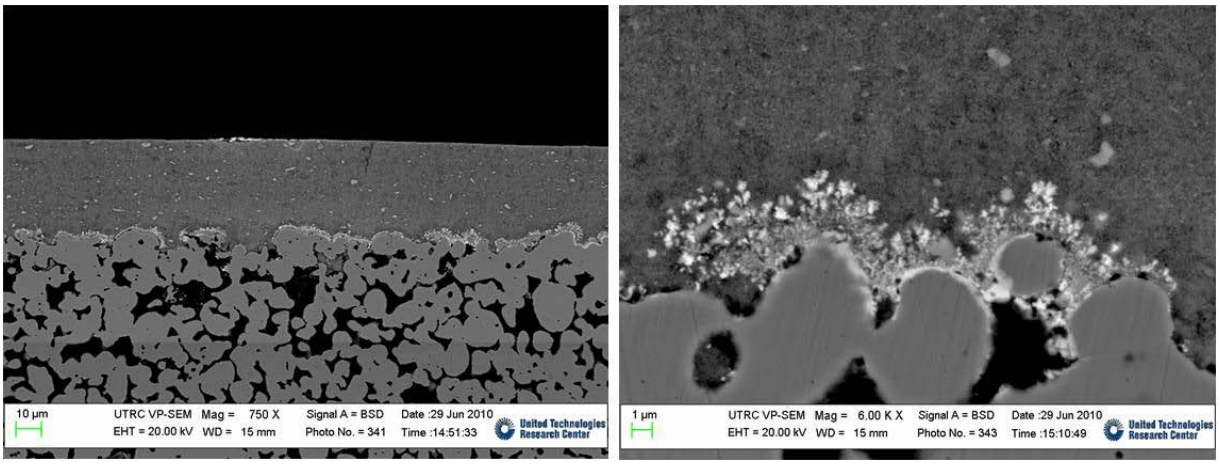

Figure 56: SEM pictures of tube 164 showing the presence of metal at the stainless steel/YSZ interface and at the outside surface.

2.2.3.2 In situ Deposition/Precipitation Method

In the deposition/precipitation (DP) technique, illustrated in Figure 57, the YSZ side of the membrane was contacted with a salt solution of chloroauric acid and palladium chloride and the stainless steel side was contacted with a reductant solution of L-ascorbic acid and sodium citrate. The deposition/precipitation technique relied on the counter-diffusion of the metal salt and reductant through the porous support. The contact of the two solutions within the membrane should cause precipitation of the gold and palladium metals.

Four 1-in long pieces of YSZ-coated tube were used to evaluate the possibility of depositing metal within the YSZ layer using DP. As shown in Table 11, sample 3-A was the baseline coupon. In sample 3-B, starch was added to the reductant solution to increase its viscosity and in sample 3-D, the reductant concentration was divided by two. The goal of both changes was to slow the diffusion of the reductant. Sample 3-C was a control sample where no reductant was added. The coupons are shown in Figure 58 during deposition (left image) and after deposition (right image). An EDS line scan was obtained for samples 3-B and 3-D (shown in Figure 59) which showed internal deposition of gold and palladium for both samples.

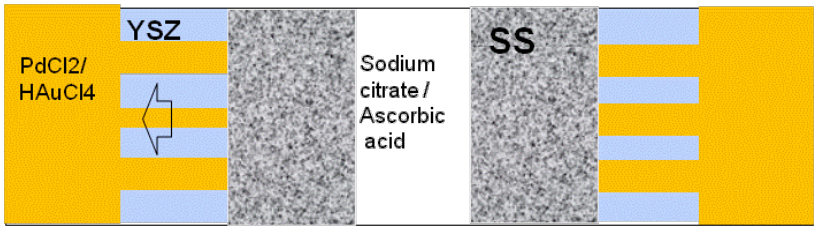

Figure 57: Schematic for the deposition/precipitation conceptual schematic.

Table 11: Description of deposition/precipitation coupon test conditions.

Tube #	Contacted Solutions	Results
3-A	1× metal – 1× reductant	YSZ surface becomes dark at ≈40 min
3-B	1× metal – 1× reductant + starch	Slower darkening of surface
3-C	Control	No change
3-D	1× metal – ×/2 reductant	Slowest darkening of surface

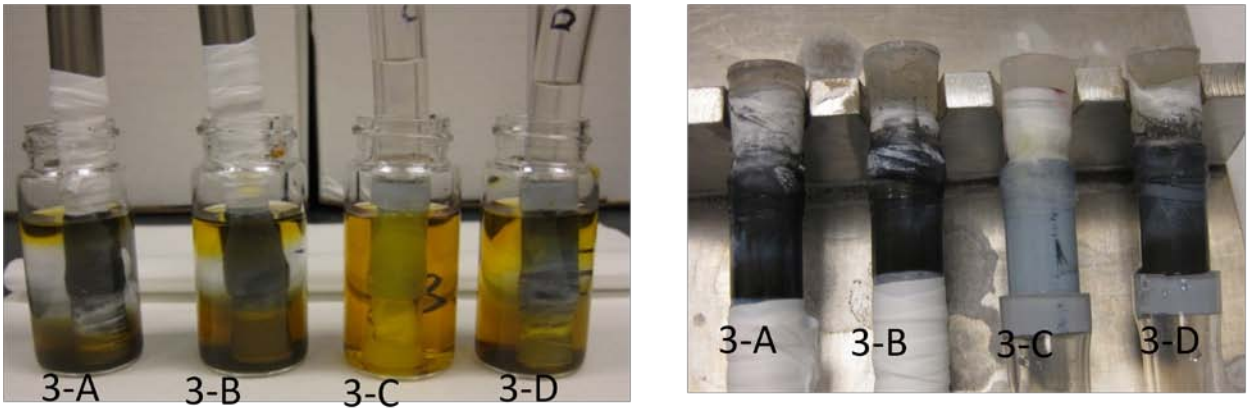

Figure 58: Test coupons before (left) and after (right) deposition/precipitation.

Even though the deposition/precipitation technique proved promising at the coupon level, it was found that when the method was transitioned to full tubes, the metal preferentially accumulated either at the surface of the YSZ layer or at the stainless steel/YSZ interface (Figure 60) and it proved challenging to control the position of the deposited layer within the membrane, probably due to the wide pore size distribution. In addition, the presence of preferential diffusion paths at the porous/non-porous stainless steel interface complicated the balancing of diffusion rates within the membrane matrix.

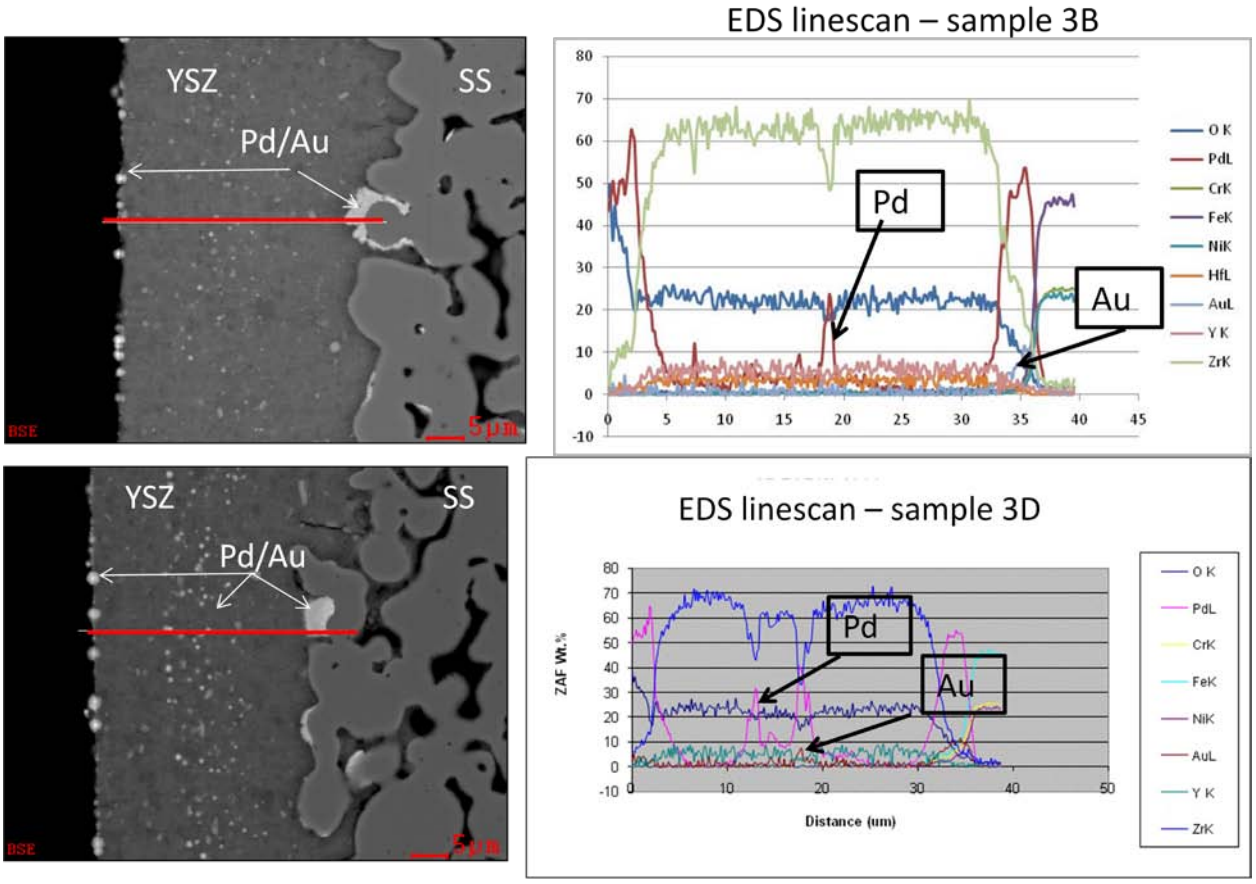

Figure 59: SEM and EDS line scan obtained for test coupon samples 3-B (top) and 3-D (bottom).

Figure 60: Surface deposition of metal using deposition/precipitation method.

2.2.3.3 Alternative Preparation Method

Based on the understanding developed through the other approaches (Sections 2.2.3.1 & 2.2.3.2), an alternative approach was developed to produce a viable Pd-alloy nanoporous oxide membrane. At various points during the synthesis of the final separator of the project, the nitrogen permeance was measured. The N_2 permeance decreased by 96% after five treatments, which was a promising result. However, time constraints prevented additional membrane processing for a hydrogen permeability measurement to be performed.

2.3 Pd Membrane Atomic Modeling

2.3.1 Adsorbate Reactivity Predictions

2.3.1.1 Membrane–Adsorbate Interactions

Atomic modeling was conducted *a priori* to sub-scale and high pressure pilot scale H separator performance tests to determine the influence of the $Pd_{0.47}Cu_{0.52}TM_{0.01}$ (TM= transition metal) membrane alloy composition and structure on H solubilization, susceptibility to poisons, and reactivity with C precursor species for coke formation, compared to the binary parent membrane alloy $Pd_{0.47}Cu_{0.53,}$ and in selected cases, with other common reactor construction metals, including Fe, Cr, Ni, Ti, and Zr. The predictions evaluated the interactions of strong binding reactants, like CO, or coal contaminant poisons, including H_2S, S, and Cl, which may compete with H adsorption and solubilization processes on the alloy/metal surfaces. The favorability of ligand interactions on inducing surface segregation of the PdCu B2 alloys was also taken into consideration.

Coke formation is a serious concern for the process intensification of centralized H_2 production from gasified coal, especially at effective low temperatures, increasing H/C, or decreasing O/C ratios for high efficiency H_2 conversion. Coke can deactivate H-selective membrane surfaces and block reactor volumes, dramatically shortening reactor runtime in between regeneration cycles. Under these conditions, the heterogeneously catalyzed Boudouard reaction, $*CO + CO \rightarrow *C + CO_2$, and/or reverse gasification reaction, $*CO + H_2 \rightarrow *C + H_2O$ (*=adsorbed), are major sources of surface and subsurface carbon that lead to coke formation. Atomic modeling simulations were made to simulate C adsorption, C subsurface absorption, and bulk solubilization, with respect to the Boudouard reaction. The turnover for heterogeneously catalyzed CO dissociation or disproportionation reactions increases with CO surface binding, which is proportional to the CO lifetime on the surface before desorption. Carbon formation is also influenced by increasing metal-carbon interactions, which drive saturation of the surface, solubilization into the subsurface and finally coke-precursor segregation or nucleation. Thus, the atomic predictions were interpreted to estimate tendencies for coke formation on the PdCu B2 membrane alloys in relation to other common reactor metals. This approach enabled the comparison of the CO and C coke precursor interactions with the B2 alloys to those of elements having known coke formation tendencies {Cr, Ni and Fe} and other possible alloying element {Ti, Zr} candidates for reducing coke formation.

2.3.1.2 Atomic Modeling Methodology

All calculations were made with the plane wave density function theory VASP code using projector augmented wave potentials to simulate periodic atomic structures. The models were relaxed to the most favorable geometries and energies at the ground state, using a force convergence criterion of 0.02 eV/Å. Full minimizations were made on bulk structures of atomic positions and lattice parameters, with the degrees of freedom determined by the model symmetry. Surface simulations were conducted on 4 layer slabs formed with the most favorable (lowest surface energy), closed-packed alloy or metal surfaces, which are the (110), (111), and (0001) surfaces for the $Im\bar{3}m$ (as well as the $Pm\bar{3}m$ PdCu-based B2 ordered alloys), $Fm\bar{3}m$, and $P6_3/mmc$ bulk phases, respectively. The slab atomic positions were relaxed, fixing the bottom layer atomic positions and the slab x-y dimensions to correspond

to the original minimized bulk structure. The slab surfaces were separated by a 10 Å vacuum layer. The pure metals were represented with 16 atom 4 layer slabs formed by revealing their most favorable surfaces. Four layer $Pd_{0.50}Cu_{0.50}$ 4x4 and $Pd_{0.50}Cu_{0.44}TM_{0.06}$ 2x2 32 atom (110) slab models were used to approximate the behavior of the experimental $Pd_{0.47}Cu_{0.53}$ and $Pd_{0.47}Cu_{0.52}TM_{0.01}$ B2 compositions, respectively. Previous simulations determined that in the latter composition, the ternary TM was more favorable substituted in subsurface layers than at the surface. This configuration was used in all $Pd_{0.50}Cu_{0.44}TM_{0.06}$ (110) surface simulations. The PdCu-based (110) surfaces reveal two types of 4-fold hemi-octahedral sites, formed from the lengthwise cleavage of the bulk α Pd_2Cu_4 and β Pd_4Cu_2 octahedra, which have underlying subsurface central Cu and Pd atoms, respectively. Adsorption and absorption calculations were made at a range of possible sites on the already relaxed surfaces, re-minimizing the atomic positions in the presence of the adsorbate. The adsorption or absorption enthalpies, ΔH_{ads} or ΔH_{abs}, were determined from the relationship

$$\Delta H_{ads} \text{ or } \Delta H_{abs} = H_{slab*adsorbate} - (H_{slab} + H_{adsorbate})$$

where separate calculations were made for the slab, adsorbate, and slab*adsorbate models. Only the most favorable adsorption or absorption configurations are included in this report. When negative, the ΔH_{ads} or ΔH_{abs} are favorable or exothermic, where a stronger adsorption corresponds to a more negative ΔH_{ads} or ΔH_{abs} value.

2.3.1.3 Simulated H Solubilization in PdCu B2 Alloy Surfaces

Prior investigations of H_2/H interactions with the $Pd_{0.50}Cu_{0.50}$ (110) surface in the DE-FG26-05NT42453 contract set the stage for the investigation of the $Pd_{0.50}Cu_{0.44}TM_{0.06}$ (110) surface in this study. Molecular H_2 adsorption/dissociation behavior on the $Pd_{0.50}Cu_{0.44}TM_{0.06}$ (110) surface was assumed to be similar to that on the $Pd_{0.50}Cu_{0.50}$ (110) surface. Molecular H_2 physisorption was predicted to occur 1.6 Å above a $Pd_{0.50}Cu_{0.50}$ (110) Pd atom with a weak binding energy of -17 kJ/mole and 1.8 Å above a $Pd_{0.50}Cu_{0.44}TM_{0.06}$ (110) Pd atom away from the subsurface TM with a binding energy of -22 kJ/mole. The H_2 dissociation was estimated to have a very small barrier of -15 kJ/mole on the $Pd_{0.50}Cu_{0.50}$ (110) surface. Here, molecular H_2 dissociated to chemisorb over adjacent 4-fold sites with a predicted moderate binding energy of -70 kJ/mole. The optimum atomic H binding position on the $Pd_{0.50}Cu_{0.50}$ and $Pd_{0.50}Cu_{0.44}TM_{0.06}$ surfaces was predicted to be at the quasi 3-fold site, just to the side of a 4-fold α hemi-octahedral site. In the latter alloy, this site was away from the subsurface TM.

H solubilizes into, and diffuses between Pd_2Cu_2 tetrahedral sites in both alloys. In the $Pd_{0.50}Cu_{0.44}TM_{0.06}$ (110) surface, H is most stable in the subsurface at a Pd_2Cu_2 tetrahedral site in the vicinity of, but not immediately adjacent to, the subsurface TM. Similar to bulk diffusion, H solubilization follows a tetrahedral-to-tetrahedral pathway inwards from the surface, where the H does not have stable interstitial sites adjacent to the TM. (Relaxation and molecular dynamics calculations have shown that H diffusion is facile next to the TM, where apparently the lengthened Pd–TM bonds allow H to pass by without encountering a barrier). The H solubilization pathway and adsorption/absorption enthalpies in the $Pd_{0.50}Cu_{0.44}TM_{0.06}$ (110) surface are shown in Figure 61 and Figure 62, respectively. The presence of TM in the subsurface decreases the favorability of H solubilization into the lattice. The atomic H adsorption enthalpy on the $Pd_{0.50}Cu_{0.44}TM_{0.06}$ (110) surface is 16.4 kJ/mole less exothermic than on the $Pd_{0.50}Cu_{0.50}$ (110) surface. The enthalpy change for

H to solubilize, from the surface into the first stable subsurface site, is 32.08 kJ/mole more endothermic in the $Pd_{0.50}Cu_{0.44}TM_{0.06}$ (110) surface than on the $Pd_{0.50}Cu_{0.50}$ (110) surface, inferring a higher activation barrier for H solubilization. The H absorption enthalpy 2 layers below the surface quickly approaches the dilute H bulk dissolution energy calculated with a fixed lattice.

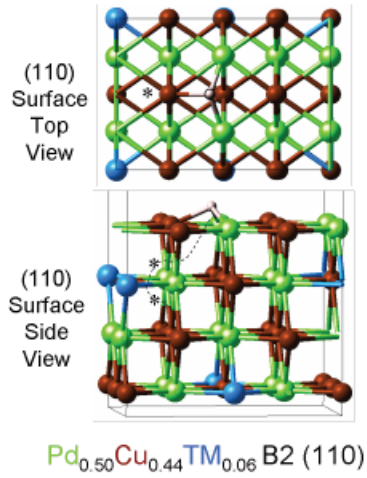

Figure 61: Most favorable H solubilization pathway in $Pd_{0.50}Cu_{0.44}TM_{0.06}$ (110) surface.

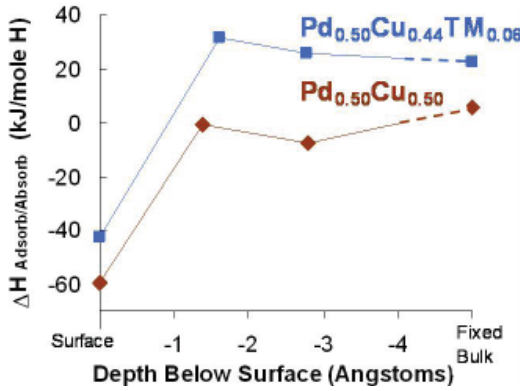

Figure 62: H adsorption/absorption enthalpies, $\Delta H_{ads}/\Delta H_{abs}$, for H solubilization into $Pd_{0.50}Cu_{0.50}$ and $Pd_{0.50}Cu_{0.44}TM_{0.06}$ (110) surfaces.

2.3.1.4 Simulated CO Adsorption and Surface Segregation

Carbon monoxide adsorption was surveyed on various surface sites of the B2 PdCu and $Pd_{0.50}Cu_{0.44}TM_{0.06}$ alloys and of the elements Pd, Ni, and Fe, to enable comparisons with prior results from the DE-FG26-05NT42453 contract and reported in the literature. Carbon monoxide adsorption was predicted to be stronger on the PdCu alloy than on the $Pd_{0.50}Cu_{0.44}TM_{0.06}$ alloy. The most stable configuration for the former was in a four-fold "long-bridge" site over a sub-surface Pd and for the latter was on-top of a Pd atom away from the TM subsurface atom. However, the CO adsorption strengths were dramatically

reduced on these alloys compared to that on the other elements simulated in this study. Simulation of CO dissociation to adjacent atomic adsorbates was found to be unstable to CO reformation on $Pd_{0.50}Cu_{0.44}TM_{0.06}$, and unfavorable on PdCu. The adsorption of C (referenced to graphite) was found to be very unfavorable on both alloys, being even more unfavorable on $Pd_{0.50}Cu_{0.44}TM_{0.06}$.

The most favorable CO adsorption on the $Pd_{0.50}Cu_{0.50}$ (110) surface has a strong binding energy of -138 kJ/mole, as shown in Table 12. However, the CO binding is much weaker compared to that on the other transition metal surfaces included for comparison: Fe (110), Ni (111), and Pd (111). The CO adsorption on top Pd on PdCu B2 alloys is substantially reduced from the tridentate binding on Pd (111) due to the diluting effect of the weaker binding Cu atoms. Table 13 shows that if a subsurface Pd atom is exchanged with a surface Cu atom to mimic Pd segregation, CO adsorption is significantly enhanced to -163 kJ/mole, because CO then changes from binding on top Pd to tridentate 3-fold binding to surface Pd atoms. Here, the strong CO adsorption may induce Pd segregation. CO adsorption on the electron-rich $Pd_{0.50}Cu_{0.44}TM_{0.06}$ (110) is weakened to -125 kJ/mole. Simulations have shown that both Pd and TM surface segregation are very unfavorable on the $Pd_{0.50}Cu_{0.44}TM_{0.06}$ (110) surface. CO binding on a Pd-segregated $Pd_{0.50}Cu_{0.44}TM_{0.06}$ (110) is even weaker. Thus, the TM substituent significantly reduces both the binding of the prevalent CO reforming reactant and stabilizes against possible compositional variations from CO-induced Pd segregation.

Once bound to the surface, CO may dissociate alone to form atomic C and O adsorbates on the surface, or, in concert with another CO molecule to form a C adsorbate and to release CO_2 via the Boudouard reaction. The tendency for CO dissociation was investigated by minimizing adsorbed C in the most stable 4-fold β hemi-octahedral positions over subsurface Pd and adsorbed O in an adjacent quasi 3-fold α hemi-octahedral position. On the $Pd_{0.50}Cu_{0.50}$ (110) surface, this led to a substantial unfavorable, endothermic enthalpy change, +238 kJ/mole, compared to the adsorbed CO configuration. On the $Pd_{0.50}Cu_{0.44}TM_{0.06}$ (110) surface, the dissociated CO configuration was not stable, the CO molecule reformed on top of Pd during the minimization. These results indicate that CO dissociation to form C, possibly leading to coke, is not favorable on the PdCu B2 alloy surfaces. The prediction results indicate that addition of the ternary TM alloying element may actually enhance the reverse conversion of adsorbed carbon to CO to counter coke formation reactions.

Table 12: Adsorption enthalpies, ΔH_{ads} for 0.25 monolayer CO adsorption on PdCu B2 alloys and some standard state metals.

Alloy / Metal	Bulk Symmetry	Surface Miller Plane	Adsorption Site Description	ΔH_{ads} kJ/mole*atom
$Pd_{0.50}Cu_{0.50}$	Pm-3m	(110)	on top Pd	-138.09
$Pd_{0.50}Cu_{0.44}TM_{0.06}$	Pm-3m	(110)	on top Pd, away from subsurface TM	-115.85
Fe	Im-3m	(110)	on top Pd	-185.37
Ni	Fm-3m	(111)	hcp (3-fold)	-185.52
Pd	Fm-3m	(111)	hcp (3-fold)	-218.12

Table 13: PdCu B2 alloy segregation enthalpies, ΔH_{seg}, and 0.25 ML CO adsorption enthalpies, ΔH_{ads}, for varying surface alloy compositions.

Surface Condition / PdCu B2 (110) Surfaces	Segregation Enthalpy ΔH_{seg} (kJ/mole)	CO Adsorption Enthalpy ΔH_{ads} (kJ/mole)
$Pd_{0.50}Cu_{0.50}$		
Native Surface	-	-138.1
Surface Pd Segregation	9.3	-163.1
$Pd_{0.50}Cu_{0.44}TM_{0.06}$ with subsurface TM		
Native Surface	-	-124.5
Surface Pd Segregation	50.9	-112.2
Surface TM Segregation	85.2	N.D.

2.3.1.5 Simulated C Surface Adsorption, Subsurface Absorption and Bulk Solubilization

Carbon surface and bulk interactions were profiled in the PdCu B2 alloys and compared to those for a range of well-known metals, to establish a basis for understanding tendencies for coke precursor formation. All C binding energies were determined with respect to CO gas using the Boudouard reaction, since this is the likely source of adsorbed and interstitial carbon: $2CO_{gas} + M \rightarrow M*C + CO_{2\ gas,}$ where M is the metal (alloy) surface slab or bulk model, and M∗C is the transition metal surface with adsorbed C or bulk model with absorbed C. CO adsorption was directly not taken into consideration here, since CO adsorption was not simulated on all the metals included in the carbon adsorption simulations. However, it is implicit that the remaining C atom, after O is extracted from a CO molecule by reaction with a second CO molecule to form CO_2, will adsorb onto the surface. Carbon binding was also determined with respect to graphite, the standard state for elemental carbon.

Atomic modeling results showed that precursor structures for coke/carbon formation were dramatically less stable on the B2 PdCu alloy, and became even more unstable in the B2 $Pd_{0.50}Cu_{0.44}TM_{0.06}$ alloy, compared to their relative stability on the alloys' constituent elements {Pd, Cu} and 5 other common elements employed in reactor construction {Ti, Zr, Fe, Cr, Ni}. The adsorption of C (referenced to graphite) was found to be very unfavorable on both Pd–Cu alloys, being even more unfavorable on $Pd_{0.50}Cu_{0.44}TM_{0.06}$. In comparison, C adsorption on most elements ranged from being favorable to being moderately unfavorable. A similar trend was predicted for C subsurface absorption in the most stable octahedral site for the membrane alloys compared to the elements. Here, C subsurface solubilization was most unfavorable for the $Pd_{0.50}Cu_{0.44}TM_{0.06}$ alloy and least unfavorable for Ni and Fe. Carbon adsorption was moderately unfavorable in the PdCu alloy, and became slightly less favorable with the TM addition in the $Pd_{0.50}Cu_{0.44}TM_{0.06}$ alloy.

The most favorable carbon surface adsorption on the PdCu B2 (110) alloy surfaces was the 4-fold configuration in the center of β hemi-octahedral sites flush with the surface over an underlying Pd atom. These sites were virtually indistinguishable in energy from the adjacent quasi 3-fold sites. The adsorption enthalpies, ΔH_{ads}, in Table 14 show that C binding is much weaker on the PdCu B2 alloys, even weaker (less negative) on the $Pd_{0.50}Cu_{0.44}TM_{0.06}$ (110) alloy, than on common reactor metals, with the exception of Cu which is known to be very resistant to coke formation. Thus, the filled d-levels in Pd and Cu are less reactive with the carbon atom than metals with less complete d-shells earlier in the transition metal series. The addition of the ternary alloy element decreases the interaction of C with the PdCu B2 alloy surface; these interactions would become even more unfavorable with increasing C coverage.

Table 14: Adsorption enthalpies, ΔH_{ads} for 0.25 monolayer C adsorption on PdCu B2 alloys and standard state metals.

Alloy / Metal	Bulk Space Group	Surface Crystal Plane	Adsorption Site Description	ΔH_{ads} with respect to Boudouard reaction kJ/mole*atom	ΔH_{ads} with respect to graphite kJ/mole*atom
$Pd_{0.50}Cu_{0.50}$	Pm-3m	(110)	long bridge (4-fold)	-134.27	114.09
$Pd_{0.50}Cu_{0.44}TM_{0.06}$	Pm-3m	(110)	long bridge (4-fold)	-80.09	168.26
Ti	$P6_3/mmc$	(0001)	quasi-fcc (3-fold)	-235.69	12.67
Cr	Im-3m	(110)	long bridge (4-fold)	-263.54	-15.18
Fe	Im-3m	(110)	long bridge (4-fold)	-351.66	-103.30
Ni	Fm-3m	(111)	hcp (3-fold)	-154.05	94.31
Cu	Fm-3m	(111)	fcc (3-fold)	30.74	279.10
Zr	$P6_3/mmc$	(0001)	quasi-hcp (3-fold)	-246.37	1.99
Pd	Fm-3m	(111)	fcc (3-fold)	-178.56	69.80

To evaluate bulk carbon adsorption, full relaxation was conducted in supercells with 3.125% interstitial substituted C in the $Fm\bar{3}m$ standard state elements Cu, Ni, Pd, and with 6.25 % interstitial substituted C in the remaining $Im\bar{3}m$ and $P6_3/mmc$ standard state elements and B2 alloy phases. Carbon was most stable in interstitial octahedral sites in all bulk phases, with slightly favorable adsorption predicted for Ti, and the most unfavorable adsorption predicted for Cr, Cu and Zr.

Carbon subsurface solubilization with the concomitant lattice strain is even less favorable on the PdCu B2 alloys. This can be observed by comparing the Table 15 absorption enthalpies, ΔH_{abs}, for 0.25 ML C absorption in α-octahedral sites just below the surface, where for the most favorable $Pd_{0.50}Cu_{0.44}TM_{0.06}$ (110) subsurface α-octahedral site is next to the subsurface TM, to the 0.25 ML C surface adsorption ΔH_{ads} values in Table 14. Subsurface absorption of 0.25 ML C was also simulated in two of the mid-transition metal surfaces, Fe (110) and Ni (111). Both metals accommodate C in octahedral interstitial sites more favorably (more exothermically) than the PdCu B2 alloys. Interestingly, subsurface C absorption is more favorable than surface adsorption in the Ni (111) surface. These

predictions give insights into the influence of C solubilization on coke nucleation. Increased C solubility in the metal subsurface promotes C saturation, leading to C surface segregation and heterogeneous nucleation of coke formation.

Carbon bulk solubility was simulated in the PdCu B2 alloys in comparison with the same metals included in the carbon surface adsorption studies. In all alloy and metal structures, C substituted most favorably in the octahedral interstitial sites. The C substituted bulk structures were fully minimized, including lattice parameters and atomic positions, to enable C accommodation in the lattice and strain relaxation. This is different in approach than for the surface adsorption/absorption studies where the metal lattice parameters were fixed by the underlying bulk structure. The results in Table 16 show that the ΔH_{abs} for C absorption is moderately favorable in the PdCu B2 alloys, being slightly less favorable in the $Pd_{0.50}Cu_{0.44}TM_{0.06}$ alloy. The ΔH_{abs} for C absorption in the other metals range from very favorable substitution in Ti to unfavorable substitution in Cu, with respect to the Boudouard reaction. When referenced to the most stable C graphitic phase, C substitution is unfavorable in the PdCu B2 alloys and all the metals, except Ti.

2.3.1.6 Competitive Adsorption of H_2S and Cl Contaminants

Atomic simulations profiled the adsorption of H_2S and Cl to represent possible sulfur and chlorine-bearing coal gas contaminants that may strongly bind to Pd and block H solubilization. In the most favorable adsorption configurations, the H_2S bonds on top of Pd on the $Pd_{0.50}Cu_{0.44}TM_{0.06}$ (110) surface, away from the subsurface TM, in a similar surface configuration to that on the $Pd_{0.50}Cu_{0.50}$ (110) surface. The TM substituent increases the electron density of the surface Pd Lewis acid site, lowering the nucleophilic binding of H_2S by 10 kJ/mole, to -62 kJ/mole on the $Pd_{0.50}Cu_{0.44}TM_{0.06}$ (110) surface. This may not point to a competitive advantage since atomic H adsorption is also weakened on this surface. The adsorption of the Cl ion is most favorable at the center of the 4-fold β hemi-octahedral sites on both (110) surfaces. The strong -190 kJ/mole binding of the electrophilic Cl ion on the $Pd_{0.50}Cu_{0.44}TM_{0.06}$ (110) surface is enhanced compared to the -175 kJ/mole Cl binding on the $Pd_{0.50}Cu_{0.50}$ (110) surface. The Cl ion is a much stronger poison than H_2S, where H_2S has a similar magnitude binding to atomic H.

Table 15: Absorption enthalpies, ΔH_{abs}, for subsurface absorption of 0.25 monolayer C just below the surface of PdCu B2 alloys and standard state metals.

Alloy / Metal	Bulk Space Group	Surface Crystal Plane	Adsorption Site Description	ΔH_{ads} with respect to Boudouard reaction kJ/mole*atom	ΔH_{ads} with respect to graphite kJ/mole*atom
$Pd_{0.50}Cu_{0.50}$	Pm-3m	(110)	α-octahedral site	-105.66	142.70
$Pd_{0.50}Cu_{0.44}TM_{0.06}$	Pm-3m	(110)	α-octahedral site adjacent to TM	-54.85	200.24
Fe	Im-3m	(110)	octahedral site	-140.21	-140.21
Ni	Fm-3m	(111)	octahedral site	-186.41	61.95

Table 16: Absorption enthalpies, ΔH_{abs} for bulk C absorption in PdCu B2 alloys and standard state metals.

Alloy / Metal	Bulk Space Group	Number Bulk Atoms	Atomic % C Solute	ΔH_{ads} with respect to Boudouard reaction kJ/mole*atom	ΔH_{ads} with respect to graphite kJ/mole*atom
$Pd_{0.50}Cu_{0.50}$	Pm-3m	16.00	6.30	-5.57	9.95
$Pd_{0.50}Cu_{0.44}TM_{0.06}$	Pm-3m	16.00	6.30	-4.71	10.82
Ti	P_{63}/mmc	16.00	6.30	-24.72	-9.20
Cr	Im-3m	16.00	6.30	0.57	16.09
Fe	Im-3m	16.00	6.30	-10.74	4.79
Ni	Fm-3m	32.00	3.10	-5.22	2.54
Cu	Fm-3m	32.00	3.10	10.16	17.92
Zr	P_{63}/mmc	16.00	6.30	7.16	22.68
Pd	Fm-3m	32.00	3.10	-5.08	2.68

2.3.1.7 Sulfur Adsorption Simulations

Sulfur adsorption from the decomposition of H_2S or other S-bearing species could possibly induce selective surface segregation of alloy constituents or lead to the formation of a reacted corrosion layer, such as the irreversible formation of a low H-permeable Pd_4S layer recently reported on Pd in the presence of H_2S (Morreale et al., 2007). Although irreversible corrosion product formation (i.e. Pd_4S) has been reported on a number of Pd-based alloys exposed to S-bearing atmospheres (Morreale, 2006 & 2007), S adsorption was observed at UTRC to be reversible on a $Pd_{0.75}Cu_{0.25}$ alloy with recoverable H permeability at higher temperatures. This finding motivated the conduction of a systematic first principles atomic modeling study to pinpoint alloy characteristics that control the reversibility/irreversibility of S interactions on a range of Pd-based alloys. The goal was to use this understanding to develop a predictive tool to guide the development of S-tolerant alloys for dense metallic hydrogen-selective membranes. Atomic modeling simulations were conducted to investigate S interactions with a series of candidate H selective membrane PdCu and PdAg alloys and their constitutive metals. The purpose of these simulations was: a) to identify the controlling factors for S ad/absorption for a range of alloy chemical and geometrical features, and b) to predict the equilibrium coverage for S for varying membrane operating parameters.

Atomic simulations were made on the lowest energy four layer (110) surface slabs of PdCu B2 ordered BCC, PdCu ordered FCC, and $Pd_{0.50}Cu_{0.44}TM_{0.06}$ BCC alloys, where in the latter the ternary TM element was substituted in the most stable subsurface layer positions. Sulfur adsorption was profiled at the hemi-octahedral four-fold positions formed by the lengthwise surface cleavage of the PdCu alloy bulk α-Pd_2Cu_4 and the β-Pd_4Cu_2 octahedra. The adsorption enthalpies in Table 17 show that S bonded strongly in the four-fold position over the hemi-β octahedral site subsurface Pd in both BCC alloys, and even more strongly in the hemi-α octahedral site overlying subsurface Cu in the FCC alloy. Sulfur-adsorption induced surface segregation was profiled by exchanging subsurface Pd,

Cu or TM with other elements in surface atomic positions adjacent to the strongest S adsorption site. Even though S atomic adsorption was moderately strong, less favorable S adsorption enthalpies were obtained over the same sites on the partially Pd-, Cu- or TM-segregated PdCu and $Pd_{0.50}Cu_{0.44}TM_{0.06}$ bcc alloy surfaces, as shown in Table 17.

The S adsorption over the partially Pd-segregated PdCu FCC phase was at least equivalent in favorability to the unsegregated surface. This could be due to the fact that though the PdCu FCC model was artificially ordered for convenience, while in reality Pd-Cu FCC compositions do not have separate sublattices for preferential occupation of Pd and Cu, as in the ordered Pd-Cu B2 BCC phases. However, a more significant reduction in favorability was noted for partial Cu segregation on the PdCu fcc surface. Since a significant increase in favorability was not modeled for any of the partial segregation scenarios, it can be interpreted that the PdCu-based BCC and FCC alloys are stable against surface segregation even in the presence of S.

Additional calculations were made to examine S stability in the PdCu-based alloys' subsurface interstitial α and β octahedral positions just below the surface. In all cases during the relaxation, the subsurface S was unstable and migrated to the surface, often causing buckling of the overlying atoms and yielding unfavorable absorption enthalpies. While it is possible that S may be stable substituted further below the surface, these results indicate that S solubilization is an endothermic process with a very large barrier and is unlikely to occur. This interpretation is corroborated by the lack of experimental observation of S-induced irreversible corrosion layers following exposure of PdCu FCC alloys to S-bearing atmospheres.

Table 17: Ground state sulfur adsorption enthalpies on PdCu-based alloy surfaces.

Alloy (110) Surface	S Adsorption Octahedral Site	S Adsorption, ΔH_{ads} (kJ/mole)			
		As-Cleaved	Pd Seg	Cu Seg	TM Seg
PdCu bcc	Hemi-β	-154.0	-125.4	-99.4	-
$Pd_{0.50}Cu_{0.44}TM_{0.06}$ bcc	Hemi-β	-158.8	-99.4	-91.4	-69.6
PdCu fcc	Hemi-α	-185.6	-191.7	-147.8	-

Adsorption (absorption) simulations of varying S coverages on a range of alloy surfaces: PdCu $Im\bar{3}m$ (110), PdCu P_4mmm (110)/(101), $Pd_{0.75}Cu_{0.25}$ $Fm\bar{3}m$ (111), $Pd_{0.75}Ag_{0.25}$ $Fm\bar{3}m$ (111), and Pd $Fm\bar{3}m$ (111) (all compositions given in atomic %), showed a clear correlation of the adsorption (absorption) enthalpy versus the alloy electronic characteristics, where the latter has a direct influence on alloy lattice parameters and surface energies. The atomic modeling studies showed that the S interactions were predominantly influenced by the d-band electronic characteristics, which are a manifestation of the alloy chemistry and symmetry. The favorability of adsorption enthalpy increased (tendency toward negative values) with the increasing difference [d band center – S p bonding peak position] determined from the S-modified alloy model electronic density of states. A very tight correlation was found between the difference [d-band center - adsorbed S p bonding peak] and the sulfur adsorption enthalpy. Here, bonding involved the coupling of metal d-band orbital with the S p peak, splitting the latter into a lower energy p bonding peak and a

higher energy p anti-bonding peak. The stronger (lower) the S adsorption enthalpy, the more the S p bonding peak shifted to lower energies and the greater the difference from the d-band center. This is shown in Figure 63.

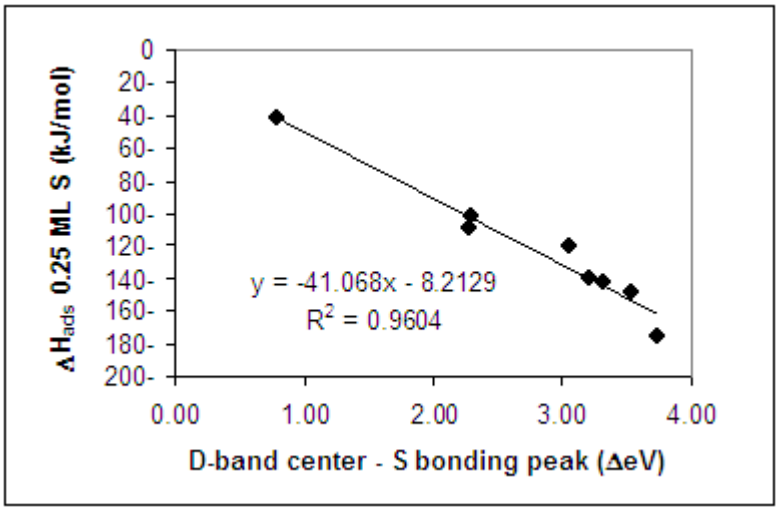

Figure 63: The correlation of enthalpies of adsorption of 0.25 monolayer (ML) S with S electronic interactions on a series of Pd-Cu and Pd-Ag alloys, and their constitutive elements.

Finite temperature surface energy calculations were made to predict the most favorable S interactions under varying temperature and H_2S/H_2 gas partial pressure compositions. Only up to a maximum surface coverage of 0.25 ML S was found for all evaluated conditions. The change in surface energy with temperature for 0.25 ML S coverage equilibrated under 19.99 Bar H_2 and 4 $x10^{-4}$ Bar H_2S (~20 ppmv) mixed gas partial pressures, is shown in Figure 64. The surface energies for S-modified alloy surfaces increase with temperature, eventually crossing the constant surface energy corresponding to the bare alloy surface, as shown in Figure 64. Each prediction is marked with the intersection with the bare surface energy. The temperature of this intersection corresponds to the lower limit for the bare surface as the equilibrium condition. Since the bare surface energy is lower at higher temperatures, this intersection corresponds to the temperature onset for equilibrium desorption of the 0.25 ML S adsorbates. The onset temperatures for S desorption shows a clear correlation with the alloy electronic characteristics, so that the onset temperature increases as the S-modified alloy surface difference [d band center – S p bonding peak position] increases (or the bonding interaction increases). Subsurface S absorption and accompanying Pd segregation would require a higher equivalent equilibrium S coverage. Thus, only reversible sulfur adsorption was predicted to occur on homogeneous alloy surfaces. Irreversible S absorption and S-bearing scale formation are anticipated to occur at higher energy, more reactive surface heterogeneities.

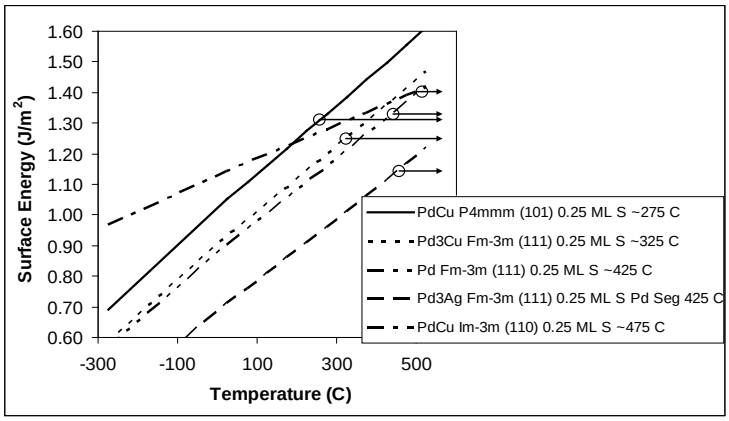

Figure 64: Finite temperature surface energy predictions marked with bare surface energies.

With increasing S coverage, several scenarios can play out on an alloy surface: a) the surface can become saturated and passivated with a S monolayer, b) S-S interactions can become stronger than the metal-S interactions, causing S coupling and desorption of S_2, or c) S can partially submerge subsurface, promoting surface alloy segregation to nucleate corrosion product formation. The predominance of a particular scenario on a given surface depends on the relative enthalpies for S adsorption or S_2 coupling versus S absorption, and the reaction enthalpy for Pd segregation and Pd_4S formation upon S absorption. This relationship is shown by the plot in Figure 65, where the former is represented by the abscissa, and the latter by the ordinate axis. In the plot, the tendency for S incorporation (towards a negative favorable value), correlates with both reported observations of irreversible S interactions with $Pd_{0.75}Ag_{0.25}$ and Pd, and UTRC's observations of S reversibility on $Pd_{0.75}Cu_{0.25}$. Once the S incorporation becomes favorable, the tendency for corrosion product formation is dictated by the favorability for Pd segregation or in the case of Pd, Pd_4S formation.

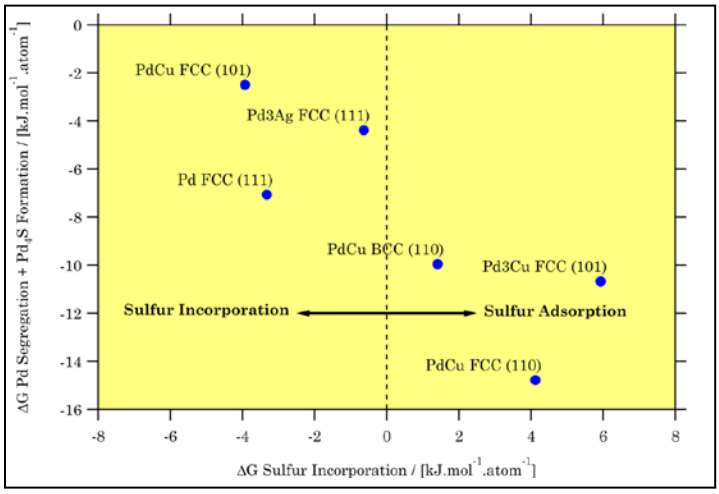

Figure 65: The analysis of reaction enthalpy for Pd segregation and Pd_4S formation upon S absorption versus the change in enthalpy for S incorporation by absorption relative to S adsorption. This serves as a predictive tool to delineate irreversible from reversible S interactions.

2.3.2 Pd-alloy/Nanoporous Oxide Membrane Simulations

2.3.2.1 Coefficient of Thermal Expansion and Interface Atomic Simulation Methodologies

A first principles interface predictive capability was implemented to guide material development for improved Pd-alloy/nanoporous oxide membrane H selectivity and thermomechanical performance. Specifically, atomic modeling was used to investigate interfacial adhesion between composite phases within the Pd-alloy/nanoporous oxide membrane which is difficult to experimentally observe directly, yet is crucial to maintaining membrane high H_2 selectivity over a long life involving large pressure drops and thermal cycling. These simulations required the implementation of new theoretical methodologies to progressively build up to models of increasing complexity: starting with the prediction of optimum bulk, surface, and interface structures, following with the determinination of the bulk phase coefficients of thermal expansion (CTE), and culiminating with evaluation of the adhesion of the relevant interfaces expanding as a function of temperature. The implementation was initially focused on the design of the Y-stabilized ZrO_2 (YSZ) / $Pd_{0.875}Au_{0.125}$ interface (all values in atomic %); and then later shifted to the YSZ / stainless steel interface. The location of these interfaces is shown schematically in Figure 66.

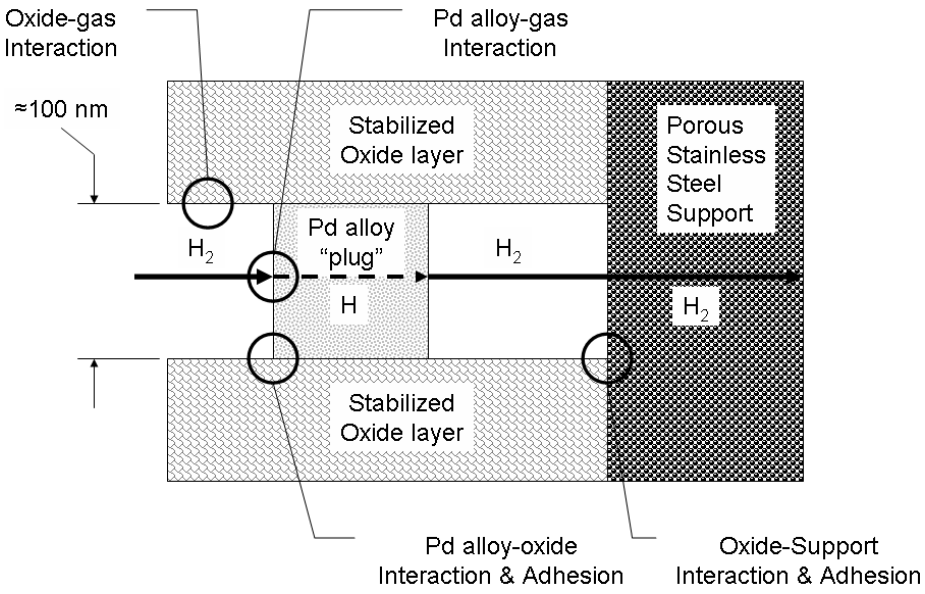

Figure 66: Pd-alloy/nanoporous oxide membrane schematic.

The efforts included working in collaboration with Materials Design, Inc., to develop and implement a coefficient of thermal expansion (CTE) predictive methodology based on the description of bulk phase thermodynamic stability as a function of volume and temperature. First, the direct method lattice dynamics method was used to predict phonon spectra and to determine the free energy as a function of temperature, for each of a range of lattice volumes. Then, a temperature–volume transformation of the predicted data was conducted to determine the minimum energy lattice volume as a function of temperature.

These predicted values were fit to a line equation to determine the CTE over the desired temperature range.

Interfaces were constructed from minimized bulk lattices having volumes that corresponded to selected temperatures within the predicted CTE temperature range. The minimum energy surfaces were then created from the bulk structures and were used to construct interfaces with the Materials Design, Inc., Interfaces module. This module found the minimum interfacial repeating unit that provided the best lattice match for the two layers by varying the *a*, *b*, and γ latttice parameters, as well as the angle between the two layers (the bedding angle). The registration between the two layers was then optimized by systematically shifting the upper layer in the x and y directions, until the minimum energy configuration was found. In addition, the interfacial spacings between the layers was also minimized by stepwise adjustments. The double interface was then minimized and used to determine the interfacial energies referenced to the original consituent bulk phases and adhesion energies referenced to the energies of the separately minimized constituent layers, both in J/m^2.

2.3.2.2 Simulation of Pd–Au alloy/Nanoporous Zirconia Interface

The first atomic modeling phase focused on examining the 88.9 ZrO_2 – 11.1 $YO_{1.5}$ [11.1 Yttria-stabilized zirconia (11.1 YSZ)]/ $Pd_{0.875}Au_{0.125}$ alloy interface formed within the collodial plugged porous oxide membrane layer. The 11.1 YSZ bulk structure falls within the metastable, kinetically-stablized, non-transformable *t'* region of the ZrO_2 – $YO_{1.5}$ phase diagram (Yashima, 1996). The most favorable atomic model of this phase has a $P\text{-}4m_2$ tetragonal structure with pairs of Y ions substituted in a tetrahedral arrangement in the Zr sublattice of the ZrO_2 $P4_2/nmc$ phase and 1 O vacancy formed for each doped Y pair in the next nearest O neighbor position (Eichler, 2001). The minimized 11.1 YSZ bulk phase had lattice parameters that were in excellent agreement with experimental values (<<1 % difference) and formed the most stable surface along the (101) crystallographic plane. The 87.5 Pd12.5 Au alloy was formed by substituting Au on the Pd lattice, while maintaining the host lattice $Fm\text{-}3m$ symmetry. The minimized alloy bulk lattice constants were also in excellent agreement with measured values, and formed the most stable surface along the (111) plane.

An example of the newly implemented CTE predictions is shown in Figure 67 for the change in lattice parameter and CTE with temperature for the $Pd_{0.875}$ $Au_{0.125}$ alloy. The $Pd_{0.875}Au_{0.125}$ alloy was predicted to have a $\alpha=17.01 \times 10^{-6}$ / ºC at 525 ºC, where experimentally CTE values of $\alpha=15.27 \times 10^{-6}$ / ºC and of $\alpha=16.52 \times 10^{-6}$ / ºC were measured for Pd and Au at 525 ºC (Dutta, 1963a&b). The comparison of the temperature dependencies of the *a* lattice parameter and the CTE values of these phases is shown in Figure 67. The predicted results were consistent with experimental measurements reported for the Pd and Au alloying elements. The predicted CTE for the 11.1 YSZ phase with the anisotropic *t'* tetragonal structure were determined separately for the *a* and *c* lattice parameters to be $\alpha = 10.2 \times 10^{-6}$ / ºC and $\alpha = 19 \times 10^{-6}$ / ºC at 525 ºC, respectively. Only isotropic CTE values have been presented for cubic or *t'* YSZ phases in the literature. The 11.1 YSZ predicted CTE for the *a* lattice parameter compared well with the 11.6×10^{-6} / ºC average temperature values quoted for the *t'* YSZ phase (Bannister, 1988). Although the CTE predictions for both the 11.1 YSZ and 87.5 Pd12.5 Au alloy phases could not be directly validated with experimental data, the predictions showed good consistency in indirect

comparisons with closely related experimental data, such as the data of Hayashi, *et. al*, in Figure 68 (Hayashi, 2005).

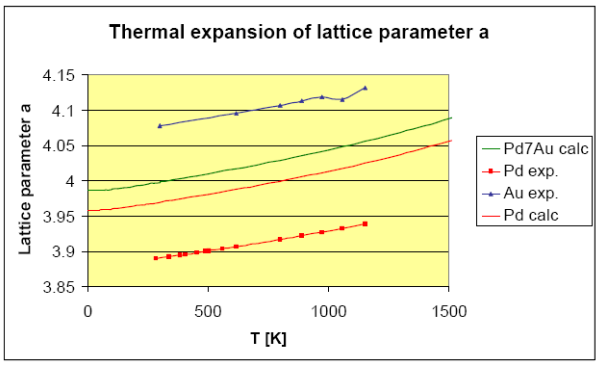

A

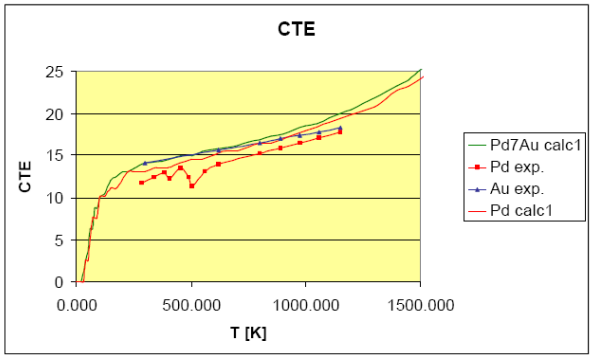

B

Figure 67: Lattice parameters (A) and linear CTE (B) as a function of temperature predicted for $Pd_{0.875}Au_{0.125}$ alloy compared to Pd and Au experimental data.

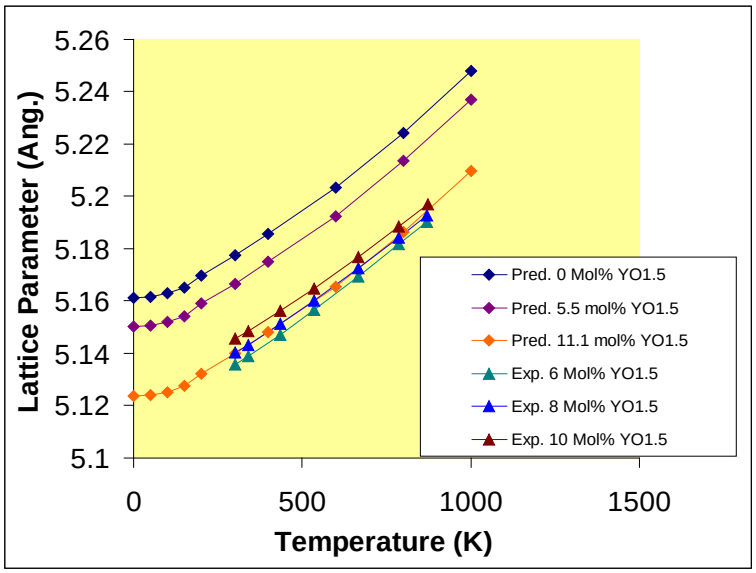

Figure 68: Comparison of predicted c lattice parameters of t' tetragonal yttria-stabilized zirconia (YSZ) with experimental a lattice parameter of cubic YSZ formed with varying mole % yttria from Hayashi, et. al (Hayashi, 2005).

The 11.1 YSZ (101) / 11.1 YSZ $Pd_{0.875}Au_{0.125}$ (111) interfaces were prepared by joining slabs formed from the bulk phases with the ground state minimized lattice parameters (≈-273 ºC), and also with the 525 ºC lattice parameters determined from the CTE predictions. Interfaces were then constructed adjoining the materials' most stable surfaces, where the interface registration and atomic positions were optimized with first principles minimizations. The double interface model is shown in Figure 69. The interface adhesion (work of separation) was then determined from the optimized interfaces. For example, an 11 %$YO_{1.5}$-89 % ZrO_2 / $Pd_{0.875}Au_{0.125}$ interface with ground state (≈0 K) lattice parameters

was predicted to have an adhesion of 1.4 J/m^2, which was stronger than the undoped ZrO_2 / $Pd_{0.875}Au_{0.125}$ interface with an adhesion of 0.9 J/m^2 at the same temperature. Simulations of the 11 %$YO_{1.5}$-89 % ZrO_2 / $Pd_{0.875}Au_{0.125}$ interface constructed with 525 ºC lattice parameters show that the high temperature interface adhesion is as good, or better, than for the low temperature. The interfacial energies and adhesion energies determined for the two different conditions were not significantly different, as shown in Table 18, indicating that despite the difference in the CTE between the 11.1 YSZ and the $Pd_{0.875}Au_{0.125}$ phases, a loss in adhesion is not anticipated upon thermal cycling from room temperature to over 500 ºC.

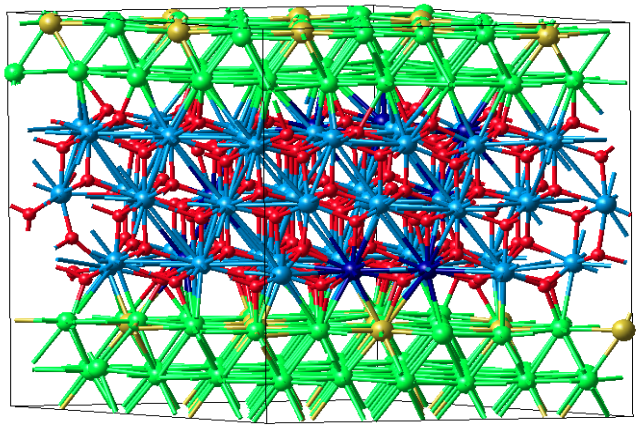

Figure 69: The 88.9 ZrO_2 – 11.1 $YO_{1.5}$ (101) / $Pd_{0.875}Au_{0.125}$ alloy (111) double interface prepared with the ground state minimized lattice parameters. The atoms are colored as follows: Pd– green, Au– gold, O– red, Zr– blue, and Y– dark blue.

Table 18: Predicted 88.9 ZrO_2 – 11.1 $YO_{1.5}$ (101) / $Pd_{0.875}Au_{0.125}$ (111) double interface.

Temperature (ºC)	Interface Energy (J/m^2)	Adhesion Energy (J/m^{2+})
~-273	2.1	1.45
525	2.0	1.76

2.3.2.3 Simulation of Stainless Steel/Nanoporous Zirconia Interface

Final atomic modeling efforts focused on the 310 stainless steel (310 SS)/11.1 $YO_{1.5}$ –88.9 ZrO_2 interfaces within the membrane structure. This modeling phase built upon prior results from the investigation of the 11.1 YSZ/ $Pd_{0.875}Au_{0.125}$ alloy interface. The 310 SS weight % composition of 24-26 Cr, 19-22 Ni, and less than 2 each other alloying constituents, was approximated with an atomic model containing in atomic % (weight %): 53 (53) Fe, 28 (26) Cr, and 19 (21) Ni (53Fe 28Cr 19Ni). The alloy lattice atomic model was formed by symmetrically substituting Cr and Ni on the Fe face-centered cubic (FCC) lattice, resulting in an alloy structure with $P4/mmm$ symmetry. The minimization of this alloy model was iterated by hand, in order to enforce the FCC symmetry that is known to occur experimentally. The minimum energy equivalent FCC lattice parameter was determined to

be 3.52 Å by this method. This minimized bulk structure was then cleaved along the (111) surface plane to form an expanded surface slab of four layers thickness. Interfaces were constructed, using the same 3 layer 11.1 YSZ phase (101) slab configuration, as was used previously for the 11.1 YSZ/ $Pd_{0.875}Au_{0.125}$ interface. Since the YSZ phase elastic modulus is slightly larger than that of 310 SS (www.matweb.com, 2010), the interfaces were constructed fixing the YSZ lattice parameters, and straining the 53 Fe 28 Cr 19 Ni alloy lattice to optimize interfacial registration with the YSZ lattice. New CTE simulations were not necessary for either material in this interface pair, since the CTE for 11.1 YSZ t' phase was previously simulated and the CTE for 310 SS is well-known experimentally (16.9 µm/m-°C from 0 to 540 °C (www.matweb.com. 2010)). Invoking the assumption that the change in local dimensions of the bonded interface with temperature is determined by the CTE of the higher modulus material, the change in lattice parameter with temperature from the CTE simulated for the YSZ *t'* phase was used to adjust the lattice parameters of the bonded interface for expansion with increasing temperature. Interfaces were optimized with the ground state minimized lattice parameters that approximately represented the temperature of ≈-273 ºC, and also with the 525 ºC lattice parameters determined from the CTE predictions. The low temperature double interface model is shown in Figure 70. The adhesion energies determined for the two different conditions were not significantly different, 3.04 and 3.19 J/m^2, respectively, indicating that despite the difference in the 11.1 YSZ *t'* and the 310 SS phase CTE values, a loss in adhesion is not anticipated upon thermal cycling from room temperature to over 500 ºC.

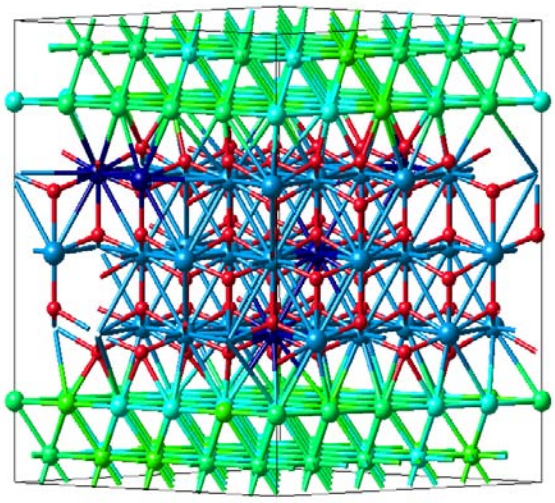

Figure 70: The 53 Fe 28 Cr 19 Ni alloy (111)/11.1 $YO_{1.5}$ –88.9 ZrO_2(101) double interface prepared with the ground state minimized lattice parameters. The atoms are colored as follows: Fe-light green, Ni-chartreuse, Cr-turquoise, O- red, Zr-blue, and Y-dark blue.

3 Conclusion

This project successfully increased the technology readiness level of palladium-based metallic membranes for hydrogen separation from coal-biomass gasifier exhaust or similar hydrogen-containing gas streams. The reversible tolerance of palladium-copper (PdCu)

alloys was demonstrated for H_2S concentrations varying from 20 ppmv up to 487 ppmv and NH_3 concentrations up to 9 ppmv. In addition, atomistic modeling validated the resistance of PdCu alloys to carbon formation, irreversible sulfur corrosion, and chlorine attack.

The experimental program highlighted two key issues which must be addressed as part of future experimental programs. These were membrane tube defects and non-membrane materials of construction. Four out of five FCC PdCu separators developed leaks during the course of the experimental program because ≈10% of the alloy tubes contained a single defect that resulted in a thin, weak point in the tube walls. These defects limited operation of the existing tubes to less than 220 psig. Future separators should be designed to account for such defects and better manufacturing approaches should be investigated to eliminate defective tubes from becoming part of the membrane separators.

For commercial applications of a PdCu alloy hydrogen separator under high sulfur concentrations, stainless steel 316 was determined to not be suitable for housing or supporting the device. Testing with sulfur concentrations of 487±4 ppmv resulted in severe corrosion of the stainless steel components of the separators. Further investigation is necessary to determine the best materials to construct hydrogen separators so that the non-Pd parts of the devices can be as durable as the membranes.

The project identified an experimental methodology for quantifying the impact of gas contaminants on PdCu alloy membrane performance as well as an atomistic modeling approach to screen metal alloys for their resistance to irreversible sulfur corrosion. Initial mathematical descriptions of the effect of species such as CO and H_2S were developed, but require further experimental work to refine. At the end of the project, an improvement to the experimental approach for acquiring the necessary data for the permeability model was made and demonstrated in preliminary tests on an enhanced PdCu separator.

All of the key DOE 2010 technical targets were met or exceeded except for the hydrogen flux. The highest flux observed for the project, 125 $ft^3ft^{-2}h^{-1}$, was obtained on a single tube separator with the aforementioned enhanced PdCu separator with a hydrogen feed pressure of 185 psig at 500 °C. Further investigation of this enhanced PdCu may yield higher fluxes so that all of the DOE goals can be met.

4 References

Bannister, M.J.; Rajendran, S. "Thermal expansion of tetragonal zirconia polycrystalline ceramics," Materials Science Forum (1988), 34-36(Int. Ceram. Conf., AUSTCERAM 88, Pt. 1), 207-11.

Chiesa, P.; Consonni, S.; Kreutz, T.; Williams, R. Co-production of Hydrogen, Electricity and CO_2 from Coal with Commercially Ready Technology. Part A. Performance and emissions. Intl J. Hydrogen Energy 2005 30 747–767.

Chiesa, P.; Consonni, S.; Kreutz, T.; Williams, R. Co-production of Hydrogen, Electricity and CO_2 from Coal with Commercially Ready Technology. Part B. Economic analysis. Intl J. Hydrogen Energy 2005 30 769–784.

Dutta, B.N.; B. Dayal, B. "Lattice constants and thermal expansion of palladium and tungsten up to 878 ºC by X-ray method," phys. stat. sol., 3 (1963) 2253.

Dutta, B.N.; B. Dayal, B. "Lattice constants and thermal expansion of gold up to 878 ºC by X-ray method," phys. stat. sol., 3 (1963) 473.

Driscoll, D.; Morreale, B.; Headley, L. *NETL Test Protocol – Testing of Hydrogen Separation Membranes*; DOE/NETL–2008/1335; U.S. Department of Energy, National Energy Technology Laboratory: Morgantown, WV, October 2008.

Eichler, A. "Tetragonal Y-doped zirconia: Structure and ion conductivity," Phys. Rev. B, 64 (2001) 174103-1-8.

H. Hayashi, H.; Saitou, T.; Maruyama, N.; Inaba, H.; Kawamura, K.; Mori, M. **"**Thermal expansion coefficient of yttria stabilized zirconia for various yttria contents," Solid State Ionics 176 (2005) 613-619.

McKinley, D.L. *Metal Alloy for Hydrogen Separation and Purification.* U.S. Patent 3,350,845, 1967.

McKinley, D.L. *Method for Hydrogen Separation and Purification.* U.S. Patent 3,439,474, 1969.

www.matweb.com website, accessed 2010.

Morreale, B.D. "The influence of H2S on palladium and palladium-copper alloy membranes," Ph.D. Thesis, University of Pittsburgh, 2006.

Morreale, B.D.; Howard, B.H.; Iyoha, O.; Enick, R.M.; Ling, C.; Sholl, D.S. "Experimental and Computational Prediction of the Hydrogen Transport Properties of Pd_4S," *Ind. Eng. Chem. Res.* 46 (2007) 6313-6319.

Yashima, M.; Kakihana, M.; Yoshimura, M. "Metastable–stable phase diagrams in zirconia-containing systems utilized in solid-oxide fuel cell application," Solid State Ionics, 86–88 (1996) 1131–1149.